Quality control of mass-produced nanomaterials

Edited by Luiz Gustavo de Oliveira Lopes Cançado and Claudia Backes

Imprint

Reliable fabrication of transparent conducting films by cascade centrifugation and Langmuir–Blodgett deposition of electrochemically exfoliated graphene

Teodora Vićentić[*1], Stevan Andrić[1], Vladimir Rajić[2] and Marko Spasenović[*1]

Full Research Paper

Address:
[1]Center for Microelectronic Technologies, Institute of Chemistry, Technology and Metallurgy, National Institute of the Republic of Serbia, University of Belgrade, Njegoševa 12, Belgrade 11000, Serbia and [2]INS Vinča, Department of Atomic Physics, University of Belgrade, Mike Petrovića Alasa 12–14, 11351 Belgrade, Serbia

Email:
Teodora Vićentić[*] - teodora@nanosys.ihtm.bg.ac.rs;
Marko Spasenović[*] - spasenovic@nanosys.ihtm.bg.ac.rs

* Corresponding author

Keywords:
2D materials; cascade centrifugation; graphene; Langmuir–Blodgett deposition; transparent conductors

Abstract

Electrochemical exfoliation is an efficient and scalable method to obtain liquid-phase graphene. Graphene in solution, obtained through electrochemical exfoliation or other methods, is typically polydisperse, containing particles of various sizes, which is not optimal for applications. We employed cascade centrifugation to select specific particle sizes in solution and prepared thin films from those graphene particles using the Langmuir–Blodgett assembly. Employing centrifugation speeds of 3, 4, and 5 krpm, further diluting the solutions in different volumes of solvent, we reliably and consistently obtained films of tunable thickness. We show that there is a limit to how thin these films can be, which is imposed by the percolation threshold. The percolation threshold is quantitatively compared to results found in literature that are obtained using other, more complex graphene film fabrication methods, and is found to occur with a percolation exponent and percolative figure of merit that are of the same order as results in literature. A maximum optical transparency of 82.4% at a wavelength of 660 nm is obtained for these films, which is in agreement with earlier works on Langmuir–Blodgett assembled ultrasonic-assisted liquid-phase exfoliated graphene. Our work demonstrates that films that are in all respects on par with films of graphene obtained through other solution-based processes can be produced from inexpensive and widely available centrifugal post-processing of existing commercially available solutions of electrochemically exfoliated graphene. The demonstrated methodology will lower the entry barriers for new research and industrial uses, since it allows researchers with no exfoliation experience to make use of widely available graphene materials.

Introduction

The interest in graphene and other 2D materials keeps growing, especially since the initial delve into fundamental properties was augmented with an outlook towards potential applications [1]. Over the past decades, a great number of different methods for the synthesis of graphene and other 2D materials has been proposed, including micromechanical cleavage [2], chemical vapor deposition (CVD) [3-7], epitaxial growth on different substrates [8,9], and the chemical reduction of graphene oxide (GO) [10,11]. In 2008, production of graphene by liquid-phase exfoliation (LPE) of graphite through sonication of graphite powder in *N*-methylpyrrolidone (NMP) was first proposed by Coleman et al. [12] as a synthesis method with high potential for scaling. Since then, LPE has developed into a common, highly scalable method for graphene synthesis in liquid media. This method is used for the production of 2D nanosheets with lateral sizes ranging from 100 nm to 100 μm and thicknesses in the range of 1–10 layers, in a range of different liquids, at a wide range of concentrations [13,14].

The mechanism of ultrasonic exfoliation involves ultrasonic waves in liquid media creating bubbles or voids in the liquid, which generate shear forces or cavitation bubbles upon collapsing, which then break up the bulk 2D materials into mono- and few-layer nanosheets [15,16]. The choice of solvent for LPE is made based on surface energy considerations, compatible solvents include NMP, dimethylformamide (DMF), *N,N*-dimethylacetamide (DMA), γ-butyrolactone (GBL), 1,3-dimethyl-2-imidazolidinone (DMEU), and *ortho*-dichlorobenzene (*o*-DCB) [12,17,18]. Exfoliation in NMP has led to minimally oxidized graphene sheets with approximately 28% monolayer flakes, and more than 75% of sheets with a thickness of less than six layers [12].

An alternative to LPE that has subsequently been developed is electrochemical exfoliation, whereby graphene is exfoliated in an electrolyte from an electrode made of graphite [19]. In electrochemical exfoliation, ions from the electrolyte flow towards the graphite electrode and intercalate between the graphene layers. The electrochemical reaction provides a driving force to break van der Waals forces, leading to exfoliation [20]. Electrochemical exfoliation offers an alternative to LPE that is both scalable and widely available. It has been used to make graphene for various applications, including energy storage [21,22].

Both ultrasound-assisted LPE and electrochemical exfoliation result in solutions that contain flakes of different sizes, that is, the solutions are polydisperse. Polydispersity is a significant problem regarding the use of solution-processed graphene, because many applications are size-dependent. On the one hand, for example, for use in composites, flakes with lateral sizes larger than 1 μm are preferred [23]. On the other hand, thinner (thus also laterally smaller [24]) flakes have a higher transparency, with potential use in transparent conductors. Size selection of 2D material flakes in solution has thus become a key challenge for the practical use of solution-processed 2D materials [24,25].

The flake size can either be controlled during exfoliation or selected after exfoliation. Processing parameters that control flake size during exfoliation include the choice and concentration of solvent [25], a process control alternating sonication with shear mixing [26], or the duration of exfoliation [27]. Using LPE for 2D materials that are size-selected during exfoliation limits their use to research groups with expertise in this method. After exfoliation, sizes can be selected by centrifugal processing, which narrows the nanosheet size and thickness distribution, depending on the centrifugation parameters. However, it is important to consider the impact of buoyant density and drag coefficient of the materials, as well as the viscosity of the solvent and many other parameters to achieve the desired results [28]. It was demonstrated by Coleman et al. that controlled centrifugation can be used for the selection of liquid-phase exfoliated graphene dispersions with mean flake sizes in the range from 1 to 3.5 μm [29]. Since centrifugation is a much more facile process than exfoliation, and centrifuges are widely available, post-exfoliation size selection is the route to take towards the mass use of 2D materials in solution.

Although size selection through post-processing with cascade centrifugation has been demonstrated in the context of ultrasonic LPE materials [30,31], to the best of our knowledge, the method has not been applied to electrochemically exfoliated graphene, nor have thin films made from dispersions following size selection through centrifugation been studied for their optoelectronic properties. Here, we present size selection through cascade centrifugation of commercially obtained electrochemically exfoliated graphene. We follow the Langmuir–Blodgett (LB) method to deposit graphene flakes from solution as uniform thin films. LB has proven to be a method that yields reliable graphene films that have been used as transparent conductors [27,32-34] and gas sensors [35,36]. By measuring optical transmittance and electrical resistance of the deposited films, we find a tradeoff between transparency and electrical performance for applications in transparent conductors. We demonstrate that, below a certain critical thickness, graphene films deposited with LB reach a percolation limit, which imposes a minimum achievable film thickness for a reasonable electrical conductivity. For both, our films made from electrochemically exfoliated graphene and literature-referenced films

made from ultrasonic LPE graphene, the percolation limit is reached at an optical transmittance of ca. 83%. This number quantifies the maximum transmittance achievable with LB assembly of graphene films made from solution-dispersed material, for a reasonable electrical conductivity. Comparisons of our obtained percolative figure of merit and percolation exponent with those observed in literature reveal that the quality of the films obtained with our demonstrated method is on par with graphene films made with other methods that make use of liquid-phase graphene. Hence, we demonstrate that commercially obtained solutions of graphene can be post-processed with a simple laboratory centrifuge and deposited into thin films with a quality on par with films obtained with other methods that require more effort from the lab workers, as well as exfoliation expertise and equipment.

## Experimental
Cascade centrifugation

In order to achieve homogeneous films with defined particle sizes, a dispersion of electrochemically exfoliated graphene from Sixonia Tech GmbH (G-DI5P-NMP-C50-2+, Dresden, Germany) was processed by cascade centrifugation (centrifuge model: COLO LACE16 from Novo Mesto, Slovenia, rotor R30403 with radius 8.19 cm). The commercially obtained solution contained a dispersion of graphene in NMP. Although many solvents are commercially available, NMP was the solvent of choice because of its favorable properties regarding LB deposition [14]. 1 mL of dispersion was initially centrifuged at a rate of 1500 rpm (relative centrifugal force, RCF, equal to 206g). The obtained centrifugation sediment contained the largest nanosheets of the initial dispersion. The supernatant was subsequently centrifuged at higher rates: 2, 3, 4, and 5 krpm (366g, 824g, 1465g, and 2289g). At each step of centrifugation, the sediments with slightly smaller graphene sheets were gathered and the supernatants were used for the following cascade step. The sediments were collected and redispersed in a specific volume of NMP (Sigma-Aldrich M79603), which ranged between 250 and 1000 μL. This method is schematically described in Figure 1.
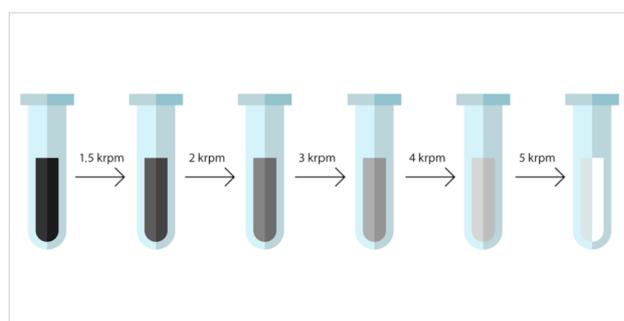
Figure 1: The process of cascade centrifugation.

Film deposition

In order to study the optical properties of the produced graphene films, graphene from solution was deposited onto glass substrates with dimensions of ca. 2 cm × 1 cm (Figure 2a). Although a great number of different types of substrate materials have been used, such as silica [37], chromium [38], tin [39], silver [40], or platinum [41], glass substrates were used in this paper. Glass is generally a popular choice, not just because glass slides are inexpensive and widely available, but also because the optical characteristics of deposited films can be subsequently examined [42]. For measuring the electrical resistance, the film was deposited onto Metrohm DropSens substrates with a pair of interdigitated electrodes (G-IDEPT10, Oviedo, Spain, Figure 2b). Using an automated pipette, the entire specific volume of the graphene dispersion in NMP was vertically dripped onto the surface of deionized water. Because the volumes ranged from 250 to 1000 μL, while the amount of graphene in that volume was kept fixed, the concentration of graphene was varied. As the film of graphene formed on the surface of the water, the LB method was used to deposit the film onto the target substrate [32].
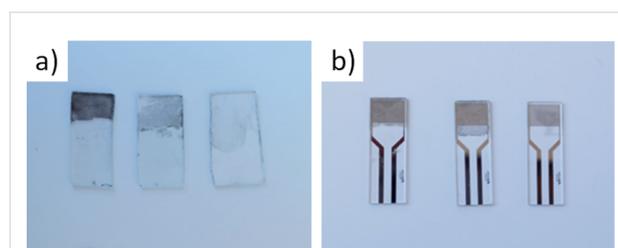
Figure 2: Deposited graphene films at centrifugation rates of 3, 4, and 5 krpm (824g, 1465g, and 2289g, respectively) from left to right; (a) glass substrate, (b) Metrohm DropSens substrates.

Film characterization

To study optical properties of the fabricated samples, UV–vis spectroscopy was performed (Thermo Fisher Scientific EVO 60, Madison, USA). A xenon lamp was used as a light source. The glass samples were mounted on a holder and inserted into the light path. Optical transmittance was measured by subtracting the signal from a baseline reference signal obtained when a clean glass substrate without graphene was inserted into the light path.

Graphene film resistance was measured by inserting the substrates with electrodes into an electrode connector (DRP-CACIDE, Metrohm, Oviedo, Spain) and the acquiring resistance with a handheld digital multimeter.

Optical dark-field microscopy of the films was performed with a magnification of 10× (Olympus BX53M). Scanning electron

microscopy (SEM) was performed with a FESEM (FEI Scios 2, Thermo Fisher Scientific, Waltham, MA, USA) at a chamber pressure of 1×10^{-4} Pa with electron beam voltages set between 1 and 30 kV, depending on the film. Films that are shown in optical dark-field microscopy and SEM have been made from solutions that have been diluted with 500 µL of NMP.
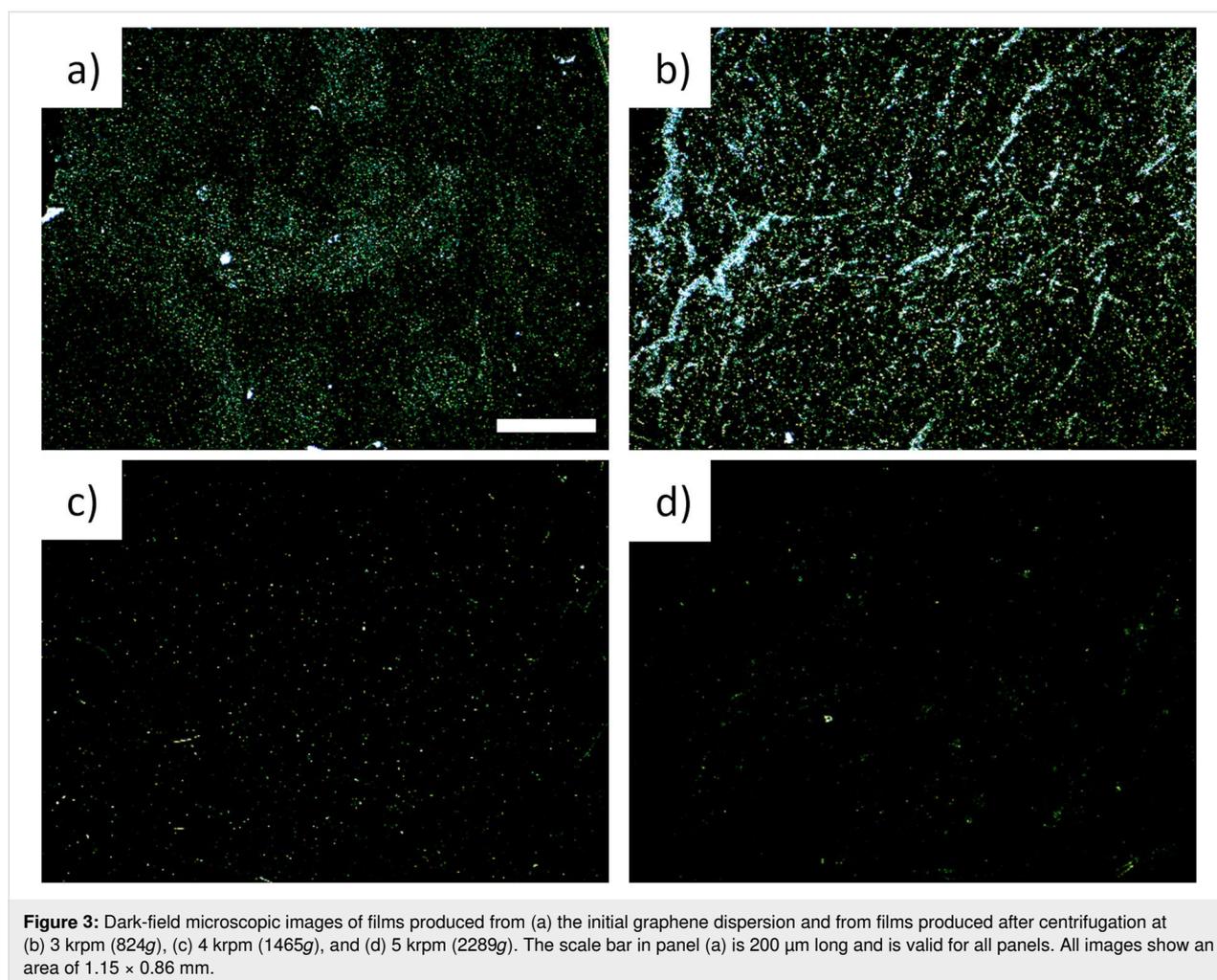
Results
Optical observation
Films deposited from solutions obtained from different centrifugation protocols are expected to have different thicknesses, due to the different size of the flakes in the solutions. A visual inspection of the images in Figure 2 confirms that slower centrifugation rates (samples on the left) yield thicker films than faster centrifugation rates (samples on the right), which is expected because flakes are thicker and laterally larger when processed at slower rates. To gain further insight into the thickness and quality of these films, we performed optical dark-field microscopy with a magnification of 10×. Photographs of deposited graphene films from solutions processed at different centrifugation rates are depicted in Figure 3. Films made directly from the initial polydisperse solution (Figure 3a) show regions with a high density of scattering centers (green and white points) intermixed with regions with a lower density of scattering centers (darker regions with few bright points). Size-selected solutions yield films that are more uniform, with dark-field microscopy revealing homogeneous distributions of scattering centers. Hence, we find that films from polydisperse films are not as homogeneous as films made from solutions that have been processed by centrifugation for size selection. There is an evident decrease in the density and intensity of scattering centers with increasing centrifugation rate, which indicates films with a decreased density of large particles.

We quantify the number of scattering centers by analyzing the dark-field images using the software imageJ. First, we set the brightness threshold for what counts as a scattering particle. As these are dark-field images, anything that is not completely dark is counted as a scattering particle. Thus, we set the threshold at a brightness value of 3 (on a scale from 0 to 255). Such an anal-

Figure 3: Dark-field microscopic images of films produced from (a) the initial graphene dispersion and from films produced after centrifugation at (b) 3 krpm (824*g*), (c) 4 krpm (1465*g*), and (d) 5 krpm (2289*g*). The scale bar in panel (a) is 200 µm long and is valid for all panels. All images show an area of 1.15 × 0.86 mm.

ysis yields results that are consistent with intuitive observation (Table 1).

Table 1: Analysis of scattering centers from dark-field observation. Both the number of particles and their total area decreases with centrifugation rate.

Centrifugation rate	Particle count	Total area	% area
3 krpm (824*g*)	5001	58972	32.329
4 krpm (1465*g*)	1909	3029	1.661
5 krpm (2289*g*)	1053	2159	1.184

The film structure was further investigated with SEM, shown in Figure 4. In general, the films look alike when they are made of the as-purchased uncentrifuged solution and when they are made from solutions centrifuged at 3 krpm (824*g*) and at 4 krpm (1465*g*). In these three cases, SEM reveals continuous graphene films. The films contain some wrinkles or flake edges, showing up as bright lines in SEM. Upon closer inspection, the contrast varies slightly across the films, which is likely due to local thickness variations. Overall, the films resemble those made earlier with ultrasonic liquid-phase exfoliation followed by LB deposition [14]. However, the film made from a solution that has been centrifuged at 5 krpm (2289*g*) is strikingly different from the ones made with lower centrifugation speeds. The 5 krpm (2289*g*) film has an irregular structure, resembling a fractal coastline. It is also noted that the conductivity of this film is much lower than those of the other three films, as SEM operation quickly leads to surface charging effects.

Optoelectronic properties

UV–vis spectra of the deposited graphene films at different centrifugation rates, redispersed in specified volumes of NMP, are given in Figure 5. The optical transmission spectra are expectedly uniform across the visible part of the spectrum. It is evident that the optical transparency can be controlled by the centrifugation rate, as well as by tuning the concentration of graphene particles by redispersing in different volumes of NMP. Optical transparencies were measured at the wavelength of 660 nm and the number of graphene layers was calculated for each sample, taking into account an absorption of 2.3% for each layer of graphene, as in the work by Bonaccorso and co-workers [43].
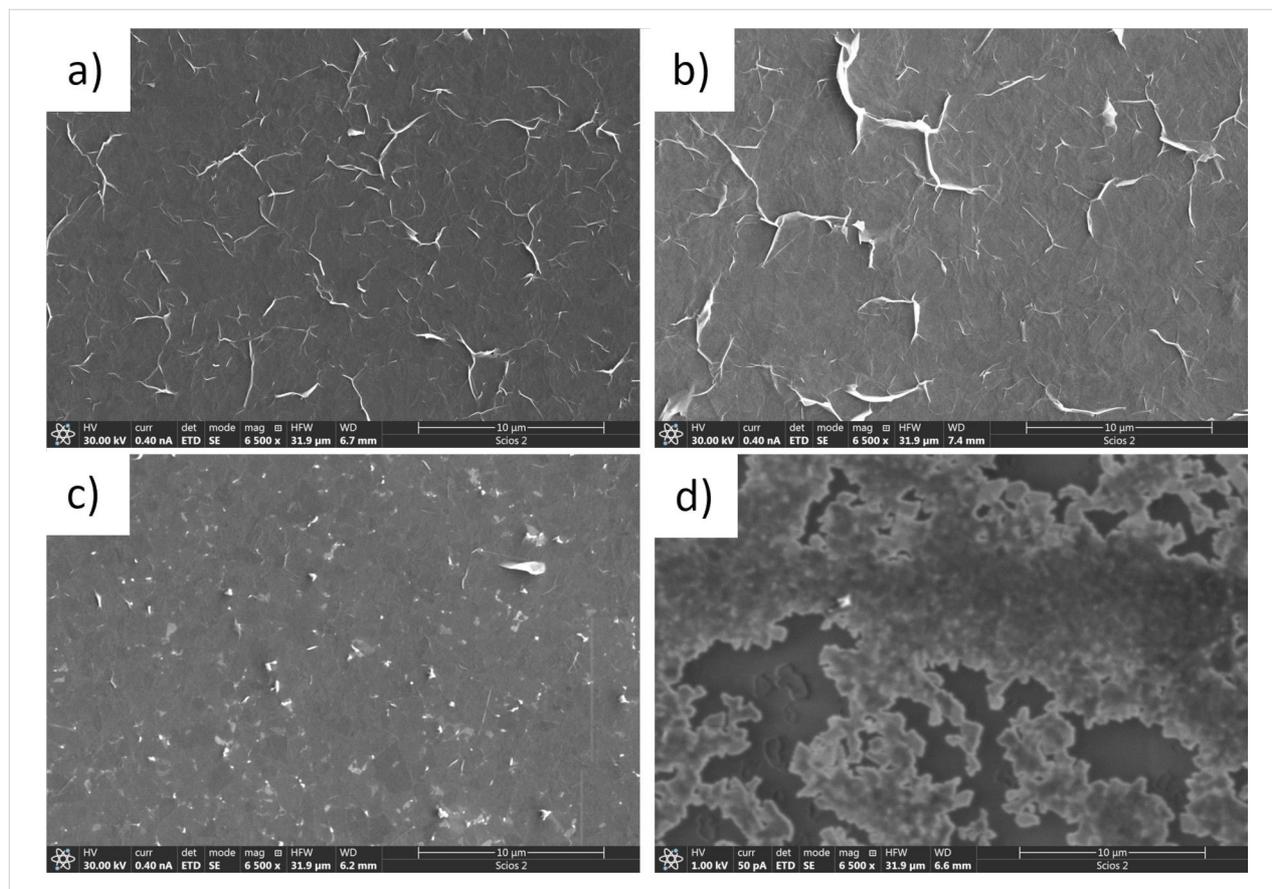
Figure 4: Scanning electron micrographs of films produced from the (a) initial graphene dispersion and from films produced after centrifugation at (b) 3 krpm (824*g*), (c) 4 krpm (1465*g*), and (d) 5 krpm (2289*g*).
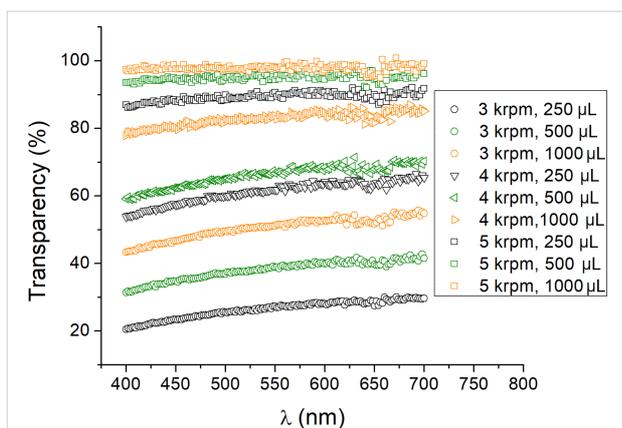
Figure 5: UV–vis spectra of deposited graphene films at different centrifugation rates, redispersed in specified volumes of NMP.

Although atomic force microscopy (AFM) is often employed to characterize graphene films [2,12,14,44], applying that method to films that consist of heterogeneous flakes, such as Langmuir–Blodgett-deposited films, is more difficult. Since the thickness varies from flake to flake, only an average film thickness over a certain area makes sense. The area over which average thickness can be measured with AFM is limited by the scan size, at a maximum of about 50 μm × 50 μm. The best method for measuring the average film thickness with AFM is to make scans that show the underlying substrate as well as the film itself and to make a histogram of measured heights, where a narrow peak related to the substrate and a broader peak related to the film surface appear. Then, the thickness is measured as the distance between those two peaks in the histogram [14,33]. With that method, the accuracy of measuring the average film thickness depends on the size of the scanned area. Optical transparency, in contrast, is a good measure of film thickness averaged over the size of the optical spot. For example, in [33], it was shown that thickness measurements from optical transmit-

tance match the results obtained with AFM, for continuous films. However, for films that do not cover the substrate completely, such as the one shown in Figure 4d, measuring the average film thickness with AFM would be impossible, because one needs to measure over a large area to take into account regions with flakes as well as regions without. Optical transmittance is a good measure of the average thickness even in the case of films that do not cover the substrate completely.

To analyze the electrical properties of the synthesized graphene films, resistance values of each film were measured. Resistance values, optical transparency values, and the average number of layers in each graphene film are shown in Table 2. A larger number of graphene layers implies a smaller electrical resistance. The relation of optical transparency and electrical resistance for all samples is given in Figure 6. The measured optical transmittance varied slightly depending on the exact spot chosen on each given sample. The measured resistance varied
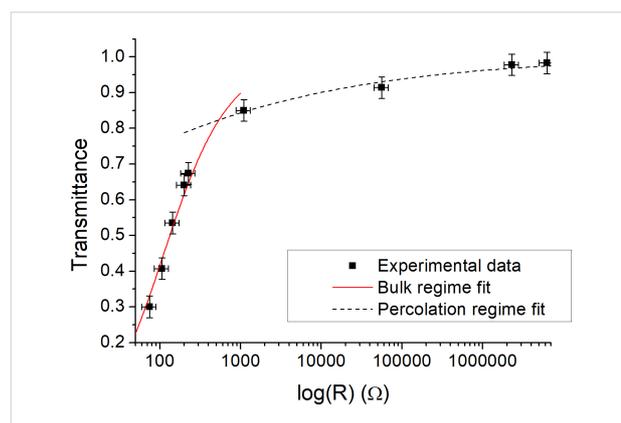
Figure 6: Dependence of the optical transparency on the electrical resistance of graphene films on a semi-logarithmic scale. The data can be divided into two regimes, the bulk regime (solid red line fit to Equation 1) and the percolation regime (dashed black line fit to Equation 2).

Table 2: Measured optical transparency, number of layers, and electrical resistance for samples obtained at different centrifugation rates, dissolved in the specified volumes of NMP.

	V (NMP)	Optical transparency	Average number of layers	Resistance
3 krpm (824g)	250 μL	30.0%	30.4	74.6 Ω
	500 μL	40.7%	25.8	106.4 Ω
	1000 μL	54.0%	20.0	144.0 Ω
4 krpm (1465g)	250 μL	64.1%	15.6	200.0 Ω
	500 μL	67.4%	14.2	226.0 Ω
	1000 μL	85.0%	6.5	1.1 kΩ
5 krpm (2289g)	250 μL	91.4%	3.7	56.1 kΩ
	500 μL	94.0%	2.3	2.3 MΩ
	1000 μL	98.2%	0.8	6.3 MΩ

by about 20% between different samples prepared with identical methodology. Since only several samples were made for each set of processing parameters, the error bars in Figure 6 represent the maximum deviation from the mean observed during experimentation.

Discussion

The images in Figure 2 show that the thickness of the deposited graphene films decreases with increasing centrifugation rates, while Figure 3 indicates that thinner films also consist of smaller particles, which is in accordance with expectations. UV–vis spectra depicted in Figure 5 show that for a given centrifugation rate the optical transmittance of the deposited graphene film has a value that scales with the quantity of solvent used. The results thus indicate that dilution of solution-processed graphene can be used as a tool to control graphene film thickness. Also, the centrifugation rate can be controlled to make films of desired thickness.

Regardless of how the film thickness is controlled, an analysis of Figure 6 reveals that there are two different regimes, that is, one in which the optical transmittance sharply rises with increasing resistance, at lower transmittance values, and another in which the optical transmittance rises with increasing resistance to a much smaller extent, at higher transmittance values. It has been noted before that thin transparent conductors [45], including graphene [46], exhibit a percolation threshold. For film thicknesses above this threshold, the film behaves as a bulk material and the transmittance and sheet resistance R_S obey the following equation:

$$T = \left[1 + \frac{Z_0}{2R_S} \frac{\sigma_{op}}{\sigma_{dc,B}} \right]^{-2} \qquad (1)$$

where Z_0 is the impedance of free space, σ_{op} is the optical conductivity, and $\sigma_{dc,B}$ is the bulk dc conductivity of the film. For film thicknesses below the percolation threshold, the transmittance and sheet resistance obey the following equation:

$$T = \left[1 + \frac{1}{\Pi} \left(\frac{Z_0}{R_S} \right)^{1/(n+1)} \right]^{-2} \qquad (2)$$

where Π is the percolative figure of merit (FOM) as described by De and Coleman [45] and n is the percolation exponent.

We fit the above two equations to our data in the two observed regimes independently. The solid red line in Figure 6 is a fit to Equation 1 which indicates the bulk regime, whereas the dashed

black line is a fit to Equation 2 for the percolation regime. The fit results in $\Pi = 1.1$ and $n = 3.6$, values which are of the same order as values previously observed for graphene [45]. The good match between our results and previously reported ones is yet another indication that the method that we used yields films of similar quality as observed earlier with other methods, although our method is facile and starts from commercially available material.

The two regimes exhibit a crossover that likely indicates the percolation threshold. The value of optical transparency at which we observe the threshold is 82.4%, matching the value found in an earlier work that showed particle size selection by control of liquid-phase exfoliation time [27], possibly indicating an upper limit for optical transparency achievable with Langmuir–Blodgett graphene films. The observed critical threshold transparency is equivalent to films which have a thickness of 7.6 layers of graphene, which is 2.6 nm. It is likely that reliably conducting films thinner than this cannot be achieved with Langmuir–Blodgett assembly of graphene nanoplatelets. Compared to the work in which the exfoliation time is controlled in the same lab where film deposition is made, our approach is advantageous because it allows experimenters to focus on film formation alone, leaving exfoliation to a partner lab or commercial vendor.

Conclusion

Solution-processed graphene holds potential for applications across a diverse range of industries. There exist several production methods for solution-processed graphene, some of which are highly scalable. However, all graphene solutions resulting from those processes are polydisperse, containing a wide distribution of particle sizes, which is unfavorable for applications. It was previously shown that cascade centrifugation can be used as a common method for the separation of graphene particles by size, in the case of ultrasound-assisted liquid-phase exfoliated graphene. In this paper, we demonstrated that cascade centrifugation of electrochemically exfoliated graphene can be used in conjunction with Langmuir–Blodgett assembly to produce thin graphene films. By tuning centrifugation speed and solvent dilution volume, we produced films of different controlled thicknesses. We have shown that the optical transparency and electrical resistance of these films behave similarly to those of other films made of graphene from solution. Namely, the films exhibit a percolation threshold, at which optoelectronic properties experience a critical change. The percolation exponent and percolative FOM are found to be of the same order as in the case of other graphene films found in literature, which indicates that our films are of a similar quality. However, the method that we have used, which relies on cascade centrifugation of a commercially available solution of graphene, is easily

accessible to researchers who have no exfoliation experience or equipment. We have shown that ownership of a centrifuge is the only prerequisite for making practical use of widely available graphene in solution.

Funding

ORCID® iDs

Teodora Vićentić - https://orcid.org/0000-0002-3460-6137
Stevan Andrić - https://orcid.org/0000-0002-9122-9104
Vladimir Rajić - https://orcid.org/0000-0001-7053-572X
Marko Spasenović - https://orcid.org/0000-0002-2173-0972

References

1. Ferrari, A. C.; Bonaccorso, F.; Fal'ko, V.; Novoselov, K. S.; Roche, S.; Bøggild, P.; Borini, S.; Koppens, F. H. L.; Palermo, V.; Pugno, N.; Garrido, J. A.; Sordan, R.; Bianco, A.; Ballerini, L.; Prato, M.; Lidorikis, E.; Kivioja, J.; Marinelli, C.; Ryhänen, T.; Morpurgo, A.; Coleman, J. N.; Nicolosi, V.; Colombo, L.; Fert, A.; Garcia-Hernandez, M.; Bachtold, A.; Schneider, G. F.; Guinea, F.; Dekker, C.; Barbone, M.; Sun, Z.; Galiotis, C.; Grigorenko, A. N.; Konstantatos, G.; Kis, A.; Katsnelson, M.; Vandersypen, L.; Loiseau, A.; Morandi, V.; Neumaier, D.; Treossi, E.; Pellegrini, V.; Polini, M.; Tredicucci, A.; Williams, G. M.; Hee Hong, B.; Ahn, J.-H.; Min Kim, J.; Zirath, H.; van Wees, B. J.; van der Zant, H.; Occhipinti, L.; Di Matteo, A.; Kinloch, I. A.; Seyller, T.; Quesnel, E.; Feng, X.; Teo, K.; Rupesinghe, N.; Hakonen, P.; Neil, S. R. T.; Tannock, Q.; Löfwander, T.; Kinaret, J. *Nanoscale* **2015,** *7,* 4598–4810. doi:10.1039/c4nr01600a

2. Novoselov, K. S.; Geim, A. K.; Morozov, S. V.; Jiang, D.; Zhang, Y.; Dubonos, S. V.; Grigorieva, I. V.; Firsov, A. A. *Science* **2004,** *306,* 666–669. doi:10.1126/science.1102896

3. Yu, Q.; Lian, J.; Siriponglert, S.; Li, H.; Chen, Y. P.; Pei, S.-S. *Appl. Phys. Lett.* **2008,** *93,* 113103. doi:10.1063/1.2982585

4. Gomez De Arco, L.; Zhang, Y.; Kumar, A.; Zhou, C. *IEEE Trans. Nanotechnol.* **2009,** *8,* 135–138. doi:10.1109/tnano.2009.2013620

5. Reina, A.; Jia, X.; Ho, J.; Nezich, D.; Son, H.; Bulovic, V.; Dresselhaus, M. S.; Kong, J. *Nano Lett.* **2009,** *9,* 30–35. doi:10.1021/nl801827v

6. Li, X.; Cai, W.; An, J.; Kim, S.; Nah, J.; Yang, D.; Piner, R.; Velamakanni, A.; Jung, I.; Tutuc, E.; Banerjee, S. K.; Colombo, L.; Ruoff, R. S. *Science* **2009,** *324,* 1312–1314. doi:10.1126/science.1171245

7. Somani, P. R.; Somani, S. P.; Umeno, M. *Chem. Phys. Lett.* **2006,** *430,* 56–59. doi:10.1016/j.cplett.2006.06.081

8. Sutter, P. W.; Flege, J.-I.; Sutter, E. A. *Nat. Mater.* **2008,** *7,* 406–411. doi:10.1038/nmat2166

9. Yazdi, G. R.; Iakimov, T.; Yakimova, R. *Crystals* **2016,** *6,* 53. doi:10.3390/cryst6050053

10. Chen, W.; Yan, L.; Bangal, P. R. *J. Phys. Chem. C* **2010,** *114,* 19885–19890. doi:10.1021/jp107131v

11. Guex, L. G.; Sacchi, B.; Peuvot, K. F.; Andersson, R. L.; Pourrahimi, A. M.; Ström, V.; Farris, S.; Olsson, R. T. *Nanoscale* **2017,** *9,* 9562–9571. doi:10.1039/c7nr02943h

12. Hernandez, Y.; Nicolosi, V.; Lotya, M.; Blighe, F. M.; Sun, Z.; De, S.; McGovern, I. T.; Holland, B.; Byrne, M.; Gun'ko, Y. K.; Boland, J. J.; Niraj, P.; Duesberg, G.; Krishnamurthy, S.; Goodhue, R.; Hutchison, J.; Scardaci, V.; Ferrari, A. C.; Coleman, J. N. *Nat. Nanotechnol.* **2008,** *3,* 563–568. doi:10.1038/nnano.2008.215

13. Backes, C.; Higgins, T. M.; Kelly, A.; Boland, C.; Harvey, A.; Hanlon, D.; Coleman, J. N. *Chem. Mater.* **2017,** *29,* 243–255. doi:10.1021/acs.chemmater.6b03335

14. Tomašević-Ilić, T.; Pešić, J.; Milošević, I.; Vujin, J.; Matković, A.; Spasenović, M.; Gajić, R. *Opt. Quantum Electron.* **2016,** *48,* 319. doi:10.1007/s11082-016-0591-1

15. Alzakia, F. I.; Tan, S. C. *Adv. Sci.* **2021,** *8,* 2003864. doi:10.1002/advs.202003864

16. Li, Z.; Young, R. J.; Backes, C.; Zhao, W.; Zhang, X.; Zhukov, A. A.; Tillotson, E.; Conlan, A. P.; Ding, F.; Haigh, S. J.; Novoselov, K. S.; Coleman, J. N. *ACS Nano* **2020,** *14,* 10976–10985. doi:10.1021/acsnano.0c03916

17. Haar, S.; El Gemayel, M.; Shin, Y.; Melinte, G.; Squillaci, M. A.; Ersen, O.; Casiraghi, C.; Ciesielski, A.; Samorì, P. *Sci. Rep.* **2015,** *5,* 16684. doi:10.1038/srep16684

18. Ghanbari, H.; Shafikhani, M. A.; Daryalaal, M. *Ceram. Int.* **2019,** *45,* 20051–20057. doi:10.1016/j.ceramint.2019.06.267

19. Su, C.-Y.; Lu, A.-Y.; Xu, Y.; Chen, F.-R.; Khlobystov, A. N.; Li, L.-J. *ACS Nano* **2011,** *5,* 2332–2339. doi:10.1021/nn200025p

20. Yu, P.; Lowe, S. E.; Simon, G. P.; Zhong, Y. L. *Curr. Opin. Colloid Interface Sci.* **2015,** *20,* 329–338. doi:10.1016/j.cocis.2015.10.007

21. Wei, D.; Grande, L.; Chundi, V.; White, R.; Bower, C.; Andrew, P.; Ryhänen, T. *Chem. Commun.* **2012,** *48,* 1239–1241. doi:10.1039/c2cc16859f

22. Abdelkader, A. M.; Cooper, A. J.; Dryfe, R. A. W.; Kinloch, I. A. *Nanoscale* **2015,** *7,* 6944–6956. doi:10.1039/c4nr06942k

23. Sudhindra, S.; Rashvand, F.; Wright, D.; Barani, Z.; Drozdov, A. D.; Baraghani, S.; Backes, C.; Kargar, F.; Balandin, A. A. *ACS Appl. Mater. Interfaces* **2021,** *13,* 53073–53082. doi:10.1021/acsami.1c15346

24. Backes, C.; Campi, D.; Szydlowska, B. M.; Synnatschke, K.; Ojala, E.; Rashvand, F.; Harvey, A.; Griffin, A.; Sofer, Z.; Marzari, N.; Coleman, J. N.; O'Regan, D. D. *ACS Nano* **2019,** *13,* 7050–7061. doi:10.1021/acsnano.9b02234

25. Griffin, A.; Nisi, K.; Pepper, J.; Harvey, A.; Szydłowska, B. M.; Coleman, J. N.; Backes, C. *Chem. Mater.* **2020,** *32,* 2852–2862. doi:10.1021/acs.chemmater.9b04684

26. Di Berardino, C.; Bélteky, P.; Schmitz, F.; Lamberti, F.; Menna, E.; Kukovecz, Á.; Gatti, T. *Crystals* **2020,** *10,* 1049. doi:10.3390/cryst10111049

27. Kim, H.; Mattevi, C.; Kim, H. J.; Mittal, A.; Mkhoyan, K. A.; Riman, R. E.; Chhowalla, M. *Nanoscale* **2013,** *5,* 12365–12374. doi:10.1039/c3nr02907g

28. Narayan, R.; Kim, S. O. *Nano Convergence* **2015,** *2,* 20. doi:10.1186/s40580-015-0050-x

29. Khan, U.; Porwal, H.; O'Neill, A.; Nawaz, K.; May, P.; Coleman, J. N. *Langmuir* **2011,** *27,* 9077–9082. doi:10.1021/la201797h

30. Backes, C.; Hanlon, D.; Szydlowska, B. M.; Harvey, A.; Smith, R. J.; Higgins, T. M.; Coleman, J. N. *J. Visualized Exp.* **2016,** No. 118, e54806. doi:10.3791/54806

31. Backes, C.; Szydłowska, B. M.; Harvey, A.; Yuan, S.; Vega-Mayoral, V.; Davies, B. R.; Zhao, P.-l.; Hanlon, D.; Santos, E. J. G.; Katsnelson, M. I.; Blau, W. J.; Gadermaier, C.; Coleman, J. N. *ACS Nano* **2016,** *10,* 1589–1601. doi:10.1021/acsnano.5b07228

32. Tomašević-Ilić, T.; Jovanović, Đ.; Popov, I.; Fandan, R.; Pedrós, J.; Spasenović, M.; Gajić, R. *Appl. Surf. Sci.* **2018,** *458,* 446–453. doi:10.1016/j.apsusc.2018.07.111

33. Matković, A.; Milošević, I.; Milićević, M.; Tomašević-Ilić, T.; Pešić, J.; Musić, M.; Spasenović, M.; Jovanović, D.; Vasić, B.; Deeks, C.; Panajotović, R.; Belić, M. R.; Gajić, R. *2D Mater.* **2016,** *3,* 015002. doi:10.1088/2053-1583/3/1/015002

34. Milošević, I. R.; Vasić, B.; Matković, A.; Vujin, J.; Aškrabić, S.; Kratzer, M.; Griesser, T.; Teichert, C.; Gajić, R. *Sci. Rep.* **2020,** *10,* 8476. doi:10.1038/s41598-020-65379-1

35. Andrić, S.; Sarajlić, M.; Frantlović, M.; Jokić, I.; Vasiljević-Radović, D.; Spasenović, M. *Chemosensors* **2021,** *9,* 342. doi:10.3390/chemosensors9120342

36. Andrić, S.; Tomašević-Ilić, T.; Bošković, M. V.; Sarajlić, M.; Vasiljević-Radović, D.; Smiljanić, M. M.; Spasenović, M. *Nanotechnology* **2021,** *32,* 025505. doi:10.1088/1361-6528/abb973

37. Kajzar, F.; Girling, I. R.; Peterson, I. R. *Thin Solid Films* **1988,** *160,* 209–215. doi:10.1016/0040-6090(88)90064-8

38. Drévillon, B. *Prog. Cryst. Growth Charact. Mater.* **1993,** *27,* 1–87. doi:10.1016/0960-8974(93)90021-u

39. Khanna, U.; Srivastava, V. K. *Thin Solid Films* **1972,** *12,* S25–S28. doi:10.1016/0040-6090(72)90419-1

40. Rothenhäusler, B.; Knoll, W. *Nature* **1988,** *332,* 615–617. doi:10.1038/332615a0

41. Collard, D. M.; Fox, M. A. *J. Am. Chem. Soc.* **1991,** *113,* 9414–9415. doi:10.1021/ja00024a083

42. Blodgett, K. B. *J. Am. Chem. Soc.* **1935,** *57,* 1007–1022. doi:10.1021/ja01309a011

43. Bonaccorso, F.; Sun, Z.; Hasan, T.; Ferrari, A. C. *Nat. Photonics* **2010,** *4,* 611–622. doi:10.1038/nphoton.2010.186

44. Ferrari, A. C. *Nanoscale* **2014,** *7,* 4598–4810. doi:10.1039/c4nr01600a

45. De, S.; Coleman, J. N. *MRS Bull.* **2011,** *36,* 774–781. doi:10.1557/mrs.2011.236

46. Tien, H.-W.; Huang, Y.-L.; Yang, S.-Y.; Wang, J.-Y.; Ma, C.-C. M. *Carbon* **2011,** *49,* 1550–1560. doi:10.1016/j.carbon.2010.12.022

License and Terms

Optimizing PMMA solutions to suppress contamination in the transfer of CVD graphene for batch production

Chun-Da Liao[1], Andrea Capasso[*1], Tiago Queirós[1,2], Telma Domingues[1,2], Fatima Cerqueira[2], Nicoleta Nicoara[1], Jérôme Borme[1], Paulo Freitas[1] and Pedro Alpuim[*1,2]

Abstract

Mass production and commercial adoption of graphene-based devices are held back by a few crucial technical challenges related to quality control. In the case of graphene produced by chemical vapor deposition, the transfer process represents a delicate step that can compromise device performance and reliability, thus hindering industrial production. In this context, the impact of poly(methyl methacrylate) (PMMA), the most common support material for transferring graphene from the Cu substrate to any target surface, can be decisive in obtaining reproducible sample batches. Although effective in mechanically supporting graphene during the transfer, PMMA solutions needs to be efficiently designed, deposited, and post-treated to serve their purpose while minimizing potential contaminations. Here, we prepared and tested PMMA solutions with different average molecular weight (AMW) and weight concentration in anisole, to be deposited by spin coating. Optical microscopy and Raman spectroscopy showed that the amount of PMMA residues on transferred graphene is proportional to the AMW and concentration in the solvent. At the same time, the mechanical strength of the PMMA layer is proportional to the AMW. These tests served to design an optimized PMMA solution made of a mixture of 550,000 (550k) and 15,000 (15k) AMW PMMA in anisole at 3% concentration. In this design, PMMA-550k provided suitable mechanical strength against breakage during the transfer cycles, while PMMA-15k promoted depolymerization, which allowed for a complete removal of PMMA residues without the need for any post-treatment. An XPS analysis confirmed the cleanness of the optimized process. We validated the impact of the optimized PMMA solution on the mass fabrication of arrays of electrolyte-gated graphene field-effect transistors operating as biosensors. On average, the transistor channel resistance decreased from 1860 to 690 Ω when using the optimized PMMA. Even more importantly, the vast majority of these resistance values are distributed within a narrow range (only ca. 300 Ω wide), in evident contrast with the scattered values obtained in non-optimized devices (about 30% of which showed values above 1 MΩ). These results prove that the optimized PMMA solution unlock the production of reproducible electronic devices at the batch scale, which is the key to industrial production.
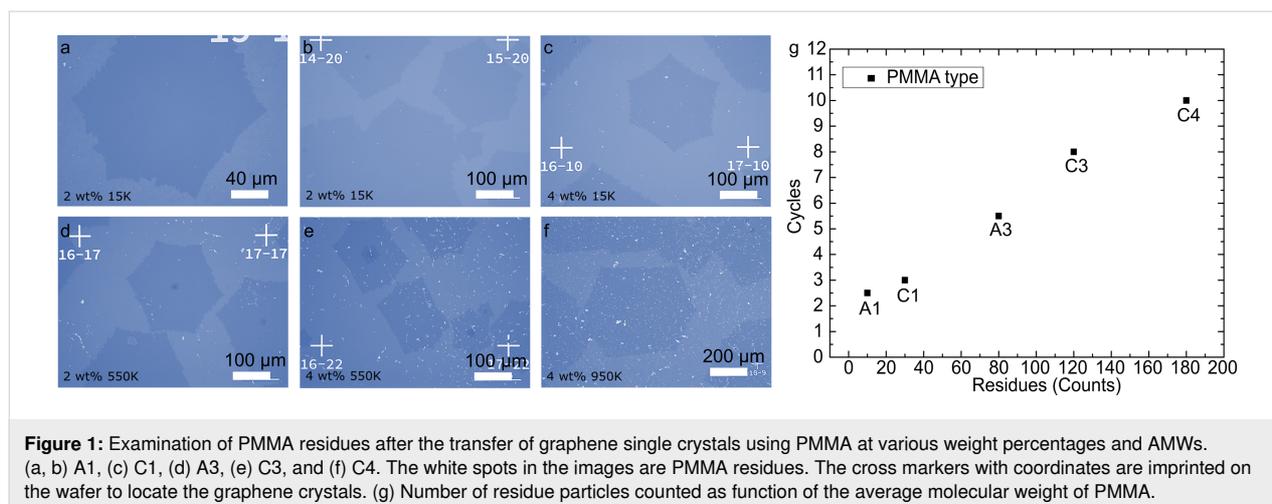
Introduction

Graphene and two-dimensional (2D) transition metal dichalcogenides (TMDCs) have been the focus of an intense research effort aimed at developing a new class of innovative devices and applications [1-3]. Among the production methods, chemical vapor deposition (CVD) made substantial progress over the years and now guarantees high-quality standards for the growth of batches of graphene samples over wafer-scale areas [4-6]. This progress allowed for the fabrication of a wide range of 2D material-based devices and heterostructures, especially in optoelectronics [7-9]. At present, one of the remaining challenges in the fabrication of graphene-based devices lies in the reproducibility: More than the CVD itself, the transfer process from the growth substrate (e.g., Cu or Ni) to the desired target substrate (e.g., SiO_2/Si, glass, or flexible polymers) often introduces inconsistencies among devices [10]. Various approaches have been developed to address this issue and establish a reproducible transfer process [11-17]. Among the many, the poly(methyl methacrylate) (PMMA)-assisted process remains the most reliable and most commonly used approach [18]. The chemical structure of PMMA features long polymer chains, whose length is proportional to the average molecular weight (AMW) of the polymer. During the transfer of graphene, the polymer serves as a supporting layer to (i) retain the integrity of graphene during the wet-etching bath required to dissolve the metallic substrate and (ii) provide mechanical stability when transferring graphene to the target substrates. During this process, two primary external sources of contamination need to be considered: (i) metallic particles from the Cu or Ni etching process and (ii) PMMA residues after the removal and rinsing processes. Both contaminations are leading causes of undesired p-type doping in CVD graphene, accompanied by a deterioration of its electrical properties [19-22]. The metallic contamination from etchants such as $FeCl_3$ can be substantially reduced by rinsing PMMA-coated graphene in DI water solution with 1–2% HCl [12]. Concerning the PMMA residues, several approaches were implemented to dissolve them, primarily by disrupting their chemical bonds. The chemical bond breakage is crucial, considering that PMMA solutions with higher weight percentage (wt %) are usually preferred as they form thicker supporting layers by spin coating: Such layers are mechanically more robust, yet leave behind significant residues [20]. Annealing processes (usually 200–450 °C, under an inert atmosphere or vacuum) were proposed [20], enabling depolymerization by breaking the molecular backbone bonds of PMMA [19,22,23]. Similarly, UV radiation can break the ester groups of PMMA, thus weakening the intermolecular interactions with graphene [24]. PMMA with higher AMW is harder to depolymerize due to strong van der Waals and London attractive forces among the long polymer chains [13]. It must also be considered that thermal treatments can often be counterproductive as they intensify polymerization, harden the PMMA residues, and complicate the removal.

Therefore, the way toward clean graphene processing appears to lie in the optimization of the PMMA-assisted transfer. In this context, we propose an optimized approach for a clean mass transfer of graphene samples over wafer-scale areas. A PMMA mixture was developed by balancing the AMW and weight percentage in anisole to guarantee a reliable transfer at a negligible contamination level, even without any post-treatment at high temperature. The supporting layer formed by spin coating presents high mechanical flexibility and strength for the transfer process and appears easy to dissolve afterward. We validated the impact of the optimized process in the mass fabrication of arrays of receded-gate graphene field-effect transistors for biosensing applications.

Results and Discussion

We transferred graphene by using PMMA with two AMWs (15k and 550k), which were dissolved in anisole at two weight ratios (2 and 4 wt %). PMMA with 950,000 (950k) AMW (at 4 wt %), commonly used for microfabrication processes as an e-beam resist, was used for further comparison (see Experimental section, "Graphene transfer"). Optical microscopy analysis was carried out to visually evaluate the presence of PMMA residues after the transfer process of graphene single crystals using PMMA with different weight percentages and AMWs (Figure 1a–g). As detailed in the description of the graphene transfer process, after the Cu etching process (Supporting Information File 1, Figure S1b, step II), the PMMA-coated graphene is rinsed in a DI water bath at least three times (Supporting Information File 1, Figure S1b, step III). Each cycle includes two actions, namely (i) scooping up the sample and (ii) releasing it into the water bath. After the rinse process, the sample must be moved to a target substrate, which takes one more transfer cycle. Therefore, the wet transfer process entails at least four cycles. A sufficiently high mechanical strength of the supporting PMMA layer is the key requirement for a successful transfer. Figure 1g shows our experimental observations on the cleanness level and maximum number of transfer cycles afforded by each PMMA solution. For statistical purposes, the number of cycles for each test was extended to eight by transferring the PMMA/graphene between two aqueous solutions. A1 and C1 PMMA solutions (see Table 1 below for the sample denominations) allowed for less than four cycles without breakage, demonstrating a low mechanical strength. The strength appears to reach a proper level for A3 PMMA, which allowed for up to six complete cycles. C3 and C4 PMMA provided the highest mechanical support, allowing for up to ten cycles. To evaluate the process cleanness, the residues were
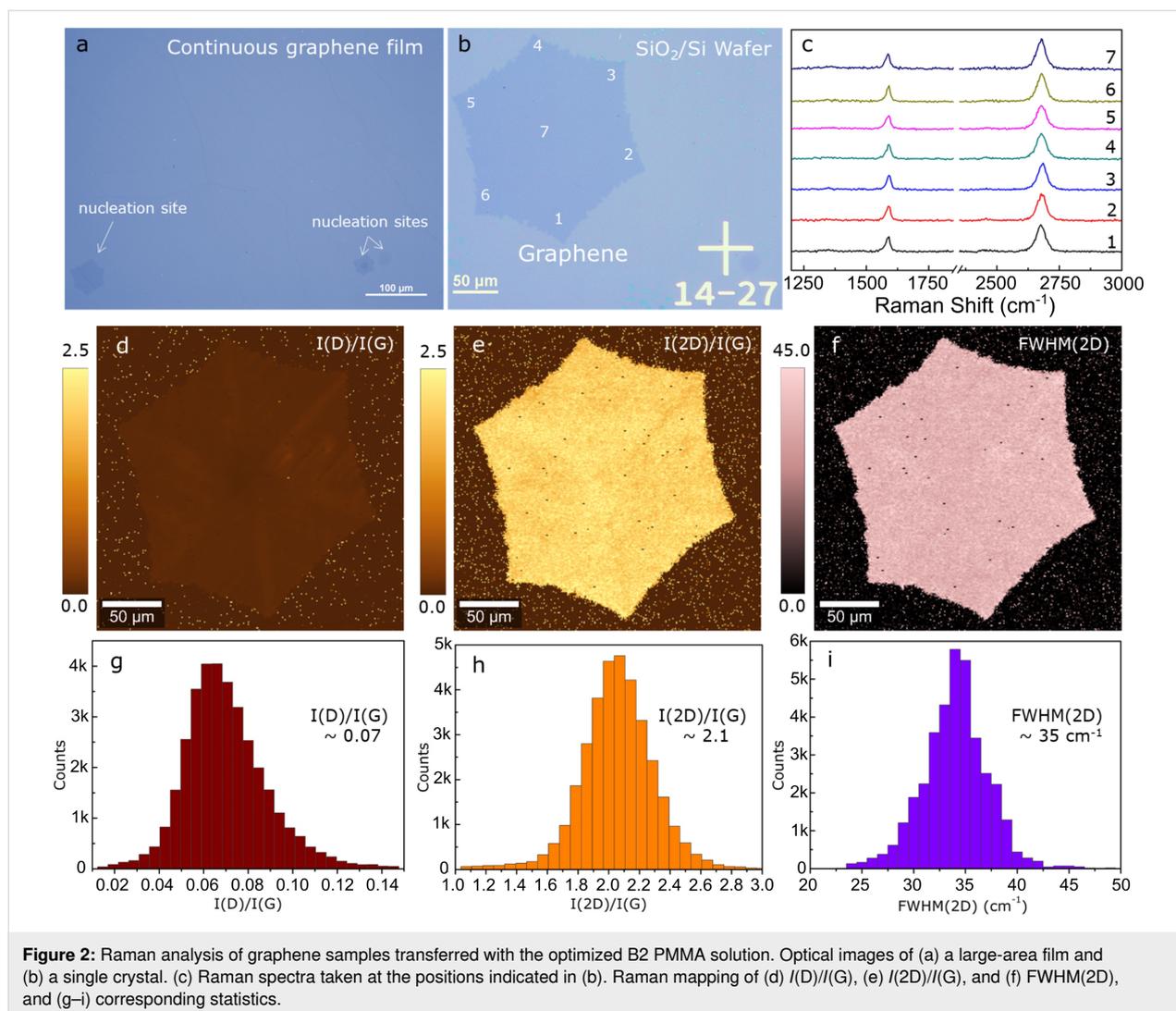
Figure 1: Examination of PMMA residues after the transfer of graphene single crystals using PMMA at various weight percentages and AMWs. (a, b) A1, (c) C1, (d) A3, (e) C3, and (f) C4. The white spots in the images are PMMA residues. The cross markers with coordinates are imprinted on the wafer to locate the graphene crystals. (g) Number of residue particles counted as function of the average molecular weight of PMMA.

quantified by counting the white spots (larger than 2.5 μm) in the images. Micrographs taken on 650×500 μm^2 areas were compared (Figure 1a–f). The amount of PMMA residues appears to be directly related to the PMMA concentration. A1 showed very little residues (they can be almost completely removed using acetone) and low mechanical strength, whereas C1 provided proper support while maintaining a low residue level. The length of the PMMA molecular chains (proportional to molecular weight and the attractive intermolecular force) appeared to be the determining factor in the mechanical strength (as demonstrated by C3 PMMA, enabling eight complete transfer cycles). Overall, all 550k samples provided strong mechanical support yet translated into a moderate-to-high residue density level. C4 revealed the densest residue distribution due to extended molecular chains and the highest mass concentration.

A PMMA mixture (coded B2, 3% mixture of PMMA-15k and PMMA-550k, see Table 1) was designed to lower the potential residue concentration while maintaining proper mechanical support. The rationale for the design of the optimized mixture is based on two hypotheses: (i) The PMMA-15k component provides short polymer chains, which are expected to diminish the molecular chain entanglement and, hence, the residue level. (ii) The sole presence of short polymer chains should, however, weaken the mechanical strength of the spin-coated layer. Therefore, the addition of PMMA-550k compensates for that and grants support during the transfer. B2 was tested in the transfer of both a graphene film and a single crystal (Figure 2a,b). The area analysis (650×500 μm^2) revealed less than ten residues, indicating an extremely clean transfer process. B2 PMMA allowed for up to six transfer cycles, representing an intermediate, yet acceptable, mechanical support. This proves that the PMMA mixture features good mechanical strength and cleanness (i.e., the acetone bath can thoroughly remove it). The transferred graphene samples were investigated via Raman spectros-

copy to evaluate crystallinity, layer number, and structural defect level [23]. The relative intensities of the G (ca. 1585 cm^{-1}) and 2D (ca. 2700 cm^{-1}) bands are typical of monolayer graphene [23-26]. The defect density appears minimal considering the negligible D band intensity at ca. 1350 cm^{-1} (Figure 2c) [27]. The Raman mapping in Figure 2d–i examines the whole crystal area [28]. The map and the corresponding statistics in Figure 2d and Figure 2g, respectively, show that the $I(D)/I(G)$ ratio is very low (down to 0.03), meaning that no or few defects could be detected. Figure 2e and Figure 2h show that over 95% of the sample has a ratio of $I(2D)/I(G) > 1.6$ (average of 2.1 ± 0.3) and a FWHM(2D) of 34.2 ± 3.0 cm^{-1} (Figure 2f,i), implying high-quality monolayer graphene. Together, the data further support uniformity and crystallinity of the sample.

The G phonon band arises from double degeneracy of iTO and iLO phonon modes (E_{2g} symmetry) at the Brillouin zone center, which is an in-plane vibration of sp^2 carbon atoms [23], and its position displays a blueshift as the charge carrier concentration rises. That is, the frequency shift of the G band is proportional to $|E_F|$, which sets the carrier concentration. Due to the method and materials employed for the graphene transfer being the same except for the PMMA mixture, we consider that the differences in Raman spectra between the different samples can be attributed to adsorbed PMMA residues. Such residues could absorb water and oxygen molecules, conferring p-type doping to graphene [29]. Conversely, by tracking the G phonon band features in Raman spectra, we can correlate the degree of doping in graphene [30,31] with PMMA residues. A comparison of the statistical data of the G band position and FWHM(G) of graphene transferred with C4 and B2 PMMA is presented in Figure 3. Representative Raman spectra for the two cases are shown in Figure 3a and Figure 3b, respectively. The comparison of Figure 3c and Figure 3d shows that the G peak position

Figure 2: Raman analysis of graphene samples transferred with the optimized B2 PMMA solution. Optical images of (a) a large-area film and (b) a single crystal. (c) Raman spectra taken at the positions indicated in (b). Raman mapping of (d) *I*(D)/*I*(G), (e) *I*(2D)/*I*(G), and (f) FWHM(2D), and (g–i) corresponding statistics.

is blueshifted in C4 samples compared to B2 samples (from an average of 1587 to 1593 cm^{-1}), indicating that the charge carrier concentration did not rise as much when using B2 PMMA. This shows that B2 leaves behind a much lower (if any) density of residues. This redshift observed upon reducing the PMMA residue concentration is consistent with studies on advanced methods for cleaning PMMA from graphene [32]. The average FWHM(G) for the C4 and B2 samples is 14 and 23 cm^{-1}, respectively (Figure 3e and Figure 3f). The broader G phonon band observed for the B2 samples reveals that a significantly higher number of inter-band decay pathways are available due to a lower Pauli blocking threshold [23] (equivalent to twice |E_F|), further indicating that the p-type doping caused by adsorbed PMMA is less intense for the B2 samples. This result again supports that employing B2 PMMA yields fewer residues and may help in avoiding post-transfer treatments for advanced PMMA residue cleaning of graphene, such as annealing and ion beam irradiation [32]. The graph of the G band shift (Support-

ing Information File 1, Figure S2a) confirms that C4 PMMA leaves the highest level of contamination. This case also shows the highest standard deviation of the G band shift and FWHM(G) (Supporting Information File 1, Figure S2a,b) due to heterogeneous doping levels in the sample. We explain these results by the higher variance in the proportions of PMMA residue aggregates, resulting in alternating regions of intensively local p-type doping (large PMMA aggregates) and regions of less intense p-doping (small PMMA aggregates). In contrast, PMMA mixtures with lighter AMWs showed lighter and more uniform p-type doping over the crystallite area (smaller error bars). Few-layer crystals transferred with B2 are analyzed in Supporting Information File 1, Figure S3. The graphene crystal in Supporting Information File 1, Figure S3a,b is composed of four layers having a thickness of 0.4–0.5 nm (Supporting Information File 1, Figure S3c) [28,33]. The crystal morphology appears very smooth and free of identifiable impurities, with an average surface roughness (R_a) of ca. 0.2 nm
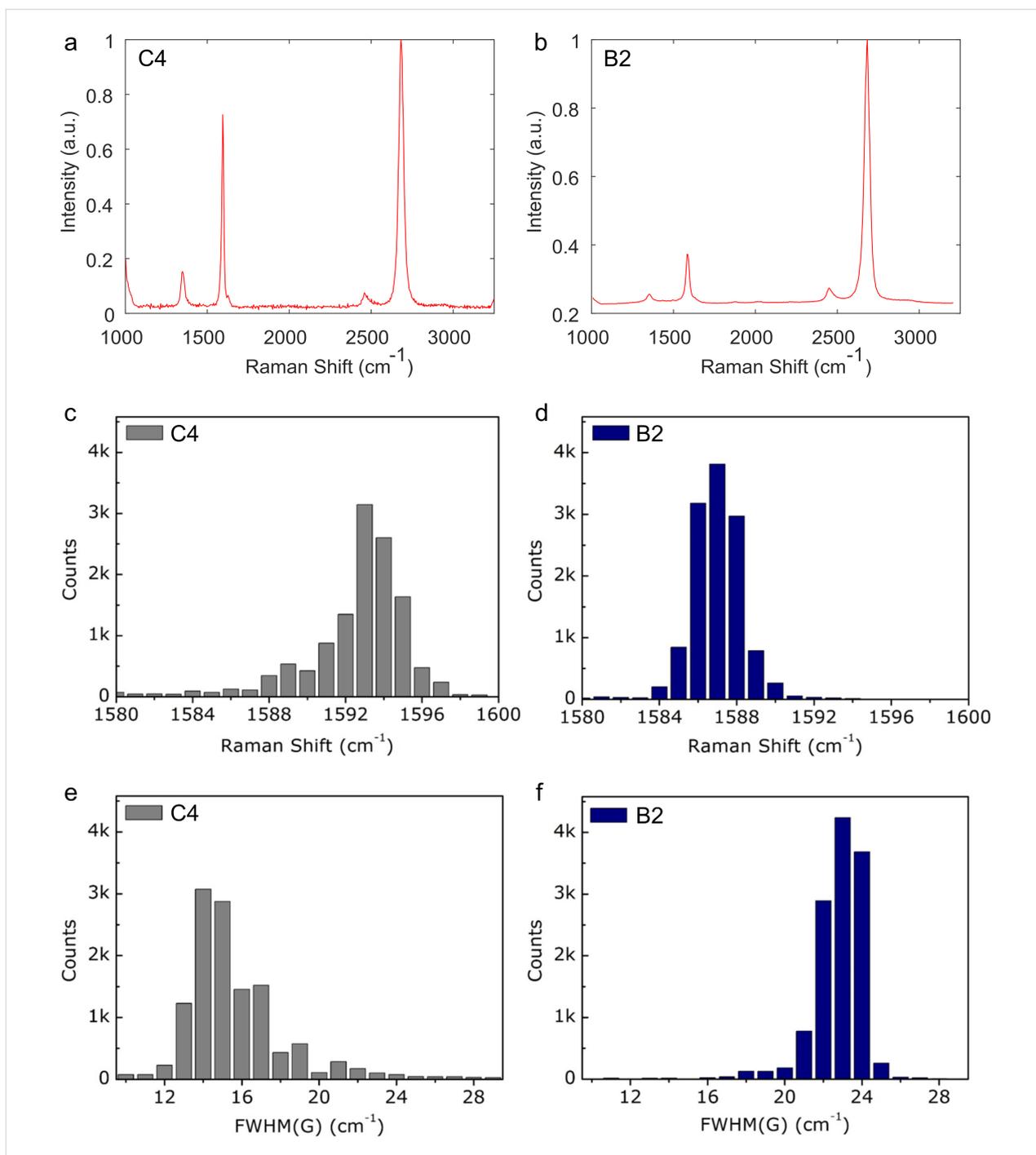
Figure 3: Statistical analysis of the Raman spectra of transistors prepared with transfers using PMMA mixtures with different molecular weights. (a, b) Representative Raman spectra of graphene transistor channels prepared using B2 and C4 mixtures, respectively. (c, d) Distributions of the G band peak position for B2 and C4, respectively. (e, f) Distributions of the FWHM of the G band.

(Supporting Information File 1, Figure S3d). This value is one order of magnitude lower than that of graphene crystals transferred with C4 PMMA, which showed a surface roughness of ca. 2.8 nm. The low roughness obtained with B2 PMMA can be also related to a minimal occurrence of nanometer-scale PMMA residues.
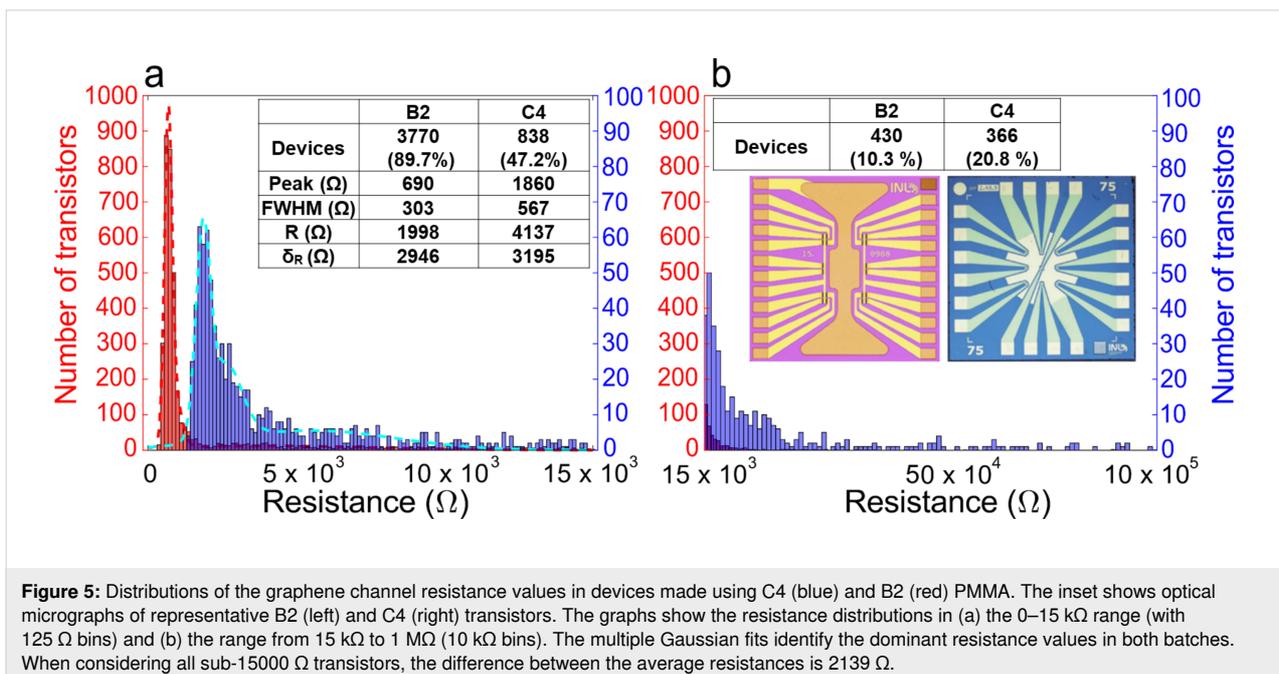
XPS was employed to analyze the graphene samples transferred using C4 and B2 PMMA (Figure 4). Figure 4a shows the chemical structure of the PMMA molecule. The C1s spectra can be decomposed into two prominent peaks originating from sp^2-hybridized C–C and sp^3-hybridized C–C/C–H bonds. Four PMMA-related peaks can be assigned to C–H, C–C, O–CH$_3$

Figure 4: (a) Representation of the molecular structure of PMMA. XPS C1s spectra of graphene samples transferred using (b) C4 and (c) B2. The normalized spectra are fitted by Gaussian–Lorentzian curves. The solid blue and grey fills identify, respectively, sp²- and sp³-hybridized carbon bonds in graphene, located at ca. 284.4 and 285.0 eV, respectively. C–H (blue line), C–C (purple line), O–CH₃ (pink line), and O–C=O (orange line) bonds are located at ca. 285.7, 286.3, 287.0 and 289.0 eV, respectively.

(methoxy functional group), and O–C=O (carboxy functional group) bonds, respectively [34-36]. PMMA residues on the graphene surface mainly feature three peaks resulting from C–C bonds and carbon–oxygen-related bonds (i.e., methoxy and carboxy functional groups). After PMMA has been removed in the acetone bath, the peak of the C–H bond can rarely be observed because of a broader merger with the peak of sp³-hybridized C–C/C–H bonds in graphene. In Figure 4b, the peak intensities of C–C, O–CH₃, and O–C=O bonds are, respectively, 17.6%, 14.6%, and 15.0% of the main peak intensity (sp² C–C). In Figure 4c, the same ratios decrease to, respectively, 2.9%, 2.6%, and 4.8%. Therefore, regarding O–C=O bonds, the

residue caused by B2 was reduced by three times and decreased about six times for the removal of C–C and O–CH₃ bonds, implying the crucial role of PMMA-15k in the mixture.

The optimized graphene transfer process was statistically validated in a batch fabrication context by comparing the channel resistance of electrolyte-gated graphene field-effect transistors (GFETs, Figure 5) designed to operate as DNA biosensors. Two batches of GFETs having a topmost graphene channel (75 μm width × 25 μm length) were fabricated (see details in Supporting Information File 1). In the first batch [37,38] (including 1755 GFETs), graphene was transferred with the C4 PMMA

Figure 5: Distributions of the graphene channel resistance values in devices made using C4 (blue) and B2 (red) PMMA. The inset shows optical micrographs of representative B2 (left) and C4 (right) transistors. The graphs show the resistance distributions in (a) the 0–15 kΩ range (with 125 Ω bins) and (b) the range from 15 kΩ to 1 MΩ (10 kΩ bins). The multiple Gaussian fits identify the dominant resistance values in both batches. When considering all sub-15000 Ω transistors, the difference between the average resistances is 2139 Ω.

mixture (see Section 2.2). The data acquired from the first batch were used to benchmark a successive test on a more extensive second batch [39,40] (4200 GFETs) that used B2 PMMA for the graphene transfer. Figure 5 shows the resistance distribution in the two cases. The distributions were fitted with multiple Gaussian curves to identify the predominant resistance values in each transistor batch. The first Gaussian curves of C4 and B2 (which envelop the most common resistance bins, see Figure 5) peak at 1860 and 690 Ω, respectively. This is a difference of 1170 Ω. The much lower channel resistance for the B2 mixture gives further evidence of a more robust, cleaner, and more effective transfer process. The B2 transfer appears to minimize the PMMA residues, known to act as centers of carrier scattering in graphene and to increase its resistance [19,20]. The vast majority (ca. 90%) of B2 data populate the first Gaussian curve with a narrow distribution (FWHM of ca. 300 Ω). In stark contrast, the C4 data are scattered over a much broader range. Almost 50% populate a broader Gaussian curve with two peaks (FWHM of the first peak: ca. 567 Ω) in the range up to 15 kΩ, while more than 20% have values up to 1 MΩ. Differently from B2, a consistent sample subset (above 30%) is above 1 MΩ, which means that a third of the fabricated devices are open circuits due to an imperfect graphene transfer (leading to highly damaged or lacking graphene). Overall, the B2 mixture yields more consistent electric properties of the graphene channel, thanks to a homogenous and reproducible process. Such characteristics ultimately translate into a consistent sensor performance, which is pivotal for industrial fabrication.

Conclusion

Monolayer graphene films and single crystals were transferred using PMMA with different AMWs and weight percentages in anisole. Repeated transfer cycles among water baths revealed, as expected, that PMMA with higher AMW and weight percentage allowed for a better mechanical support to graphene. Optical microscopy, Raman spectroscopy, and XPS carried out to evaluate the amount of PMMA residues on graphene after the transfer processes showed that PMMA with higher AMW resulted in a more significant number of residues: PMMA-950k AMW (C4) yielded a maximum of 180 residues (in a $650 \times 500\ \mu m^2$ area), while the optimized mixture (PMMA-15k/550k, B2) yield a minimum value of ten residues in the same area. More abundant PMMA contamination on graphene translated into a more intense p-type doping, as evidenced by (i) the position of the Raman G peak, which was blueshifted by ca. 6 cm^{-1} (between C4 and B2 samples), and (ii) the FWHM of the G peak, which appeared broader in B2 samples (23 cm^{-1} vs 14 cm^{-1} of the C4 samples). The XPS analysis showed a markedly increased presence of C–H, C–C, O–CH_3, and O–C=O bonds in C4 graphene compared to B2 samples, corroborating the previous findings. We validated the impact of the

optimized B2 process in the mass fabrication of arrays of electrolyte-gated GFETs. The channel resistances of thousands of GFETs prepared using B2 and C4 PMMA were measured with a probe station in air. The resistance distributions were analyzed and fitted with Gaussian curves. The resistance distributions were centered at 690 Ω (FWHM = 303 Ω) and 1860 Ω (FWHM = 567 Ω), respectively, proving that the optimized PMMA mixture enables the production of reproducible arrays of electronic devices with consistent properties.

Experimental
Graphene growth
Single-crystal and large-area graphene were obtained on Cu foil via catalyst-assisted growth in a low-pressure CVD system (CVD First Nano, EasyTube 3000). A 25 μm thick annealed Cu foil (Alfa Aesar, purity 99.8%), serving as a metal catalyst, was placed in a graphite enclosed cavity during the whole process. The temperature for annealing and growth was kept stable at 1040 °C by PID thermal controllers. The Cu foil was first annealed in argon atmosphere (500 sccm, 9.0 Torr) for 30 min in a quartz tube furnace. In the growth process, the gas mixture of argon (250 sccm), hydrogen (100 sccm), and methane (1.2 sccm) was subsequently introduced into the quartz chamber, where a reaction pressure of 4.0 Torr was kept constant through the variable frequency-driven pumping system. The growth time for single graphene crystals (250–350 μm) and large-area graphene films (ca. 25 cm^2) was 40 and 80 min, respectively. To finalize the process, an argon flush of 500 sccm was conducted to cool down samples until the furnace reached room temperature.

Graphene transfer
For the preparation of the various PMMA solutions, PMMA-15k (Sigma-Aldrich, 200336) and PMMA-550k (Alfa Aesar, 43982) powders were dissolved in anisole (Merck, 801452) in different proportions, as indicated in Table 1. PMMA-950k (MicroChem, PMMA-950k A4) at 4 wt % is commonly used for microfabrication processes and was chosen for comparison. The optimized PMMA mixture (coded B2) was made by mixing PMMA-550k and PMMA-15k in anisole at a 2:1 ratio (3 wt %). The solutions were stirred at 1000 rpm for 24 h. The graphene transfer process is illustrated in Supporting Information File 1, Figure S1. Graphene/Cu foil was spin-coated with PMMA at 3000 rpm for 30 s, followed by drying in a fume hood for 8 h. The back side graphene was removed by oxygen plasma (4×10^{-1} mbar, 250 W, 90 s).

PMMA/graphene/Cu foil was placed over the 0.5 M $FeCl_3$ solution surface for 3 h to etch away the Cu foil. After the etching process, PMMA/graphene floating on the surface of the $FeCl_3$ solution was rinsed with DI water three times. A rinse in 2%

Table 1: PMMA solutions used in the graphene transfer tests.

Name	Ratio (wt %)	Polymer AMW	Polymer wt %	Anisole mass (g)
A1	2	15,000	2	98
C1	4	15,000	4	96
A3	2	550,000	2	98
C3	4	550,000	4	96
C4	4	950,000	4	96
B2	3	15,000/550,000	1/2	97

HCl solution was done to remove metal precipitates. At last, the PMMA/graphene was washed in DI water three times and scooped up with a target substrate (SiO_2/Si wafer). The sample was dried in a vacuum chamber (ca. 10^{-4} Torr) at room temperature for 2 h. For PMMA removal, the entire sample was vertically dipped into an acetone bath for 4 h. After that, the exposed graphene on a SiO_2/Si substrate was again vertically dipped into IPA and then DI water bath for 1 h. Finally, the graphene on the receiving substrate was blow-dried with N_2.

Optical microscopy

A selective oxidation method was adopted to rapidly identify the as-grown graphene, enabling the direct optical inspection of the graphene domains without the laborious transfer process. Following this method, the Cu substrate with graphene was first oxidized in ambient air on a hot plate at 200 °C for 2 min. The graphene film on the Cu substrate serves as a protection layer, preventing the underlying Cu surface from oxidation because of its high chemical/thermal stability and impermeability to gases and liquids. In contrast, the surrounding exposed areas of the Cu foil surface exhibited high reactivity and were readily oxidized to copper oxides with a noticeable color change. The apparent color contrast between the oxidized and non-oxidized Cu surfaces made the synthesized graphene domains easy to be observed in an optical microscope equipped with a CCD camera (Supporting Information File 1, Figure S1a).

Raman spectroscopy

Large-area graphene films and single graphene crystals transferred onto SiO_2/Si substrates were characterized by Raman microscopy (WITec GmbH, Model: Alpha300M+) with an excitation laser wavelength of 532 nm. A laser power of ca. 2 mW was used for all measurements. The backscattered laser light containing the Raman bands from 1200 to 3000 cm^{-1} was collected by a CCD camera (Andor, Model number: DV401A-BV-352) integrated with the WITec system. The characteristic Raman signature collected from a p-doped Si wafer at 520.7 cm^{-1} was employed as standard calibration. Raman mapping was conducted by raster scan, where the step size of the laser spot moving over a selected area is 1 μm, and the exposure time of 0.4 s was taken at each point of the mapping. In the maps, the intensity of D and 2D bands were normalized to the G band intensity. Corresponding statistics were extracted from the maps.

X-ray photoelectron spectroscopy

The chemical components of PMMA residues were analyzed by X-ray photoelectron spectroscopy (XPS, Thermo Scientific ESCALAB 250Xi) using a non-monochromatic Mg Kα source with an analysis spot smaller than 2 mm^2. The detection system contains a double-focusing 180° spherical sector analyzer with a mean radius of 150 mm and an energy range of 0 to 5 keV. The pressure in the analysis chamber was ca. 5×10^{-10} Torr, and the analyzer had a pass energy of 20 eV.

Atomic force microscopy

The surface topographies of graphene were investigated by a Bruker Dimension Icon atomic force microscope (AFM), using PPP-NCH (NanosensorsTM) cantilevers with a tip radius smaller than 20 nm, a force constant of 42 N/m, and 250 kHz resonance frequency. The AFM measurement was carried out in tapping mode. A 633 nm laser light aimed at the back side of the cantilever tip was reflected toward a position-sensitive photodetector, which provides feedback signals to piezoelectric scanners that maintain the cantilever tip at constant height (force) above the surface, thus, reproducing its topography.

Fabrication and characterization of graphene field-effect transistors

Receded-gate graphene field-effect transistors were fabricated on an 8″ Si/SiO_2 (200 nm thick) wafers. Two arrays of devices were fabricated with different process steps (Wafer 1: C4 PMMA; Wafer 2: B2 PMMA). Both wafers started with the patterning of Cr/Au contacts (deposited by magnetron sputtering) using direct-write laser lithography and ion milling. The fabrication of the two wafers followed slightly different steps, as described below.

Wafer 1: A stopping layer (Al_2O_3/TiWN/AlSiCu/TiWN) was patterned by lift-off, followed by the CVD growth of a multi-stack layer of SiO_2 and Si_3N_4 to passivate the current lines. After this, a thin Al_2O_3 layer was deposited by sputtering and patterned by wet etching to protect the gate during the graphene etch. The C4 PMMA/graphene films were then transferred onto the patterned wafer until all device areas were covered. After removing the PMMA, graphene was patterned using optical lithography and oxygen plasma etching. Finally, the sacrificial layer was removed by wet etching.

Wafer 2: An additional layer of Al_2O_3 was deposited on the Au layer as protection. After that, the two wafers followed different fabrication processes. A residue-free transfer process was used, using a sacrificial metallic mask (TiWN, AlSiCu, TiWN) patterned by lift-off to protect the entire wafer except for the areas around the channel, source, and drain, on which the graphene film would make electrical contact. The B2 PMMA/graphene films were then transferred onto the wafer and patterned by O_2 plasma, followed by the sacrificial layer removal. Previous to the passivation, Al_2O_3 was selectively removed to improve the adhesion of the oxide passivation to the surface of the chips. A stopping layer (Cu/AlSiCu/TiW) for the reactive ion etching (RIE) process was sputtered, and the SiO_2/SiN_x multistack passivation layer was deposited by CVD. The passivation layer was patterned by lithography and etched by RIE until revealing the stopping layer on the contact pads and graphene transistor channels. Finally, the stopping layer was removed by wet etching, exposing the graphene channel.

In both wafers, the GFET channels had nominal dimensions of $W = 75$ µm and $L = 25$ µm. The total number of GFETs condidered in this study was 1755 on Wafer 1 and 4200 on Wafer 2. The source–drain resistance of the GFETs was measured with a semi-automatic DC measurement probe station for 8″ wafers. The setup uses a 40-tip probe head with 250 µm spacing between the tips; each probe allowed us to measure 20 devices simultaneously. A current was injected into each transistor to reach an output voltage of 1 mV. Histogram distributions for the graphene channel resistances were plotted (using MATLAB scripts) to compare the effects of B2 and C4 PMMA-assisted graphene transfer on device performance. Based on our observations of the device performance, a threshold resistance of 15000 Ω was selected as the cut-off resistance value identifying working graphene channels (i.e., correctly operating devices). A maximum resistance value of 1 MΩ was set to identify the non-operating channels (due to imperfect transfer leading to heavily damaged or lacking graphene). Multiple Gaussian fits were performed to isolate the trends in the resistance distributions.

Supporting Information

Supporting Information File 1
Additional experimental data.
[https://www.beilstein-journals.org/bjnano/content/supplementary/2190-4286-13-70-S1.pdf]

Funding

ORCID® iDs

Andrea Capasso - https://orcid.org/0000-0003-0299-6764
Tiago Queirós - https://orcid.org/0000-0001-6765-7793
Pedro Alpuim - https://orcid.org/0000-0001-9875-6188

Preprint

A non-peer-reviewed version of this article has been previously published as a preprint: https://doi.org/10.3762/bxiv.2022.42.v1

References

1. Butler, S. Z.; Hollen, S. M.; Cao, L.; Cui, Y.; Gupta, J. A.; Gutiérrez, H. R.; Heinz, T. F.; Hong, S. S.; Huang, J.; Ismach, A. F.; Johnston-Halperin, E.; Kuno, M.; Plashnitsa, V. V.; Robinson, R. D.; Ruoff, R. S.; Salahuddin, S.; Shan, J.; Shi, L.; Spencer, M. G.; Terrones, M.; Windl, W.; Goldberger, J. E. *ACS Nano* **2013,** *7,* 2898–2926. doi:10.1021/nn400280c
2. Geim, A. K.; Grigorieva, I. V. *Nature* **2013,** *499,* 419–425. doi:10.1038/nature12385
3. Novoselov, K. S.; Mishchenko, A.; Carvalho, A.; Castro Neto, A. H. *Science* **2016,** *353,* aac9439. doi:10.1126/science.aac9439
4. Obraztsov, A. N. *Nat. Nanotechnol.* **2009,** *4,* 212–213. doi:10.1038/nnano.2009.67
5. Hao, Y.; Bharathi, M. S.; Wang, L.; Liu, Y.; Chen, H.; Nie, S.; Wang, X.; Chou, H.; Tan, C.; Fallahazad, B.; Ramanarayan, H.; Magnuson, C. W.; Tutuc, E.; Yakobson, B. I.; McCarty, K. F.; Zhang, Y.-W.; Kim, P.; Hone, J.; Colombo, L.; Ruoff, R. S. *Science* **2013,** *342,* 720–723. doi:10.1126/science.1243879

6. Chen, C.-C.; Kuo, C.-J.; Liao, C.-D.; Chang, C.-F.; Tseng, C.-A.; Liu, C.-R.; Chen, Y.-T. *Chem. Mater.* **2015,** *27,* 6249–6258. doi:10.1021/acs.chemmater.5b01430

7. Han, T.-H.; Lee, Y.; Choi, M.-R.; Woo, S.-H.; Bae, S.-H.; Hong, B. H.; Ahn, J.-H.; Lee, T.-W. *Nat. Photonics* **2012,** *6,* 105–110. doi:10.1038/nphoton.2011.318

8. Britnell, L.; Ribeiro, R. M.; Eckmann, A.; Jalil, R.; Belle, B. D.; Mishchenko, A.; Kim, Y.-J.; Gorbachev, R. V.; Georgiou, T.; Morozov, S. V.; Grigorenko, A. N.; Geim, A. K.; Casiraghi, C.; Neto, A. H. C.; Novoselov, K. S. *Science* **2013,** *340,* 1311–1314. doi:10.1126/science.1235547

9. Gomez De Arco, L.; Zhang, Y.; Schlenker, C. W.; Ryu, K.; Thompson, M. E.; Zhou, C. *ACS Nano* **2010,** *4,* 2865–2873. doi:10.1021/nn901587x

10. Chen, M.; Haddon, R. C.; Yan, R.; Bekyarova, E. *Mater. Horiz.* **2017,** *4,* 1054–1063. doi:10.1039/c7mh00485k

11. Liang, X.; Sperling, B. A.; Calizo, I.; Cheng, G.; Hacker, C. A.; Zhang, Q.; Obeng, Y.; Yan, K.; Peng, H.; Li, Q.; Zhu, X.; Yuan, H.; Hight Walker, A. R.; Liu, Z.; Peng, L.-m.; Richter, C. A. *ACS Nano* **2011,** *5,* 9144–9153. doi:10.1021/nn203377t

12. Kim, S. M.; Hsu, A.; Lee, Y.-H.; Dresselhaus, M.; Palacios, T.; Kim, K. K.; Kong, J. *Nanotechnology* **2013,** *24,* 365602. doi:10.1088/0957-4484/24/36/365602

13. Kim, S.; Shin, S.; Kim, T.; Du, H.; Song, M.; Lee, C.; Kim, K.; Cho, S.; Seo, D. H.; Seo, S. *Carbon* **2016,** *98,* 352–357. doi:10.1016/j.carbon.2015.11.027

14. Lin, Y.-C.; Lu, C.-C.; Yeh, C.-H.; Jin, C.; Suenaga, K.; Chiu, P.-W. *Nano Lett.* **2012,** *12,* 414–419. doi:10.1021/nl203733r

15. Borin Barin, G.; Song, Y.; de Fátima Gimenez, I.; Souza Filho, A. G.; Barreto, L. S.; Kong, J. *Carbon* **2015,** *84,* 82–90. doi:10.1016/j.carbon.2014.11.040

16. Capasso, A.; De Francesco, M.; Leoni, E.; Dikonimos, T.; Buonocore, F.; Lancellotti, L.; Bobeico, E.; Sarto, M. S.; Tamburrano, A.; De Bellis, G.; Lisi, N. *Appl. Phys. Lett.* **2014,** *105,* 113101. doi:10.1063/1.4895733

17. Ullah, S.; Yang, X.; Ta, H. Q.; Hasan, M.; Bachmatiuk, A.; Tokarska, K.; Trzebicka, B.; Fu, L.; Rummeli, M. H. *Nano Res.* **2021,** *14,* 3756–3772. doi:10.1007/s12274-021-3345-8

18. Qing, F.; Zhang, Y.; Niu, Y.; Stehle, R.; Chen, Y.; Li, X. *Nanoscale* **2020,** *12,* 10890–10911. doi:10.1039/d0nr01198c

19. Suk, J. W.; Lee, W. H.; Lee, J.; Chou, H.; Piner, R. D.; Hao, Y.; Akinwande, D.; Ruoff, R. S. *Nano Lett.* **2013,** *13,* 1462–1467. doi:10.1021/nl304420b

20. Pirkle, A.; Chan, J.; Venugopal, A.; Hinojos, D.; Magnuson, C. W.; McDonnell, S.; Colombo, L.; Vogel, E. M.; Ruoff, R. S.; Wallace, R. M. *Appl. Phys. Lett.* **2011,** *99,* 122108. doi:10.1063/1.3643444

21. Ahn, Y.; Kim, H.; Kim, Y.-H.; Yi, Y.; Kim, S.-I. *Appl. Phys. Lett.* **2013,** *102,* 091602. doi:10.1063/1.4794900

22. Jeong, H. J.; Kim, H. Y.; Jeong, S. Y.; Han, J. T.; Baeg, K.-J.; Hwang, J. Y.; Lee, G.-W. *Carbon* **2014,** *66,* 612–618. doi:10.1016/j.carbon.2013.09.050

23. Malard, L. M.; Pimenta, M. A.; Dresselhaus, G.; Dresselhaus, M. S. *Phys. Rep.* **2009,** *473,* 51–87. doi:10.1016/j.physrep.2009.02.003

24. Ferrari, A. C.; Basko, D. M. *Nat. Nanotechnol.* **2013,** *8,* 235–246. doi:10.1038/nnano.2013.46

25. Pimenta, M. A.; Dresselhaus, G.; Dresselhaus, M. S.; Cançado, L. G.; Jorio, A.; Saito, R. *Phys. Chem. Chem. Phys.* **2007,** *9,* 1276–1290. doi:10.1039/b613962k

26. Faggio, G.; Capasso, A.; Messina, G.; Santangelo, S.; Dikonimos, T.; Gagliardi, S.; Giorgi, R.; Morandi, V.; Ortolani, L.; Lisi, N. *J. Phys. Chem. C* **2013,** *117,* 21569–21576. doi:10.1021/jp407013y

27. Lisi, N.; Buonocore, F.; Dikonimos, T.; Leoni, E.; Faggio, G.; Messina, G.; Morandi, V.; Ortolani, L.; Capasso, A. *Thin Solid Films* **2014,** *571,* 139–144. doi:10.1016/j.tsf.2014.09.040

28. Gnisci, A.; Faggio, G.; Messina, G.; Kwon, J.; Lee, J.-Y.; Lee, G.-H.; Dikonimos, T.; Lisi, N.; Capasso, A. *J. Phys. Chem. C* **2018,** *122,* 28830–28838. doi:10.1021/acs.jpcc.8b10094

29. Ni, Z. H.; Wang, H. M.; Luo, Z. Q.; Wang, Y. Y.; Yu, T.; Wu, Y. H.; Shen, Z. X. *J. Raman Spectrosc.* **2010,** *41,* 479–483. doi:10.1002/jrs.2485

30. Das, A.; Pisana, S.; Chakraborty, B.; Piscanec, S.; Saha, S. K.; Waghmare, U. V.; Novoselov, K. S.; Krishnamurthy, H. R.; Geim, A. K.; Ferrari, A. C.; Sood, A. K. *Nat. Nanotechnol.* **2008,** *3,* 210–215. doi:10.1038/nnano.2008.67

31. Wu, J.-B.; Lin, M.-L.; Cong, X.; Liu, H.-N.; Tan, P.-H. *Chem. Soc. Rev.* **2018,** *47,* 1822–1873. doi:10.1039/c6cs00915h

32. Zhuang, B.; Li, S.; Li, S.; Yin, J. *Carbon* **2021,** *173,* 609–636. doi:10.1016/j.carbon.2020.11.047

33. Capasso, A.; Dikonimos, T.; Sarto, F.; Tamburrano, A.; De Bellis, G.; Sarto, M. S.; Faggio, G.; Malara, A.; Messina, G.; Lisi, N. *Beilstein J. Nanotechnol.* **2015,** *6,* 2028–2038. doi:10.3762/bjnano.6.206

34. Ton-That, C.; Shard, A. G.; Teare, D. O. H.; Bradley, R. H. *Polymer* **2001,** *42,* 1121–1129. doi:10.1016/s0032-3861(00)00448-1

35. Ferrah, D.; Renault, O.; Petit-Etienne, C.; Okuno, H.; Berne, C.; Bouchiat, V.; Cunge, G. *Surf. Interface Anal.* **2016,** *48,* 451–455. doi:10.1002/sia.6010

36. Cunge, G.; Ferrah, D.; Petit-Etienne, C.; Davydova, A.; Okuno, H.; Kalita, D.; Bouchiat, V.; Renault, O. *J. Appl. Phys.* **2015,** *118,* 123302. doi:10.1063/1.4931370

37. Campos, R.; Borme, J.; Guerreiro, J. R.; Machado, G., Jr.; Cerqueira, M. F.; Petrovykh, D. Y.; Alpuim, P. *ACS Sens.* **2019,** *4,* 286–293. doi:10.1021/acssensors.8b00344

38. Motoso Abreu, C. F. Biosensors for Enhanced in Vitro Fertilisation Outcomes. Ph.D. Thesis, Swansea University, Swansea, UK, 2019.

39. Cabral, P. D.; Domingues, T.; Machado, G., Jr.; Chicharo, A.; Cerqueira, F.; Fernandes, E.; Athayde, E.; Alpuim, P.; Borme, J. *Materials* **2020,** *13,* 5728. doi:10.3390/ma13245728

40. Purwidyantri, A.; Domingues, T.; Borme, J.; Guerreiro, J. R.; Ipatov, A.; Abreu, C. M.; Martins, M.; Alpuim, P.; Prado, M. *Biosensors* **2021,** *11,* 24. doi:10.3390/bios11010024

Liquid phase exfoliation of talc: effect of the medium on flake size and shape

Samuel M. Sousa[‡1], Helane L. O. Morais[‡1], Joyce C. C. Santos[2],
Ana Paula M. Barboza[3], Bernardo R. A. Neves[4], Elisângela S. Pinto[5]
and Mariana C. Prado[*3]

Full Research Paper

Open Access

Address:
[1]Campus Santa Luzia, Instituto Federal de Minas Gerais, R. Érico Veríssimo, 317, Santa Luzia – MG, 33115-390, Brazil, [2]Centro de Desenvolvimento da Tecnologia Nuclear CDTN/CNEN, Avenida Antônio Carlos, 6627, Belo Horizonte, Minas Gerais 31270-901, Brazil, [3]Physics Department, Universidade Federal de Ouro Preto, R. Diogo de Vasconcelos, 122, Ouro Preto – MG, 35400-000, Brazil, [4]Physics Department, Universidade Federal de Minas Gerais, Avenida Antônio Carlos, 6627, Belo Horizonte – MG, 31270-901, Brazil and [5]Campus Ouro Preto, Instituto Federal de Minas Gerais, R. Pandiá Calógeras, 898, Ouro Preto – MG, 35400-000, Brazil

Email:
Mariana C. Prado[*] - mariana.prado@ufop.edu.br

* Corresponding author   ‡ Equal contributors

Abstract

Industrial applications of nanomaterials require large-scale production methods, such as liquid phase exfoliation (LPE). Regarding this, it is imperative to characterize the obtained materials to tailor parameters such as exfoliation medium, duration, and mechanical energy source to the desired applications. This work presents results of statistical analyses of talc flakes obtained by LPE in four different media. Talc is a phyllosilicate that can be exfoliated into nanoflakes with great mechanical properties. Sodium cholate at two different concentrations (below and at the critical micelar concentration), butanone, and Triton-X100 were employed as exfoliation medium for talc. Using recent published statistical analysis methods based on atomic force microscopy images of thousands of flakes, the shape and size distribution of nanotalc obtained using the four different media are compared. This comparison highlights the strengths and weaknesses of the media tested and hopefully will facilitate the choice of the medium for applications that have specific requirements.

Introduction

Two-dimensional (2D) materials have attracted a lot of interest due to their outstanding properties [1]. However, large-scale production is still a challenge that needs to be addressed to integrate 2D materials into industrial applications. One approach to producing large quantities of few-layer flakes of a broad range of exfoliatable materials is liquid-phase exfoliation (LPE) [2-5].

This method relies on mechanical energy to exfoliate materials in an appropriate liquid medium. To exfoliate a material of interest, it must be reduced to a fine powder and mixed with a liquid that serves as an exfoliation medium. The solution is exposed to a mechanical energy source that leads to the delamination of the material, resulting in a suspension of nanosheets [6]. The energy may be provided by an ultrasonic bath, a shear force mixer, or a tip sonicator. The solution serves three purposes: it provides a medium to propagate the mechanical energy, suspends the exfoliated nanosheets, and prevents them from agglomerating again. The versatility of the method allows it to be employed to obtain nanoflakes of a collection of materials such as graphene [3,7], hexagonal boron nitride [8], transition metal dichalcogenides [9], and others [10,11].

Although the experimental setup is generally designed as described before [6], numerous parameters must be adjusted to optimize the exfoliation for a given material and the available experimental setup. The exfoliation medium must be chosen correctly to guarantee the optimum result. And one must keep in mind that completely separating the nanoflakes from the solution might not be an easy task, if possible at all. So, if the flakes can be obtained in an application-friendly medium, it will greatly facilitate the process.

In this study, we addressed the implications of the choice of medium for shape and size of talc nanoflakes obtained by LPE. This material is a hydrated magnesium silicate belonging to the phyllosilicate group [12]. Phyllosilicates are crystalline minerals with a basic Si_2O_5 composition that exhibit a layer structure, making them ideal candidates for mechanical exfoliation. Talc already has several industrial applications [12], ranging from polymer and ceramics fillers [13-16] to pharmaceutical and cosmetics uses [17]. It was shown that monolayer talc has outstanding mechanical properties of the same order of magnitude as graphene [12]. The breaking strength for uniaxial deformations ranges from 29 to 33 N·m^{-1}, and the two-dimensional elasticity modulus is $E = 181$ N·m^{-1}. Also, talc's flexural rigidity is about three times that of graphene but it can be bent to small curvatures without fracturing. These properties make nanoscale talc a promising candidate for the application [14,15,18] as reinforcement for polymers and other composites, including biocompatible materials, and van der Waals heterostructures. Being able to scale the production is a crucial step to realizing applications at an industrial level. We present the results of liquid-phase exfoliation of talc using different liquid media, namely sodium cholate aqueous solution (6 mg/mL and 1 mg/mL), Triton X-100 aqueous solution, and butanone. The mechanical energy necessary to delaminate the mineral was provided by an ultrasonic bath. We report a statistical analysis of the dimensions (measured by atomic force microscopy) of

the nanoflakes obtained employing the four routes, evidencing that the exfoliation medium has an important influence on flake size and shape and should be accounted for when designing a production route with the desired application in mind.

Results and Discussion
Choice of exfoliation medium

Four exfoliation media were employed in this work, as summarized in Table 1. The first one was an aqueous solution of sodium cholate (SC) at 6 mg/mL, previously employed in the literature [11]. SC is a bile salt ionic surfactant widely employed in LPE [6,19-21]. While it is less toxic than other organic compounds usually employed for the same purpose, such as *N*-methyl-pyrrolidone (NMP), it is expensive and can leave residues on exfoliated flakes. Although fundamental to LPE, the role of the concentration and chemical composition of the exfoliation medium is still not fully understood [6]. Bearing that in mind, we also tested SC at a much lower concentration of 1 mg/mL. The critical micelle concentration (CMC) of SC at room temperature ranges from 5.2 to 6.5 mg/mL [22]. The dilute solution is guaranteed to be well below the CMC, which is regarded as preferable [6]. To guarantee that the effects seen in flake size after exfoliation were not due to a change in the relative concentration of SC to talc, we also added less talc powder to the solution, to keep the ratio constant. We also tested the nonionic surfactant Triton-X100. Besides the absence of charged groups, compared to SC, Triton-X100 is also less expensive, although not environmentally friendly either. Finally, we tested an organic solvent, namely butanone. Butanone is volatile and has a boiling point of approximately 80 °C, making it the easiest medium to remove after exfoliation of the four employed here. Also, unlike other organic solvents commonly used in LPE, for example, NMP or dimethylformamide (DMF), that have a higher boiling point, butanone leaves less residues when exfoliated flakes are deposited onto substrates for atomic force microscopy (AFM) measurements. Table 1 summarizes the solutions tested here, and details of the sample preparation can be found in the Experimental section.

Table 1: Initial concentration of talc and surfactants/organic solvents for exfoliation.

| Sample	Exfoliation medium	Talc concentration
SC6	sodium cholate/DI water 6 mg/mL	6 mg/mL
SC1	sodium cholate/DI water 1mg/mL	1 mg/mL
Triton	Triton-X100/DI water 1 mg/mL	6 mg/mL
butanone	butanone (pure)	6 mg/mL

Liquid exfoliation of talc

Talc powder was exfoliated in each liquid medium by exposure to mechanical energy provided by an ultrasonic bath (full details in the Experimental section). Talc was manually milled down to a fine powder and characterized by X-ray diffraction (XRD). Figure 1a displays the results. All peaks are assigned to talc, when compared with the crystallographic database, and many are labeled. The insert shows the structure and chemical formula of talc [23]. Figure 1b shows the mineral that was milled to a fine powder. The powder was mixed with the exfoliation medium and subjected to mechanical energy provided by an ultrasonic bath (Figure 1c).

Centrifugation was performed to separate non-exfoliated material from nanometer-sized flakes. To analyze the influence of the exfoliation medium on shape and size of the nanoflakes obtained by LPE, we carefully chose acceleration and duration of the centrifugation. Thick flak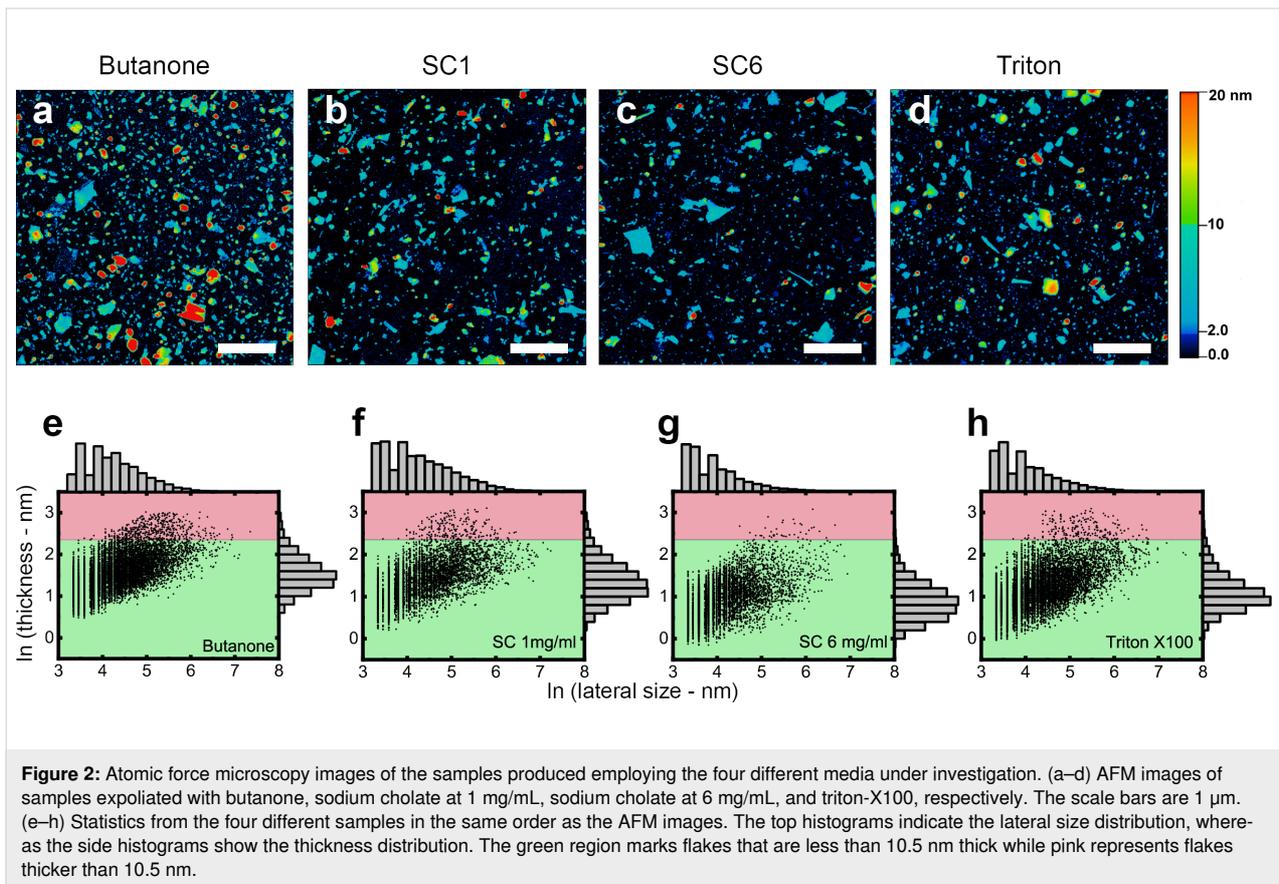es (>100 nm) must be removed to implement a semi-automated analysis of thousands of flakes based on AFM images that provide a robust statistical representation of the sample [24,25]. At the same time, the removal of flakes that are few to tens of nanometers thick would make the effect of exfoliation medium on size and shape less evident. Therefore, a single centrifugation step of one hour only at 1000*g* was employed. Such low acceleration will not produce a monolayer-rich solution [26], which is crucial for the analysis we aim to perform.

Atomic force microscopy characterization of flake size

Figure 2 shows the results obtained for each exfoliation medium. Figure 2a–d shows AFM topographical images of samples exfoliated in butanone, SC1, SC6, and Triton-X100, respectively. A single vertical scale was chosen to facilitate the visualization of flakes of different thicknesses in all samples. The substrate appears in black to dark blue. Following previous works,
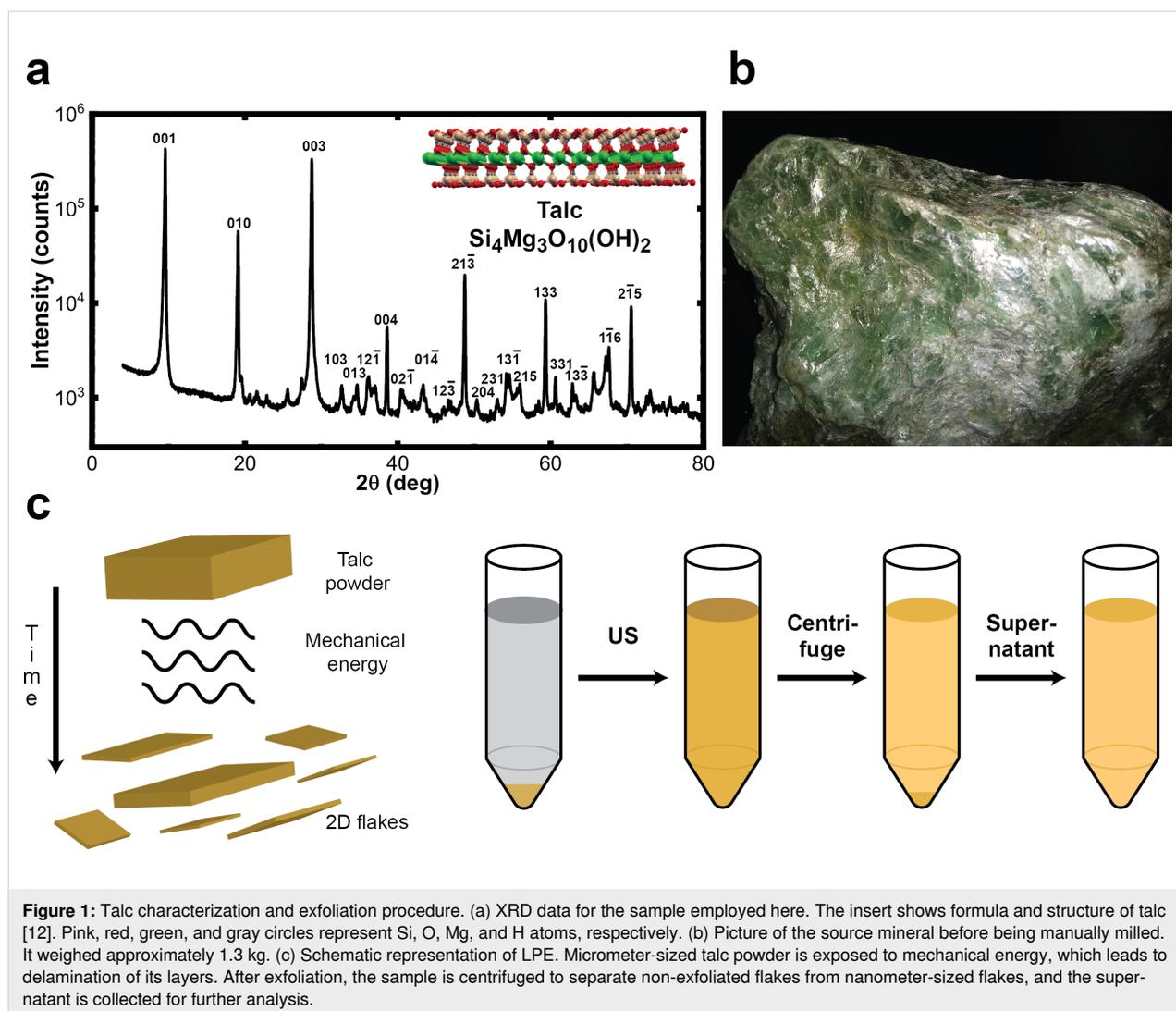
Figure 1: Talc characterization and exfoliation procedure. (a) XRD data for the sample employed here. The insert shows formula and structure of talc [12]. Pink, red, green, and gray circles represent Si, O, Mg, and H atoms, respectively. (b) Picture of the source mineral before being manually milled. It weighed approximately 1.3 kg. (c) Schematic representation of LPE. Micrometer-sized talc powder is exposed to mechanical energy, which leads to delamination of its layers. After exfoliation, the sample is centrifuged to separate non-exfoliated flakes from nanometer-sized flakes, and the supernatant is collected for further analysis.

Figure 2: Atomic force microscopy images of the samples produced employing the four different media under investigation. (a–d) AFM images of samples expoliated with butanone, sodium cholate at 1 mg/mL, sodium cholate at 6 mg/mL, and triton-X100, respectively. The scale bars are 1 µm. (e–h) Statistics from the four different samples in the same order as the AFM images. The top histograms indicate the lateral size distribution, whereas the side histograms show the thickness distribution. The green region marks flakes that are less than 10.5 nm thick while pink represents flakes thicker than 10.5 nm.

we consider flakes with ten or less layers as "few-layer" [25]. Since talc has a layer thickness of approximately 1 nm [12], we did not convert the height to the number of layers as it is a direct conversion. Few-layer flakes appear in light blue. Flakes that are thicker than 10 nm and thinner than 20 nm appear in green, yellow, and orange shades. Red represents everything of 20 nm thickness or thicker.

It is easy to see that all four exfoliation media produced samples mainly consisting of few-layer flakes (thinner than 10.5 nm, accounting for a thicker first layer and/or exfoliation medium residue [6,24]). At the same time, even without an in-depth analysis, it is clear that the medium has a very important influence on the flake size distribution. The sample exfoliated in sodium cholate at 6 mg/mL has visually fewer flakes in the pink region of the distribution graphics (Figure 2e–h). Butanone seems to have yielded a less dispersed distribution of flakes, although with higher thicknesses than other media.

Table 2 provides statistical parameters for the four samples. To characterize the lateral size of the flakes, the so-called Feret diameter was employed (the maximum Feret diameter of a flake, F, is the largest distance between two parallel tangential lines in any in-plane direction of a flake) [27]. It would be simple to

conclude that sodium cholate at 6 mg/mL produces the sample with the smallest mean flake thickness (h) and lateral size. If one desires a sample aimed at an application where flake thickness is critical and monolayers and bilayers are preferable, at a first glance, this would be the SC6 sample. However, much more information can be obtained using the procedures proposed by the authors of [24].

Table 2: Comparison of four different talc LPE samples. The total number of flakes analyzed, mean height (h) and its standard deviation (σ_h), mean lateral size (Feret diameter, F), and its standard deviation (σ_F), are shown.

Medium	No.	$<h>$ (nm)	σ_h (nm)	$<F>$ (nm)	σ_F (nm)
But.	11458	5.2	2.5	90	84
SC1	6286	4.5	2.6	100	106
SC6	8405	2.7	1.5	60	71
Triton	16494	3.4	2.0	77	84

As discussed by Fernandes and co-workers [24], simply looking at mean flake thickness and standard deviation of a sample does not account well for the volume (or mass) of few-layer flakes versus bulk flakes (thicker than 10.5 nm for talc, which repre-

sents 10 or more layers). We calculated the mass ratio of bulk (*M*) and few-layer (*m*) flakes. This ratio is defined as follows:

$$\frac{M}{m} = \frac{p_n\left(1-p_v\right)}{p_v\left(1-p_n\right)}, \qquad (1)$$

where p_n is the probability of a randomly picked flake being a few-layer flake and p_v is the volume fraction of few-layer flakes. See Supporting Information of [24] for details on the calculation.

The sample with the smallest *M*/*m* ratio is SC1 (5.6), followed by butanone (11.6) and Triton-X100 (16.6). Surprisingly, the sample with the highest ratio is SC6 (40.5). This can be understood in light of the meaning of the mass ratio. For every few-layer flake in the SC6 sample, the bulk flakes will correspond to a mass of ca. 41 few-layer flakes. Since the few-layer flakes are very small in this sample (thickness and Feret diameter), a bulk flake weights the same as many small flakes. This has serious implications for applications that demand few-layer flakes.

Centrifugation at higher accelerations can remove bulk flakes changing the parameters obtained here. An interesting hypothesis discussed in recent works [25,28] is that centrifugation might also lead to the loss of the smallest flakes along with the large ones due to drag effects. Flakes of the SC6 sample would be very susceptible to this effect, and a single centrifugation step at high acceleration should be avoided.

Topological vector analysis

To further investigate the differences between samples exfoliated in different media, we use now the methodology proposed in [25]. Figure 3a shows a 3D graphic representation of all the flakes in the four samples (several thousand flakes were analyzed for each case). We characterize size and shape of each flake considering its average thickness (*h*), maximum Feret diameter (Feret), and minimum Feret diameter (MinF, the smallest distance between two tangential parallel lines in any in-plane direction of a flake [27]). Recapping the discussion made by the authors who also use some of the methodology proposed by Chacham and colleagues [28], using AFM data we calculate three dimensionless aspect ratios:

$$r_h = \frac{h}{\sqrt[3]{V}}, \, r_{Feret} = \frac{Feret}{\sqrt[3]{V}}, \, r_{MinF} = \frac{MinFeret}{\sqrt[3]{V}}. \qquad (2)$$

Next, we plotted the probability distributions of the logarithm of these aspect ratios, $\ln(r_h)$, $\ln(r_{Feret})$, and $\ln(r_{MinF})$. Figure 3b–d shows the distribution histograms of these values for all four different exfoliation media under investigation here. The distri-

butions are skewed and best described by the exponentially modified Gaussian (EMG) distribution [25]. The probability density function of the EMG distribution is given by:

$$f\left(x;\mu,\sigma,\lambda\right) = \frac{\lambda}{2}e^{\frac{\lambda}{2}\left(2\mu+\lambda\sigma^2-2x\right)}\left[1-erf\left(\frac{\mu+\lambda\sigma^2-x}{\sqrt{2}\sigma}\right)\right], \quad (3)$$

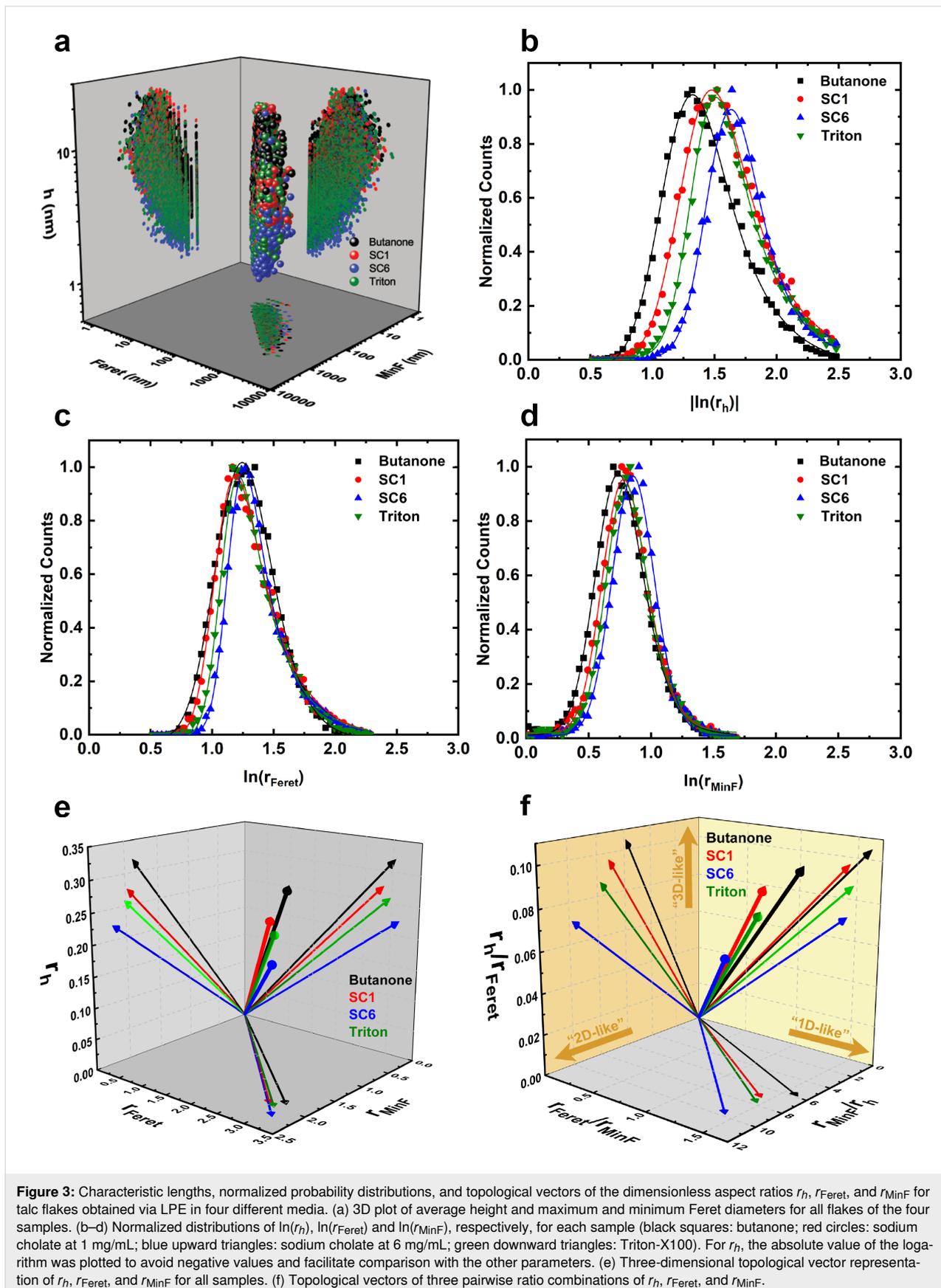where μ and σ are the mean and the variance of the Gaussian distribution and λ is the exponential decay rate; erf(*x*) is the error function. The applicability of this distribution and further details are discussed in a previous work [25].

As can be seen in Figure 3b–d, an EMG function fitted the data very well with $R^2 > 0.99$. The thickness parameter distribution is the widest one for all samples while the minimum lateral diameter (MinFeret) one is the narrowest and most symmetrical of all three parameters. This was observed and discussed before for talc and graphene samples [25].

Using the most probable value (mode) as the representative value for each of the three dimensionless aspect ratios, we constructed the topological vector representation of each sample (Figure 3e). This representation is very useful since it immediately brings out the differences between each sample. The projections of the vector in the planes readily offer a comparison of the characteristics of the sample. The samples differ more in thickness-related parameters (thus, the number of layers) than in the lateral size-related parameters.

To further compare shape-related features of the samples, we plotted topological vectors of pairwise ratios among these components (Figure 3f) [26]. The arrows in Figure 3f emphasize the meaning of the ratios. The r_h/r_{Feret} axis correlates with the voluminosity of a flake, that is, a greater the value indicates a more three-dimensional shape of the sample. A greater value of the r_{Feret}/r_{MinF} axis indicates a more ribbon-shaped flake, that is, a more one-dimensional shape. Finally, greater values of the r_{MinF}/r_h axis indicate a more plate-shaped flake, that is, a more two-dimensional shape.

The four media investigated here clearly produce samples with different shape characteristics. SC6 flakes are the most two-dimensional, while those exfoliated with butanone are the least two-dimensional, having a more 3D shape than all other samples. It is interesting to note that the SC1 and Triton-X100 samples are very alike. The dilution of sodium cholate has an important influence on the shape of the exfoliated flakes. Since the talc concentration was also diminished to keep the mass ratio between surfactant and talc constant, the effect must be due to the surfactant arrangement (i.e., the presence or absence of mo-

Figure 3: Characteristic lengths, normalized probability distributions, and topological vectors of the dimensionless aspect ratios r_h, r_{Feret}, and r_{MinF} for talc flakes obtained via LPE in four different media. (a) 3D plot of average height and maximum and minimum Feret diameters for all flakes of the four samples. (b–d) Normalized distributions of $\ln(r_h)$, $\ln(r_{Feret})$ and $\ln(r_{MinF})$, respectively, for each sample (black squares: butanone; red circles: sodium cholate at 1 mg/mL; blue upward triangles: sodium cholate at 6 mg/mL; green downward triangles: Triton-X100). For r_h, the absolute value of the logarithm was plotted to avoid negative values and facilitate comparison with the other parameters. (e) Three-dimensional topological vector representation of r_h, r_{Feret}, and r_{MinF} for all samples. (f) Topological vectors of three pairwise ratio combinations of r_h, r_{Feret}, and r_{MinF}.

lecular aggregates) and a higher relative amount of dispersion medium (the water-to-talc ratio is larger in the SC1 sample).

As stressed by Santos and colleagues [25], shape and size are different things. The previous analysis of bulk versus few-layer flakes is very important to complement the topological vectors just discussed because having a 2D shape does not mean that the flake has few layers. A bulk flake that has a thickness much smaller than both lateral parameters is 2D-shaped but behaves like the bulk material and not like mono-layer or few-layer flakes.
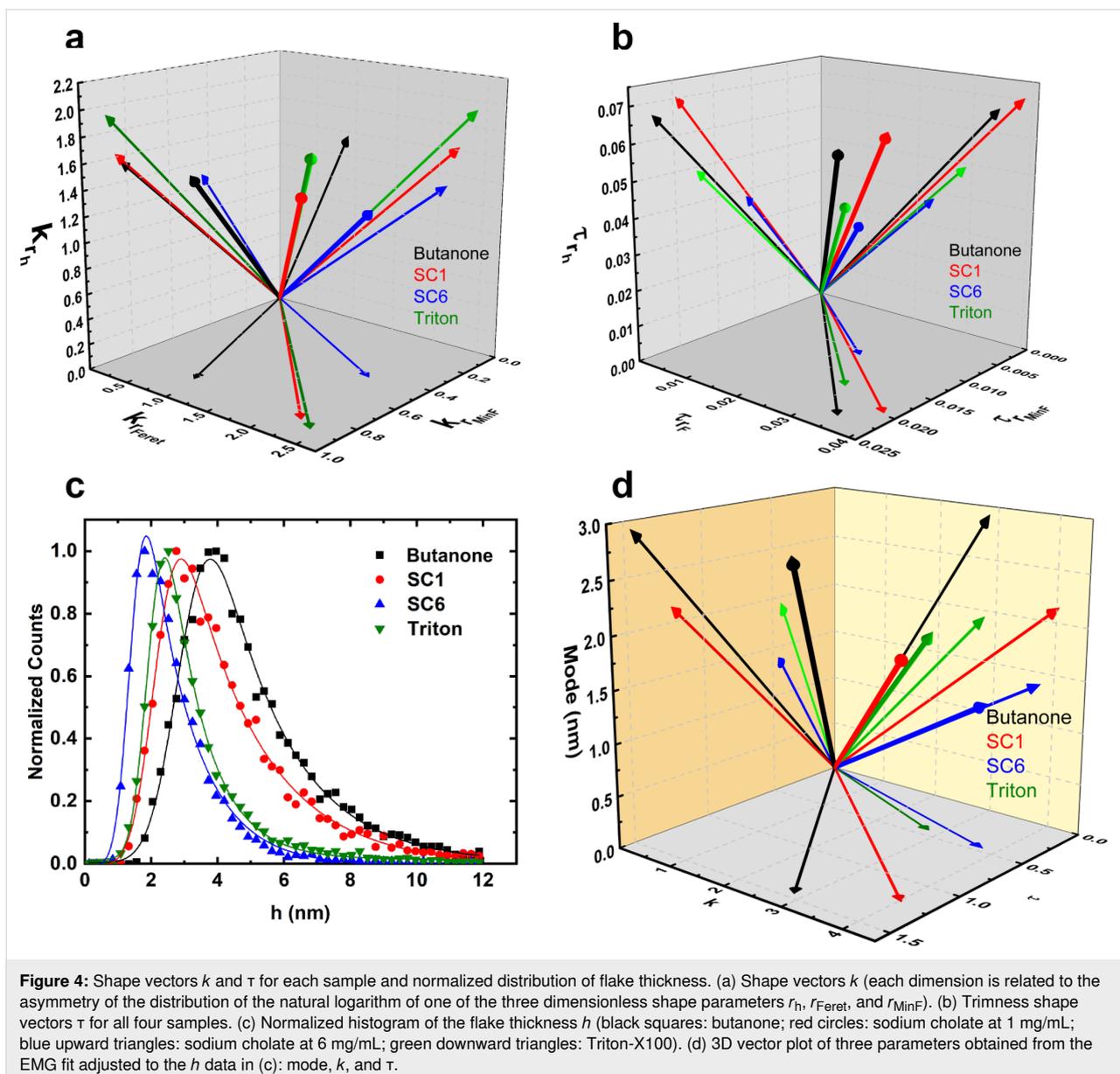
Adding to the discussion, let us consider the asymmetry of the distribution curve for each sample. A Gaussian distribution is

symmetric while the EMG is not; it is possible to characterize this asymmetry by calculating two shape parameters, k (asymmetry) and τ (trimness), both functions of σ and λ:

$$k = (\sigma\lambda)^{-1} \tag{4}$$

$$\tau = \frac{\sigma}{\lambda} \tag{5}$$

An in-depth discussion of these can be found elsewhere [25,29]. Figure 4a,b displays the topological vectors constructed for each sample for k and τ. Starting with the k shape vectors, the

Figure 4: Shape vectors k and τ for each sample and normalized distribution of flake thickness. (a) Shape vectors k (each dimension is related to the asymmetry of the distribution of the natural logarithm of one of the three dimensionless shape parameters r_h, r_{Feret}, and r_{MinF}). (b) Trimness shape vectors τ for all four samples. (c) Normalized histogram of the flake thickness h (black squares: butanone; red circles: sodium cholate at 1 mg/mL; blue upward triangles: sodium cholate at 6 mg/mL; green downward triangles: Triton-X100). (d) 3D vector plot of three parameters obtained from the EMG fit adjusted to the h data in (c): mode, k, and τ.

most symmetric distribution regarding r_h (thickness) was observed for the SC6 sample. Butanone and SC1 samples have a very similar asymmetry and Triton-X100 is the most asymmetrical of all four samples (thicker flakes cause the tail of the distribution to be more prominent). Exfoliation in butanone also results in a more symmetric distribution of the r_{Feret} parameter and again, SC1 and Triton-X100 samples are very similar, with SC6 being the most asymmetrical of all four samples. Regarding the distribution of r_{MinF}, in contrast, the SC6 sample is the most symmetrical.

For the trimness parameter, τ (Figure 4b), a small value indicates a more symmetric and narrow distribution. The SC6 sample has the most trimmed distribution for all dimensionless shape parameters of all four samples. SC1 and butanone exhibit similar values (less trimmed) and Triton-X100 lies in between.

Finally, let us add to the initial flake size discussion by analyzing the flake thickness distribution instead of the dimensionless parameters. The normalized histograms of flake thickness for all four samples (Figure 3c) are well adjusted by the EMG probability density function (Equation 3). The thickness distribution is clearly asymmetric. Thicker flakes resulting in the tail of the curve have not been removed by the low-acceleration centrifugation. The mean flake thickness values have the same trend as the mean values displayed in Table 2: $h_{SC6} < h_{Triton\text{-}X100} < h_{SC1} < h_{butanone}$. For the SC6 sample, the most common flake would be a bilayer talc flake.

For symmetry analysis, Figure 4d adds to what can be seen in Figure 4c with vectorial representation of mode, k, and τ for the h distribution of all four samples. Triton-X100 and SC6 have the most trimmed distributions while the most symmetrical are those of butanone and Triton X-100. All comparisons can be found in Table 3.

Finally, let us analyze advantages and drawbacks of each sample. An aqueous solution of 6 mg/mL sodium cholate is a widely recommended medium for liquid exfoliation [6,11]. For talc, it does yield the sample with the lowest average flake thickness (2.7 nm). However, it has the largest M/m ratio. The flakes are usually very small. Thus, many small flakes are required to compensate for the mass of rare but existing larger flakes. This means that while the number of thin flakes greatly exceeds the number of bulky ones, the mass of the latter is considerably large. Regarding the symmetry of the dimensionless shape parameters, the flakes of the SC6 sample are the most symmetrical, except for r_{Feret}, for which they are the second most symmetric. The SC6 flakes are also the ones with the most prominent 2D shape, that is, the flakes are more plate-like than those of all other samples. All this makes this sample appropriate for applications in which monolayers and bilayers are required and flakes are all similar in a narrow range of 2D shapes.

The SC1 sample with more water added to the sample (sodium cholate and talc concentrations are reduced to 1 mg/mL) makes the average flake thickness increase to 4.5 nm. Also, it drastically brings down the M/m ratio (by more than seven times). It also makes the distribution of shape and size parameters less symmetrical. Nevertheless, this sample is well suited for applications that require thin flakes (mostly not a single layer) and the overall mass of talc to be mostly constituted of thin flakes. It should be stressed that SC is very difficult to remove from the exfoliated sample and applications using this solution must tolerate SC residues.

To avoid exfoliation medium residues, organic solvents of low boiling points could be used. Butanone was tested here and

Parameter	Meaning	Order
mean flake thickness	lower values indicate thinner flakes	SC6 < Triton-X100 < SC1 < butanone
M/m	lower values indicate that fewer small flakes are needed to account for the mass of a large bulky flake	SC1 < butanone < Triton-X100 < SC6
k_{rh}	lower values indicate more symmetrical distributions	SC6 < butanone < SC1 < Triton-X100
k_{rFeret}	lower values indicate more symmetrical distributions	butanone < SC6 < SC1 < Triton-X100
k_{rMinF}	lower values indicate more symmetrical distribution	SC6 < butanone < SC1 < Triton-X100
τ_{rh}	lower values indicate more trimmed distribution	SC6 < Triton-X100 < butanone < SC1
τ_{rFeret}	lower values indicate more trimmed distribution	SC6 < Triton-X100 < butanone < SC1
τ_{rMinF}	lower values indicate more trimmed distribution	SC6 < Triton-X100 < SC1 < butanone
k_h	lower values indicate more symmetrical distribution	Triton-X100 < butanone < SC6 < SC1
τ_h	lower values indicate more symmetrical distribution	Triton-X100 < SC6 < SC1 < butanone

Table 3: Summary of the analysis for all four samples.

yields the largest mean flake thickness (5.2 nm). This is almost the double that of the SC6 sample, but it is still in the few-layer range. The *M*/*m* ratio is the second smallest, indicating that most of the mass of the sample is from few-layer flakes. The distribution of the shape parameters is fairly symmetric compared to the other samples but not very trimmed. The flakes are the most 3D-like ones, meaning they are more voluminous than other samples. Overall, if removability of the extraction medium is critical and few layers are required without the need for most flakes being monolayers, butanone is a good option.

Triton X-100 is also a widely employed surfactant for LPE. Since it is a nonionic surfactant, it is compatible with materials with surface charges. It is less expensive than SC and yields a sample with an average thickness of 3.4 nm, the second lowest one. Its *M*/*m* ratio is only smaller than that of the SC6 sample. However, it is about 2.4 times smaller, making it a good candidate for applications that require few-layer flakes predominating in number and in mass at the same time. It is the least symmetrical sample regarding the shape parameters, but it is fairly trimmed and the most symmetrical in flake size distribution.

Conclusion

A thorough characterization of flake size and shape was performed for samples of liquid-phase exfoliated talc in four different media. LPE is a robust, scalable production route to obtain 2D nanomaterials from minerals. However, many parameters need to be adjusted to obtain a product suitable for a given application. Here, the choice of the medium was addressed while other parameters (mechanical energy source, exfoliation time, centrifugation acceleration and duration, and sample deposition) were kept constant. Four different media were employed to exfoliate talc. Aqueous solutions of sodium cholate at 1 and 6 mg/mL (with the talc powder concentration adapted to keep the cholate/talc ratio constant), an aqueous solution of Triton-X100, and pure butanone.

The exfoliation medium has an influence on flake size and shape and should be chosen according to the desired application. Implications go beyond the mean number of layers of the flakes (all four media yielded few-layer-rich solutions). Flake size (variance and asymmetry of distribution), few-layer-to-bulk mass ratio, and 1D/2D/3D shape characteristics also varied.

Table 3 gives a summary of the efficiency of each medium in producing flakes with the listed size and shape features. Our procedure puts to use previously published flake analysis methodology, highlighting the importance of obtaining information on thousands of flakes and using appropriate statistical descriptions to analyze the data.

Experimental

Materials. Talc was obtained through a donation of a sample from Minas Gerais state, Brazil. X-ray diffraction (XRD) was performed to characterize the sample composition. The rock was manually milled to a fine powder. Sodium cholate and Triton-X100 were purchased from Sigma-Aldrich and used as received. All organic solvents were of analytical grade and used as received. Deionized water (resistivity 18.2 MΩ·cm) from a milliQ system was used for solution preparation. AFM measurements were performed on silicon substrates with an oxide layer, Si/SiO$_x$. Substrates were functionalized with (3-aminopropyl)triethoxysilane (APTES) following the procedure reported by Fernandes and co-workers [24].

X-ray diffraction. XRD was performed in a Rigaku Geigerflex 2037 diffractometer with a graphite monochromator using Cu Kα radiation (1.54056 Å) in the Bragg–Brentano geometry (θ/2θ).

Talc liquid-phase exfoliation. Before submitting the material to the liquid exfoliation process, a purification step was performed to remove any contaminations [11]. Talc powder was sonicated for 1 h in chloroform and then the solution was left to decant. The supernatant was discarded, and the process was repeated with acetone and water. Finally, the powder was collected and dried for 12 h at 60 °C in an oven. The purified talcum powder was placed in an aqueous solution of the surfactant of choice (or pure butanone) (Table 1). For sodium cholate (SC), 6 mg/mL (concentrated) and 1 mg/mL (diluted) solutions in DI water were prepared. Talcum powder was added to the surfactant solutions at 1 mg talc to 1 mL of diluted SC solution and 6 mg talc to 1 mL of concentrated SC solution. Triton-X100 solutions were 1 mg/mL. Butanone was used pure as received. For Triton-X100 and butanone, talc was added at 6 mg/mL. Glass vials containing the solutions were placed in an ultrasonic bath (Elma, S10H) for 15 h. The water bath temperature was monitored and controlled by adding ice to keep it below 40 °C if required. The resulting solutions were centrifuged at 1000*g* for 1 h (Multifuge X3R Thermo Scientific) to remove non-exfoliated material [26]. All analyses were performed with the collected supernatant. Purified talc powder of the same batch was used to prepare different medium samples to ensure the starting material was the same. All exfoliation parameters and material were kept as equal as possible to ensure that the differences of the flakes were associated to the medium influence and not to any other parameter.

AFM measurements. Sample preparation for AFM measurements followed the procedure designed by Fernandes et al. [24] and Santos and co-workers [25]. In short, a solution (1:40) of APTES in DI water was prepared. Si/SiO$_x$ substrates were

immersed in the solution for 15 min. Subsequently, each substrate was rinsed with DI water and blown dry with pure N_2 five times to ensure the removal of any residual APTES molecules. This step is crucial to ensure that talc flakes of all sizes adhere to the substrate and do not stack. Talc deposition is achieved employing spread coating of the solution onto the functionalized substrate. A drop that covers all the substrate is deposited on the surface and allowed to be in contact with it for 30 to 60 s to ensure optimal coverage. Then the sample is rinsed again in DI water to remove loose flakes and residual surfactant. An in-depth discussion of this procedure can be found in [24].

AFM measurements were performed on a Park XE-70 microscope, in intermittent contact mode using commercial silicon probes (MikroMasch, HQ:NSC35/AlBs or HQ:NSC36/AlBs). For each sample, nine different 5 μm × 5 μm fields were chosen at random and scanned at 0.5 Hz with 500 pixels/line (lateral resolution of 10 nm/pixel). Image processing (line and plane corrections) and flake counting [24] was performed using Gwyddion [30] and ImageJ software, respectively. The standard particle analysis toolbox available in ImageJ was employed to obtain the flake dimensions.

Acknowledgements

Funding

ORCID® iDs

Samuel M. Sousa - https://orcid.org/0000-0001-5050-3341
Helane L. O. Morais - https://orcid.org/0000-0003-2362-6949
Joyce C. C. Santos - https://orcid.org/0000-0002-6355-1083
Ana Paula M. Barboza - https://orcid.org/0000-0002-1807-971X
Bernardo R. A. Neves - https://orcid.org/0000-0003-0464-4754
Elisângela S. Pinto - https://orcid.org/0000-0002-8531-2470
Mariana C. Prado - https://orcid.org/0000-0003-0472-2433

References

1. Tan, C.; Cao, X.; Wu, X.-J.; He, Q.; Yang, J.; Zhang, X.; Chen, J.; Zhao, W.; Han, S.; Nam, G.-H.; Sindoro, M.; Zhang, H. *Chem. Rev.* **2017,** *117,* 6225–6331. doi:10.1021/acs.chemrev.6b00558

2. Smith, R. J.; King, P. J.; Lotya, M.; Wirtz, C.; Khan, U.; De, S.; O'Neill, A.; Duesberg, G. S.; Grunlan, J. C.; Moriarty, G.; Chen, J.; Wang, J.; Minett, A. I.; Nicolosi, V.; Coleman, J. N. *Adv. Mater. (Weinheim, Ger.)* **2011,** *23,* 3944–3948. doi:10.1002/adma.201102584

3. Paton, K. R.; Varrla, E.; Backes, C.; Smith, R. J.; Khan, U.; O'Neill, A.; Boland, C.; Lotya, M.; Istrate, O. M.; King, P.; Higgins, T.; Barwich, S.; May, P.; Puczkarski, P.; Ahmed, I.; Moebius, M.; Pettersson, H.; Long, E.; Coelho, J.; O'Brien, S. E.; McGuire, E. K.; Sanchez, B. M.; Duesberg, G. S.; McEvoy, N.; Pennycook, T. J.; Downing, C.; Crossley, A.; Nicolosi, V.; Coleman, J. N. *Nat. Mater.* **2014,** *13,* 624–630. doi:10.1038/nmat3944

4. Nicolosi, V.; Chhowalla, M.; Kanatzidis, M. G.; Strano, M. S.; Coleman, J. N. *Science* **2013,** *340,* 1226419. doi:10.1126/science.1226419

5. Coleman, J. N.; Lotya, M.; O'Neill, A.; Bergin, S. D.; King, P. J.; Khan, U.; Young, K.; Gaucher, A.; De, S.; Smith, R. J.; Shvets, I. V.; Arora, S. K.; Stanton, G.; Kim, H.-Y.; Lee, K.; Kim, G. T.; Duesberg, G. S.; Hallam, T.; Boland, J. J.; Wang, J. J.; Donegan, J. F.; Grunlan, J. C.; Moriarty, G.; Shmeliov, A.; Nicholls, R. J.; Perkins, J. M.; Grieveson, E. M.; Theuwissen, K.; McComb, D. W.; Nellist, P. D.; Nicolosi, V. *Science* **2011,** *331,* 568–571. doi:10.1126/science.1194975

6. Backes, C.; Higgins, T. M.; Kelly, A.; Boland, C.; Harvey, A.; Hanlon, D.; Coleman, J. N. *Chem. Mater.* **2017,** *29,* 243–255. doi:10.1021/acs.chemmater.6b03335

7. Giovannetti, R.; Rommozzi, E.; Zannotti, M.; D'Amato, C. A.; Ferraro, S.; Cespi, M.; Bonacucina, G.; Minicucci, M.; Di Cicco, A. *RSC Adv.* **2016,** *6,* 93048–93055. doi:10.1039/c6ra07617c

8. Wang, H.; Su, X.; Song, T.; Li, Z.; Zhao, Y.; Lou, H.; Wang, J. *Appl. Surf. Sci.* **2019,** *488,* 656–661. doi:10.1016/j.apsusc.2019.05.296

9. Kedawat, G.; Kumar, P.; Nagpal, K.; Paul, S. J.; Singh, V. N.; Kumar, S. S.; Gupta, B. K. *ChemistrySelect* **2019,** *4,* 6219–6226. doi:10.1002/slct.201901325

10. Hanlon, D.; Backes, C.; Doherty, E.; Cucinotta, C. S.; Berner, N. C.; Boland, C.; Lee, K.; Harvey, A.; Lynch, P.; Gholamvand, Z.; Zhang, S.; Wang, K.; Moynihan, G.; Pokle, A.; Ramasse, Q. M.; McEvoy, N.; Blau, W. J.; Wang, J.; Abellan, G.; Hauke, F.; Hirsch, A.; Sanvito, S.; O'Regan, D. D.; Duesberg, G. S.; Nicolosi, V.; Coleman, J. N. *Nat. Commun.* **2015,** *6,* 8563. doi:10.1038/ncomms9563

11. Harvey, A.; Boland, J. B.; Godwin, I.; Kelly, A. G.; Szydłowska, B. M.; Murtaza, G.; Thomas, A.; Lewis, D. J.; O'Brien, P.; Coleman, J. N. *2D Mater.* **2017,** *4,* 025054. doi:10.1088/2053-1583/aa641a

12. Alencar, A. B.; Barboza, A. P. M.; Archanjo, B. S.; Chacham, H.; Neves, B. R. A. *2D Mater.* **2015,** *2,* 015004. doi:10.1088/2053-1583/2/1/015004

13. Świetlicki, M.; Chocyk, D.; Klepka, T.; Prószyński, A.; Kwaśniewska, A.; Borc, J.; Gładyszewski, G. *Materials* **2020,** *13,* 698. doi:10.3390/ma13030698

14. Torres, H. S. S.; Varajão, A. F. D. C.; Sabioni, A. C. S. *Appl. Clay Sci.* **2015,** *112-113,* 53–61. doi:10.1016/j.clay.2015.04.016

15. Castillo, L.; López, O.; López, C.; Zaritzky, N.; García, M. A.; Barbosa, S.; Villar, M. *Carbohydr. Polym.* **2013,** *95,* 664–674. doi:10.1016/j.carbpol.2013.03.026

16. Balamurugan, G. P.; Maiti, S. N. *Polym. Eng. Sci.* **2010,** *50,* 1978–1993. doi:10.1002/pen.21724

17. Claverie, M.; Dumas, A.; Carême, C.; Poirier, M.; Le Roux, C.; Micoud, P.; Martin, F.; Aymonier, C. *Chem. – Eur. J.* **2018,** *24,* 519–542. doi:10.1002/chem.201702763

18. Mania, E.; Alencar, A. B.; Cadore, A. R.; Carvalho, B. R.; Watanabe, K.; Taniguchi, T.; Neves, B. R. A.; Chacham, H.; Campos, L. C. *2D Mater.* **2017,** *4,* 031008. doi:10.1088/2053-1583/aa76f4

19. Lund, S.; Kauppila, J.; Sirkiä, S.; Palosaari, J.; Eklund, O.; Latonen, R.-M.; Smått, J.-H.; Peltonen, J.; Lindfors, T. *Carbon* **2021,** *174,* 123–131. doi:10.1016/j.carbon.2020.11.094

20. Karger, L.; Synnatschke, K.; Settele, S.; Hofstetter, Y. J.; Nowack, T.; Zaumseil, J.; Vaynzof, Y.; Backes, C. *Adv. Mater. (Weinheim, Ger.)* **2021,** *33,* 2102883. doi:10.1002/adma.202102883

21. Abreu, B.; Almeida, B.; Ferreira, P.; Fernandes, R. M. F.; Fernandes, D. M.; Marques, E. F. *J. Colloid Interface Sci.* **2022,** *626,* 167–177. doi:10.1016/j.jcis.2022.06.097

22. Sugioka, H.; Moroi, Y. *Biochim. Biophys. Acta, Lipids Lipid Metab.* **1998,** *1394,* 99–110. doi:10.1016/s0005-2760(98)00090-3

23. Perdikatsis, B.; Burzlaff, H. *Z. Kristallogr.* **1981,** *156,* 177–186. doi:10.1524/zkri.1981.156.3-4.177

24. Fernandes, T. F. D.; Miquita, D. R.; Soares, E. M.; Santos, A. P.; Cançado, L. G.; Neves, B. R. A. *2D Mater.* **2020,** *7,* 025045. doi:10.1088/2053-1583/ab7975

25. Santos, J. C. C.; Prado, M. C.; Morais, H. L. O.; Sousa, S. M.; Silva-Pinto, E.; Cançado, L. G.; Neves, B. R. A. *npj 2D Mater. Appl.* **2021,** *5,* 51. doi:10.1038/s41699-021-00234-z

26. Backes, C.; Szydłowska, B. M.; Harvey, A.; Yuan, S.; Vega-Mayoral, V.; Davies, B. R.; Zhao, P.-l.; Hanlon, D.; Santos, E. J. G.; Katsnelson, M. I.; Blau, W. J.; Gadermaier, C.; Coleman, J. N. *ACS Nano* **2016,** *10,* 1589–1601. doi:10.1021/acsnano.5b07228

27. Merkus, H. G. *Particle Size Measurements;* Particle Technology Series; Springer: Dordrecht, 2009. doi:10.1007/978-1-4020-9016-5

28. Chacham, H.; Santos, J. C. C.; Pacheco, F. G.; Silva, D. L.; Martins, R. M.; Del'Boccio, J. P.; Soares, E. M.; Altoé, R.; Furtado, C. A.; Plentz, F.; Neves, B. R. A.; Cançado, L. G. *ACS Appl. Nano Mater.* **2020,** *3,* 12095–12105. doi:10.1021/acsanm.0c02598

29. Foley, J. P.; Dorsey, J. G. *J. Chromatogr. Sci.* **1984,** *22,* 40–46. doi:10.1093/chromsci/22.1.40

30. Necas, D.; Klapetek, P. *Cent. Eur. J. Phys.* **2012,** *10,* 181–188. doi:10.2478/s11534-011-0096-2

On the use of Raman spectroscopy to characterize mass-produced graphene nanoplatelets

Keith R. Paton[*1], Konstantinos Despotelis[1], Naresh Kumar[1,2], Piers Turner[1,3] and Andrew J. Pollard[*1]

Full Research Paper

Address:
[1]National Physical Laboratory, Teddington, TW11 0LW, UK,
[2]Department of Chemistry and Applied Biosciences, ETH Zurich, CH-8093 Zurich, Switzerland and [3]Department of Physics, University of Oxford, Oxford, UK

Email:
Keith R. Paton[*] - keith.paton@npl.co.uk; Andrew J. Pollard[*] - andrew.pollard@npl.co.uk

* Corresponding author

Abstract

Raman spectroscopy is one of the most common methods to characterize graphene-related 2D materials, providing information on a wide range of physical and chemical properties. Because of typical sample inhomogeneity, Raman spectra are acquired from several locations across a sample, and analysis is carried out on the averaged spectrum from all locations. This is then used to characterize the "quality" of the graphene produced, in particular the level of exfoliation for top-down manufactured materials. However, these have generally been developed using samples prepared with careful separation of unexfoliated materials. In this work we assess these metrics when applied to non-ideal samples, where unexfoliated graphite has been deliberately added to the exfoliated material. We demonstrate that previously published metrics, when applied to averaged spectra, do not allow the presence of this unexfoliated material to be reliably detected. Furthermore, when a sufficiently large number of spectra are acquired, it is found that by processing and classifying individual spectra, rather than the averaged spectrum, it is possible to identify the presence of this material in the sample, although quantification of the amount remains approximate. We therefore recommend this approach as a robust methodology for reliable characterization of mass-produced graphene-related 2D materials using confocal Raman spectroscopy.

Introduction

Graphene and related 2D materials (GR2Ms) are now well established with commercial products available across a range of sectors, from sports and leisure products [1,2], through mobile phones [3] to automotive applications [4]. There are also a large number of producers of these materials [5], offering an array of products with a wide range of properties such as im-

proved mechanical strength and higher thermal conductivity. To accelerate the further development and adoption of GR2Ms, it is critical to develop reliable and standardized methods to characterize the materials being produced and purchased. The publication of international standards is a key step in this process, such as recent publications on nomenclature [6] and structural characterization [7]. The measurement methods described in these standards, however, can be time-consuming and expensive. As the range of applications for GR2Ms expands, and with it the production volumes, there is an increasing need for faster methods that can be applied in-line or at-line. These quality control methods do not need the same level of accuracy and precision as those specified in international standards, but they do need to be validated against those methods. What is more important is repeatability and reproducibility, to allow for product monitoring over time. They also need to be able to provide results quickly, in a form that is easy to interpret, providing simple pass/fail outcomes.

Raman spectroscopy is one of the most widely used characterization tool for GR2Ms [8]. A search of Web of Science showed that of 97,532 articles published in the last five years with "Graphene" in the abstract, 9.3% also mentioned "Raman". This is compared with atomic force microscopy (AFM) (2.4%), scanning electron microscopy (SEM) (11.4%), transmission electron microscopy (TEM) (7.2%) or X-ray photoelectron spectroscopy (XPS) (5.6%). It has the advantages of relatively low cost, simple sample preparation, quick measurements, and automated analysis, offering clear benefits for quality control applications. It has been demonstrated in several application areas as an in-line process analysis and control method [9-12].

Raman spectroscopy is particularly suited to the analysis of graphitic materials because of the large scattering cross section of graphitic materials and the large amount of information obtainable from a single measurement. For example, information on flake size, extent of structural defects, chemical or electronic doping, and strain and layer number can all be extracted from one spectrum [13-18]. As such, Raman spectroscopy is widely used by producers to assess the quality of their material, in particular the absence of graphite or nanoscale graphite. It is important to recall that graphene has been defined as a "single layer of carbon atoms with each atom bound to three neighbours in a honeycomb structure" with materials with more than one layer defined as "few-layer graphene" or "graphene nanoplatelets" [6]. This assessment is generally based on examining the shape of the so-called 2D peak (ca. 2700 cm^{-1}), which, for Bernal stacking, shows clear changes on going from single-layer through few-layer graphene to graphite [19]. Bulk graphite typically shows a signal comprising two components, sometimes referred to as $2D_1$ and $2D_2$, with intensities approxi-

mately one fourth and half of that of the so-called G peak (ca. 1580 cm^{-1}) [20]. In contrast, single-layer graphene typically yields a 2D peak comprising a single component, with an intensity of around double that of the G peak [19]. In between these two extremes, the peak shape evolves gradually, and while the 2D peak from bilayer graphene has been shown to comprise four components, deconvolution for higher layer numbers has not been reliably carried out. The spectrum recorded from flakes with ten or more layers is typically indistinguishable from that of bulk graphite. However, it is important to note that this behaviour can be affected by the stacking order. For example, for turbostratic graphite, where there is random rotational alignment between the layers, the 2D band also has the shape of a single Lorentzian line [21]. However, it typically has a larger width (45–60 cm^{-1}) compared to single layer graphene (ca. 24 cm^{-1}). The intensity of the peaks has also been shown to be influenced by the rotational angle in bilayer graphene, although the shape of the peak is largely unaffected [22]. Roscher et al. [23] have attempted to quantify the distinction between graphite and few-layer graphene based on the "goodness of fit" parameter when using a single Voigt function to fit the 2D peak. However, these changes in peak shape and (relative) intensity are generally only qualitative and have mostly been demonstrated only on well-defined materials, either from large mechanically exfoliated flakes or CVD-grown materials. When measuring the Raman spectrum from aggregated few-layer graphene (FLG) powder, where many particles are probed in a single measurement, the Raman 2D peak still typically appears as a symmetric shape, although with lower (relative) intensity and larger width than for single-layer graphene as a result of the convolution of many individual peaks [13].

It has previously been shown that Raman spectroscopy can be used to provide quantitative information on both flake thickness and lateral size of exfoliated graphene nanoplatelets (GNPs) [13]. These metrics are based on averaging spectra from multiple locations and using this averaged spectrum to make claims about the quality of the material. However, it is not clear how sensitive these metrics are to small amounts of thicker materials in a sample. Typically, the samples used to derive these metrics had also been carefully processed to ensure removal of unexfoliated graphite particles. In other cases, metrics are developed based on changes in Raman spectra with layer number from measurements on individual, well-defined, flakes that are not commercially produced [23]. Again, it is not clear if the same metrics can be applied to measurements performed on bulk material, where flakes are restacked or reaggregated. As many GNP products are produced through top-down manufacturing methods, which typically have a GNP yield of less than 100%, there is often a separation step in the production process [24,25]. Often based on a sedimentation process, this step

removes the unexfoliated fraction of the material from the exfoliated product. However, if this process is not well designed and controlled, it is possible for the unwanted sediment to pass into the product stream. Due to this potential variation in material form within a sample, the results of any Raman analysis are typically based on averaging the spectra from a number of measurements across a sample. Although the sediment material has a distinct Raman spectrum compared to the commercially supplied GNP powder, it is not clear if Raman spectroscopy has the sensitivity to detect the presence of this material in the final product.

In this paper, we examine the effect that increasing amounts of unexfoliated graphitic material in a well-defined sample of GNPs have on the measured Raman spectra. First, a sample of GNP material is prepared through careful separation of unexfoliated material. Then, the observed changes for an averaged Raman spectrum are investigated while adding small amounts of graphite to the GNP sample. We then evaluate the ability of previously published metrics to identify the presence of this unexfoliated material in the GNP sample. Finally, we examine a more industrially relevant set of samples where fractions of the sediment removed during a separation stage are added back into the GNP sample. By examining the Raman spectrum averaged across many points on the sample, as well as individual spectra, the limits of the published metrics can be tested, and recommendations can be made for improved Raman analysis approaches.

Methods

Rather than using commercial GNP products, we produced a dispersion by sonication-assisted liquid-phase exfoliation, using graphite (Sigma-Aldrich, UK, product no. 332461) and 1-methyl-2-pyrrolidone (NMP) (Sigma-Aldrich, UK, ACS Reagent, product number 443778) [26] as starting materials. An initial processing of the graphite was carried out to remove any impurities or small graphitic particles present in the material. To achieve this, graphite (0.8 g) was added to NMP (40 mL), and the mixture was sonicated at 20 kHz with a flat-head probe (130 W, CPX 130, Cole-Parmer Instruments, USA; 60% amplitude, 6 s on/2 s off cycle, 1 h sonication). The vessel was kept cool by immersing it in an ice bath during processing. The dispersion was then centrifuged at 5000g for 1 h, and the supernatant was separated from the sediment and discarded. Fresh NMP was added to bring the volume up to 40 mL, and the mixture was returned to the sonic tip. Using the same conditions as for the initial processing step, the mixture was sonicated for 5 h to exfoliate the graphite.

To ensure that thicker material was removed from the dispersion, an abbreviated cascade centrifugation process was applied

[27]. The dispersion obtained following 5 h of sonication was centrifuged at low speed (250g) for 2 h to remove the very largest particles of unexfoliated graphite. The supernatant from this step was then centrifuged at 1000g for 2 h to sediment the larger particles of GNPs. The supernatant from this step was then further centrifuged at 5000g for 2 h to sediment the thinner GNPs. This sediment was then mixed with fresh NMP (50 mL), and the mixture was vortex-mixed briefly and subsequently sonicated in a bath sonicator for 5 min to re-disperse the sediment. This sample is referred to as "GNP$_{ref}$".

The concentration of GNP$_{ref}$ was measured using UV–vis extinction spectroscopy (Perkin-Elmer 850, PerkinElmer, UK), using a cuvette with 10 mm path length. Measuring the extinction at 660 nm and using an extinction coefficient of 4237 mL·mg^{-1}·m^{-1} [28] yielded a concentration of 0.028 mg·mL^{-1}.

To characterize the thickness of the particles in GNP$_{ref}$, the dispersion was drop-cast on to a cleaned Si/SiO$_2$ (300 nm thick oxide layer) wafer. Before deposition, the dispersion was diluted by a factor of 10 in fresh NMP. 10 µL of the diluted dispersion was then drop-cast on a Si/SiO$_2$ wafer at a temperature of 200 °C. To remove residual NMP, the sample was dried overnight in a vacuum oven at 60 °C.

AFM measurements of the deposited flakes were carried out using Cypher AFM (Asylum Research, Oxford Instruments, UK). AFM images were recorded using Si AFM probes (Mikro-Masch HQ:NSC15, 40 N/m, 325 kHz, MikroMasch, Bulgaria) in tapping-mode feedback. AFM images were measured in square areas between 6 µm × 6 µm and 8 µm × 8 µm using 1024 × 1024 pixels with a scan speed below 20 µm·s^{-1}.

To prepare the mixed GNP$_{ref}$/graphite samples, 1.2 mg of the as-purchased graphite was mixed with 40 mL of NMP, and the mixture bath was sonicated for 30 min. Sonication was carried out to reduce the particle size while still maintaining the thickness to be graphite-like [29]. The graphite and GNP$_{ref}$ dispersions were then mixed to obtain graphite mass fractions as given in Table 1.

To prepare the mixed GNP$_{ref}$/sediment samples, a fresh GNP$_{ref}$ sample was prepared by sonication as described above. After the initial centrifugation step at 250g, however, the sediment was retained and redispersed in fresh NMP. The concentration of the resulting dispersion was measured using UV–vis spectroscopy, as described above. The dispersion was then added to the GNP$_{ref}$ sample to produce 13 mixed GNP/sediment samples with sediment concentrations of 0.5, 1, 2, 5, 10, 25, 35, 50, 65, 75, and 90 wt %.

Table 1: Graphite content in the samples measured in this study.

Sample #	GNP$_{ref}$/wt %	Graphite/wt %
1	0	100
2	90	10
3	95	5
4	98	2
5	99	1
6	99.5	0.5
7	100	0

Each mixed dispersion was then vacuum-filtered through alumina membranes (20 nm pore size), rinsed with IPA to remove residual NMP, and dried in a vacuum oven at 60 °C overnight. For samples 2 to 7, 3 mL of the dispersion was filtered, while for sample 1, ca. 30 mL was used to ensure adequate coverage of the membrane.

Raman spectra of the filtered films on the membrane were recorded using a Renishaw Qontor confocal spectrometer (Renishaw plc., UK) using a 532 nm excitation laser and a 2400 L/mm grating. An area of 20 μm × 20 μm of the film was mapped, with 1 μm distance between measurement locations. Spectra were recorded between 1000 cm^{-1} and 3000 cm^{-1} Raman shift, using 5% of the maximum power (ca. 0.8 mW incident on the sample), 10 s acquisition time, and a 100× (0.9 NA) objective lens.
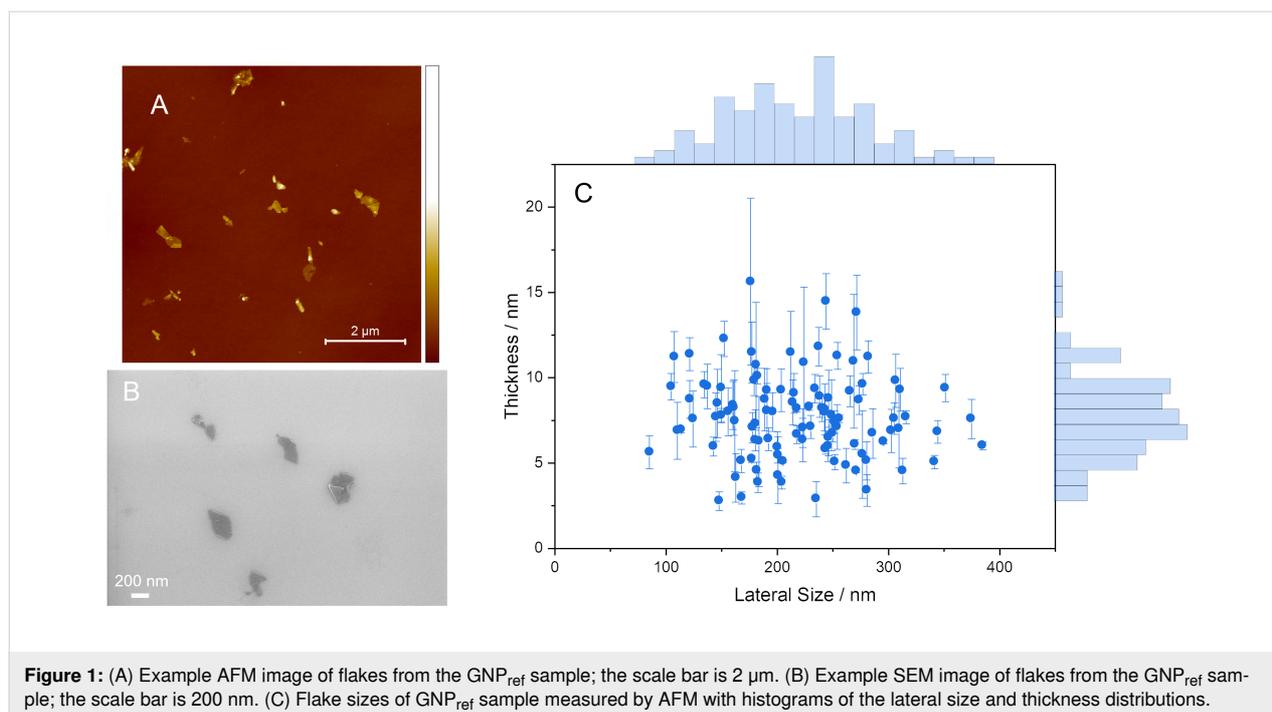
Spectra were processed to remove cosmic ray artefacts, and a baseline was subtracted using the "Intelligent Fitting" algorithm in the Wire 5.4 software (Renishaw plc., UK) based on an 11-point polynomial. Each spectrum was then normalised to give intensities between 0 and 1, and the spectra from each map were averaged. D band, G band, D' band, and 2D band of all spectra, either individual or averaged, were fitted using Lorenztian functions. The peaks were fitted together, with an offset baseline. We have averaged across 441 points in a sample, which is more than is used in a typical workflow, and the effect of the number of points measured is examined later in this paper.

Results and Discussion
AFM results
The aim of the sample preparation protocol for GNP$_{ref}$ is to obtain a dispersion that contains primarily graphene nanoplatelets [6] without unexfoliated graphite particles. To evaluate this [30-32], AFM was carried out to measure the thickness of the flakes from the dispersion. A representative AFM image of the flakes contained in the GNP dispersion is presented in Figure 1. The measurements were carried out according to ISO TS 21356-1 [7].

The height of the flakes ranged from 2.8 to 15.6 nm, with 85.3% of the measured flakes thinner than 10 nm and 3.9% of the flakes less than 3.4 nm thick. These are particles that can be classified as FLG in thickness [6]. We note that this is a higher content of FLG than in many such powders on the market [33].

Figure 1: (A) Example AFM image of flakes from the GNP$_{ref}$ sample; the scale bar is 2 μm. (B) Example SEM image of flakes from the GNP$_{ref}$ sample; the scale bar is 200 nm. (C) Flake sizes of GNP$_{ref}$ sample measured by AFM with histograms of the lateral size and thickness distributions.

The flakes had a mean height of 7.7 ± 2.5 nm (mean ± standard deviation) and a median height of 7.6 nm. A scatter plot showing the correlation between the flake height (i.e., thickness) and their lateral size is shown in Figure 1c. Figure 1c indicates that the height of the flakes in the GNP dispersion is independent of the lateral size. The lateral size of the measured flakes ranged from 85 nm to 385 nm, with a mean lateral size of 219 ± 64 nm and a median lateral size of 218 nm. We did not attempt to give a number of layers for these flakes. Yet, we do note that while the natural interlayer spacing for graphite is 0.34 nm, it has been reported previously that for similarly produced flakes, monolayer flakes had a measured thickness of 2 nm, with each additional monolayer adding 0.95 nm to the thickness [25].

Graphite addition
Raman spectroscopy results
Samples of GNP_{ref} with different amounts of added graphite were analysed with Raman spectroscopy. As shown in Figure 2, the spectrum measured from pure graphite is distinct from that of the GNP_{ref} with a lower D band intensity (ca. 1350 cm^{-1}) and a distinct shoulder on the 2D band at ca. 2700 cm^{-1}. In contrast, there is no clear difference in the average spectra recorded in any of samples 2–7. All of them are almost identical to the spectrum of the GNP_{ref} sample. In other words, despite the samples contained up to 10 wt % graphite, a measurement protocol that might be considered typical yields a spectrum that is almost indistinguishable from that of graphene nanoplatelets.

The averaged spectra were fitted to obtain the peak intensity ratios, as shown in Figure 3. To investigate any differences in the measured spectra, each spectrum in each map was also fitted to obtain the peak intensities of the D peak (1350 cm^{-1}), the G peak (1580 cm^{-1}), the D' peak (1620 cm^{-1}), and the 2D peak (2700 cm^{-1}) (see Supporting Information File 1, Figure S1 for distributions of I_D/I_G values). The median of the values was then calculated, together with the standard error of the mean. Note that the 2D peak has not been fitted for the graphite sample as the 2D peak in the graphite spectrum is a poor fit to a single Lorentzian function. For all other spectra, a single peak was used to fit the 2D band. The intensity ratio between D peak and G peak (I_D/I_G) has been shown to correlate with the lateral sizes of exfoliated flakes [30-32], while the intensity ratio between 2D peak and G peak (I_{2D}/I_G) varies with flake thickness [8,19,34]. As shown in Figure 3, in both cases (averaged (black) and individual (red)), there is a fall in the value of I_D/I_G with increasing graphite content. This would be expected as the graphite particles have a larger lateral size compared to the exfoliated GNPs. However, this trend is only seen up to 2 wt % graphite, with no further change observed above this graphite weight percentage value. The overall variation in I_D/I_G ratio between samples is also relatively small. This trend is matched by the I_{2D}/I_G ratio, which again would be expected due to the thicker particles in the graphite materials. See Supporting Information File 1, Figure S2 for plots including the 100 wt % graphite sample.

While metrics such as mean intensity ratios are widely used, a more reliable identifier to distinguish graphite from graphene/few-layer graphene is the shape of the 2D peak. For graphite, it shows a clear shoulder on the low-wavenumber side of the peak, as seen in Figure 2b, and is therefore best fitted with two individual Lorentzian peaks. In order to investigate whether Raman spectroscopy can be used to quantify the proportion of graphite in a bulk sample such as this, a non-negative linear least-squares (NNLS) algorithm [35] has been applied to the
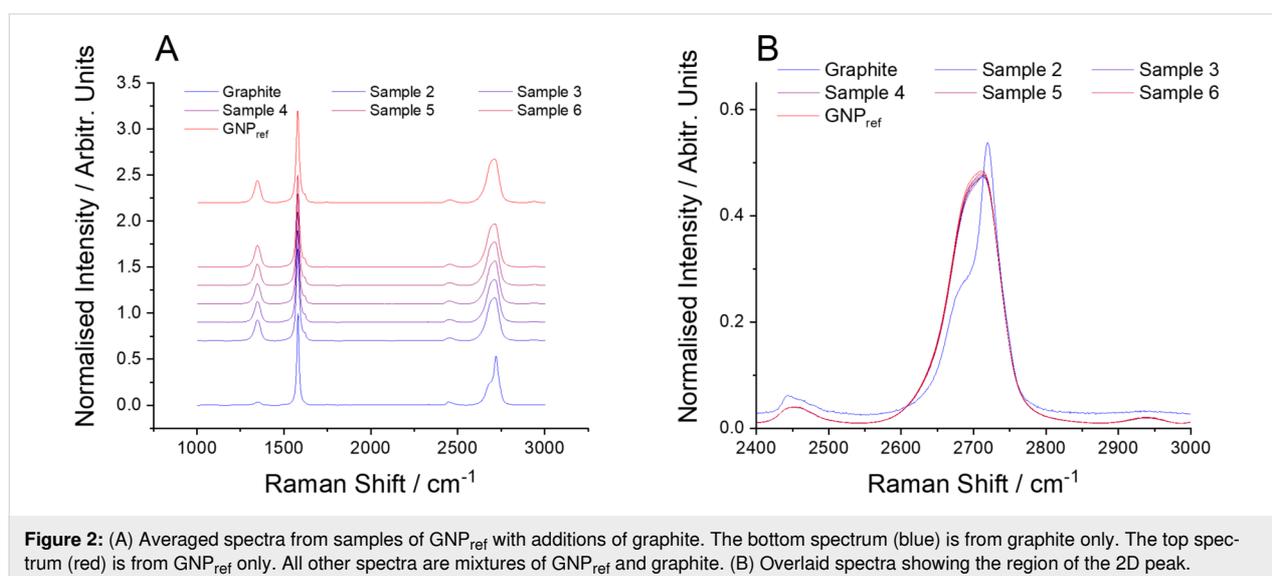
Figure 2: (A) Averaged spectra from samples of GNP_{ref} with additions of graphite. The bottom spectrum (blue) is from graphite only. The top spectrum (red) is from GNP_{ref} only. All other spectra are mixtures of GNP_{ref} and graphite. (B) Overlaid spectra showing the region of the 2D peak.
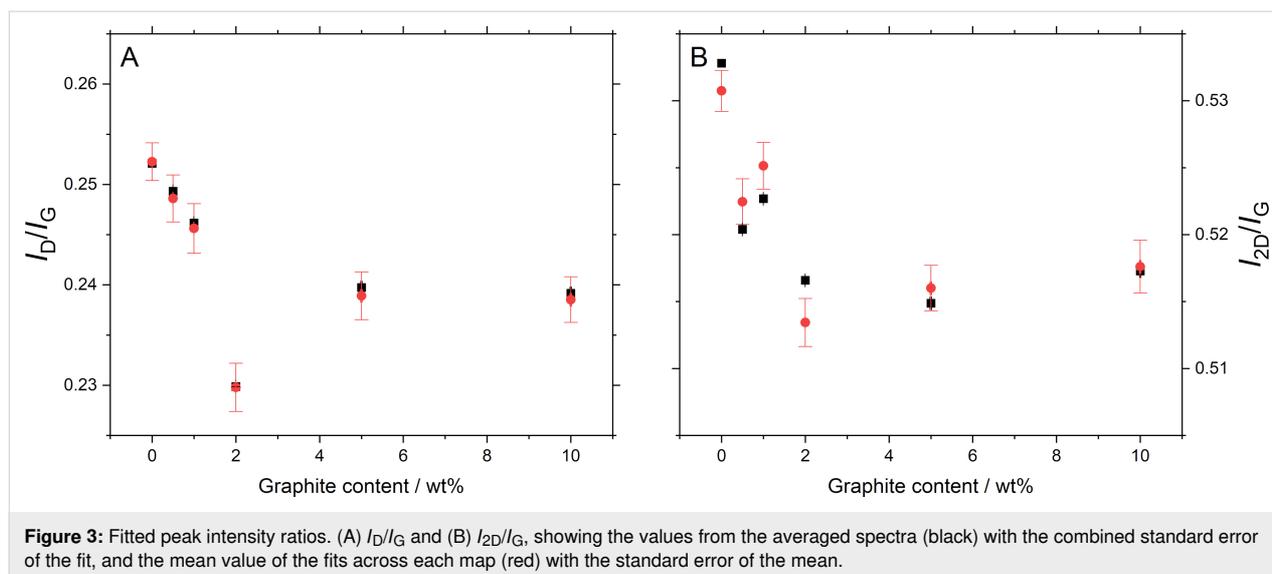
Figure 3: Fitted peak intensity ratios. (A) I_D/I_G and (B) I_{2D}/I_G, showing the values from the averaged spectra (black) with the combined standard error of the fit, and the mean value of the fits across each map (red) with the standard error of the mean.

spectra to calculate the quality of the match to either a graphite or GNP Raman spectrum. This fitting was carried out using the "Component Analysis" tool in Wire 5.4, using the average spectra from graphite and GNP samples respectively as the "pure" components. No additional baseline or normalization was applied during the analysis, and the spectra were fitted directly (rather than a derivative of the spectra). Similar fitting can be implemented in a range of other analysis packages. A higher value of the correlation value indicates a better match to that component. Plotting the median value of the graphite correlation value (Figure 4, black data points) shows that it increases with increasing graphite content across the full range of measured graphite loading. This approach appears therefore capable of discerning the amount of graphite in a sample.

From the distribution of component loadings from the GNP$_{ref}$ sample (see Supporting Information File 1, Figure S2) we can define a threshold value for a spectrum that corresponds to graphite. This is taken as the d_{90} value from the distribution. Based on this, we can then classify each pixel measured across a sample as either "graphite" or "GNP". From this, we can calculate a fraction of graphite in the sample, as shown in Figure 4 (red data points). The measured fraction of graphite-like spectra increases with nominal graphite content in the sample. The fraction for the graphite sample is close to 100% confirming that the sample has very high levels of thick, graphite-like flakes (see Supporting Information File 1, Figure S3 for plots of other metrics shown to include the 100% graphite sample).

The analysis based on simple peak fitting of the spectra measured from samples with graphite added to GNP$_{ref}$ have shown that there is very limited ability to reliably identify the presence of graphite. In contrast, applying a least-squares fitting process to estimate the graphite loading in each sample shows better ability to identify those additions. However, it is of interest to examine how previously published metrics perform on the same samples.

Comparison to literature metrics

As mentioned above, several metrics have previously been published to attempt to obtain quantitative information of the flake thickness from Raman measurements. A selection of these have been applied to the data acquired as part of this work to evaluate whether these metrics can be implemented successfully. Two metrics have been presented by Backes et al. [13] to quantify the mean number of layers from Raman spectra measurements. The first of these (M$_1$) is based on the I_{2D}/I_G ratio as calculated above, and an empirical fit to the mean number of layers N was found as

$$\langle N \rangle = 1.04 * \left(I_{2D}/I_G \right)^{-2.32}. \tag{1}$$

The second metric (M$_2$) is based on the ratio of intensities at two different locations in the 2D band [13]. The first location is that of the maximum of the 2D band of the parent graphite material. In this case, this is the 100% graphite sample and the location is $\omega_1 = 2719$ cm^{-1}. The second location is 30 cm^{-1} below the first location, that is, $\omega_2 = 2689$ cm^{-1}. The ratio of the intensities at these two locations is then normalised to the ratio from the parent graphite, such that

$$M_2 = \left(\frac{I_{\omega_1}}{I_{\omega_2}} \right)_{GNP} \Big/ \left(\frac{I_{\omega_1}}{I_{\omega_2}} \right)_{G'ite}. \tag{2}$$
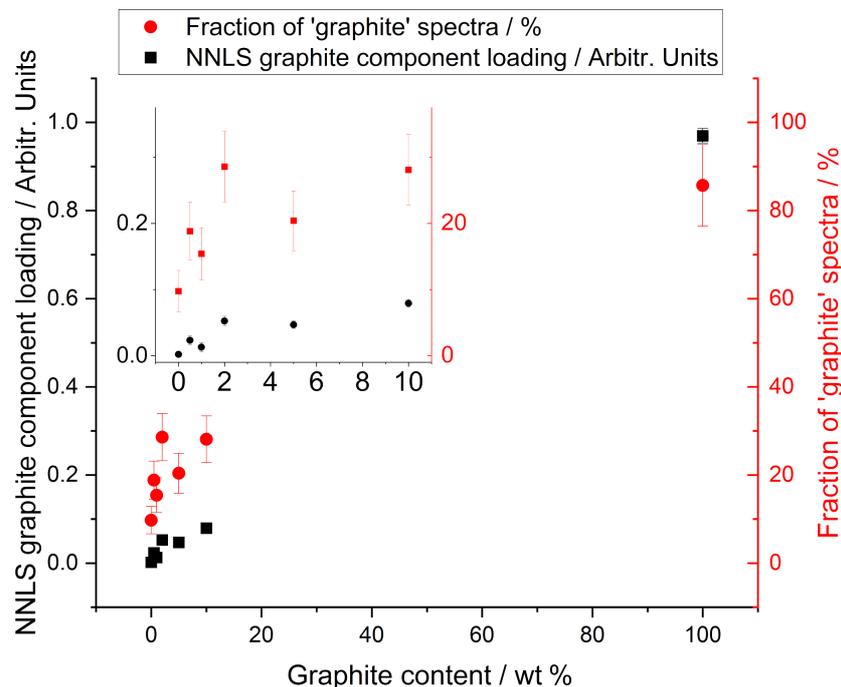
Figure 4: Median value of the graphite component loading value, as determined by a non-negative least-squares fit (black squares, left axis) and the fraction of points that show a graphite-like spectrum (red squares, right axis). A graphite-like spectrum is defined as having a correlation value to the graphite spectrum of greater than 0.15, as obtained from a non-negative linear least-squares procedure when fitted with both a GNP and graphite spectrum. The inset shows the low-loading region of the graph, with the same axes.

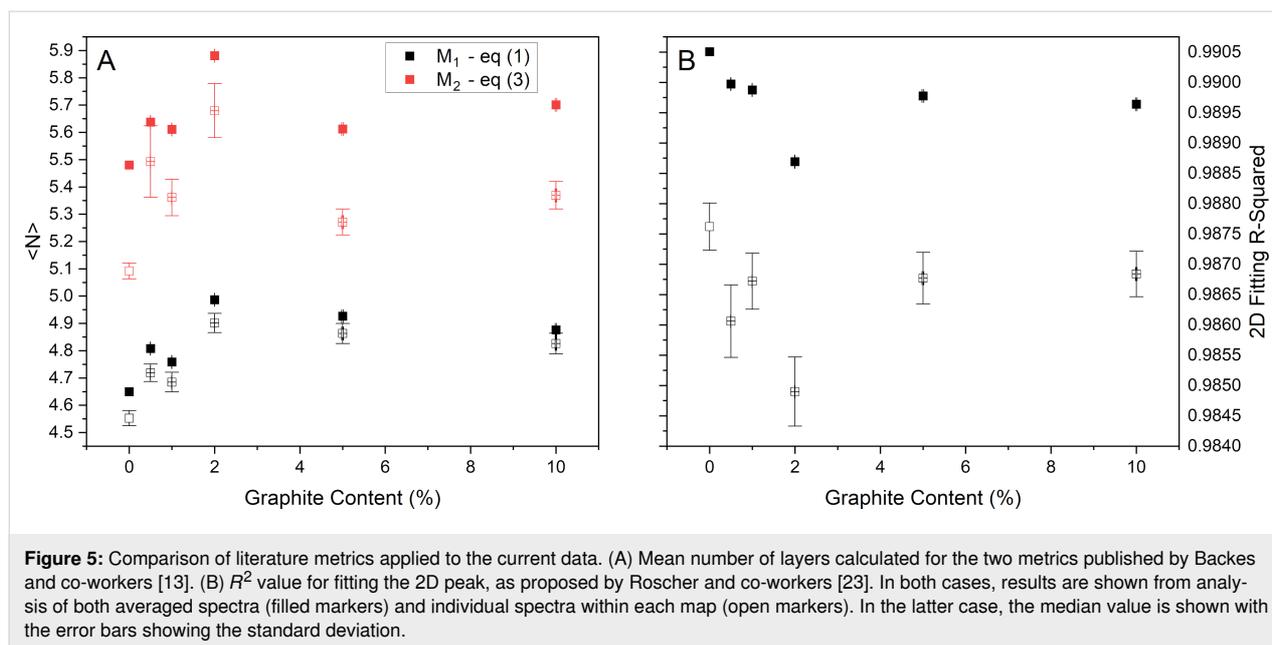The mean number of layers per flake can then be calculated according to

$$\langle N \rangle = 0.83 e^{3.6 M_2}. \tag{3}$$

An alternative approach has been proposed, based on the change in shape of the 2D band as the number of layers increases [23,36-38]. It is known that Raman measurements of single-layer graphene produces a single peak, whereas graphite produces a bimodal peak [19]. Furthermore, it has also been shown that the peak shape changes gradually between these two extreme cases [34]. As a simple way to characterize this change, the 2D peak can be fitted to a single Voigt peak, and the quality of the fit, as quantified by the R^2 value, can be correlated to the mean number of layers in the sample. Results from the Casiraghi group [39] suggest that a single-layer flake has $R^2 > 0.987$ and few-layer graphene has $0.987 > R^2 > 0.985$. R^2 values less than 0.985 would indicate a thicker flake with more than seven layers.

We have applied the three metrics described above to the current data, both the averaged spectra and each individual spectrum, with the results shown in Figure 5. It is clear that, neither

of the simple peak intensity ratios described above are effective at discriminating the presence of graphite within the sample. Some changes are seen up to 2 wt % graphite, but not beyond this (see Supporting Information File 1, Figure S3 for plots including the 100 wt % graphite sample). We also note that the number of layers for the GNP$_{ref}$ sample predicted by the M$_1$ and M$_2$ metrics are in reasonable agreement with the AFM results presented in Figure 1.

The metric based on the 2D peak shape was derived from measurements on single flakes with well-characterized thicknesses. It is known that when measuring bulk, reaggregated flakes, the 2D peak retains a symmetric shape, even to values of mean thickness where a single flake of equivalent thickness would yield a clear shoulder in the Raman spectrum [13]. It is clear from these measurements that this method also does not have the sensitivity to identify the presence of small amounts of graphite in a sample. Similarly, although the metrics from Backes et al. were both derived from measurements of reaggregated materials, they are also unable to identify the graphite content. The samples used to develop these methods, however, were carefully prepared to exclude all graphite-like material, which may not be representative of commercially produced products. It is of particular note that the M$_2$ and R^2 metrics give

Figure 5: Comparison of literature metrics applied to the current data. (A) Mean number of layers calculated for the two metrics published by Backes and co-workers [13]. (B) R^2 value for fitting the 2D peak, as proposed by Roscher and co-workers [23]. In both cases, results are shown from analysis of both averaged spectra (filled markers) and individual spectra within each map (open markers). In the latter case, the median value is shown with the error bars showing the standard deviation.

significantly different values of mean layer number depending on whether the single averaged spectrum or the individual spectra are analysed. It is clear that the sequence of analysis (analysing an averaged spectrum vs averaging values from individual spectra) can have an effect on the results obtained for these methods. In the case of the R^2-based metric, this difference is likely to be a result of the reduction in noise level affecting the value of R^2 (see Supporting Information File 1). Additional metrics, including G peak width and the correlation between peak area ratios and G peak width, show similar trends (see Supporting Information File 1).
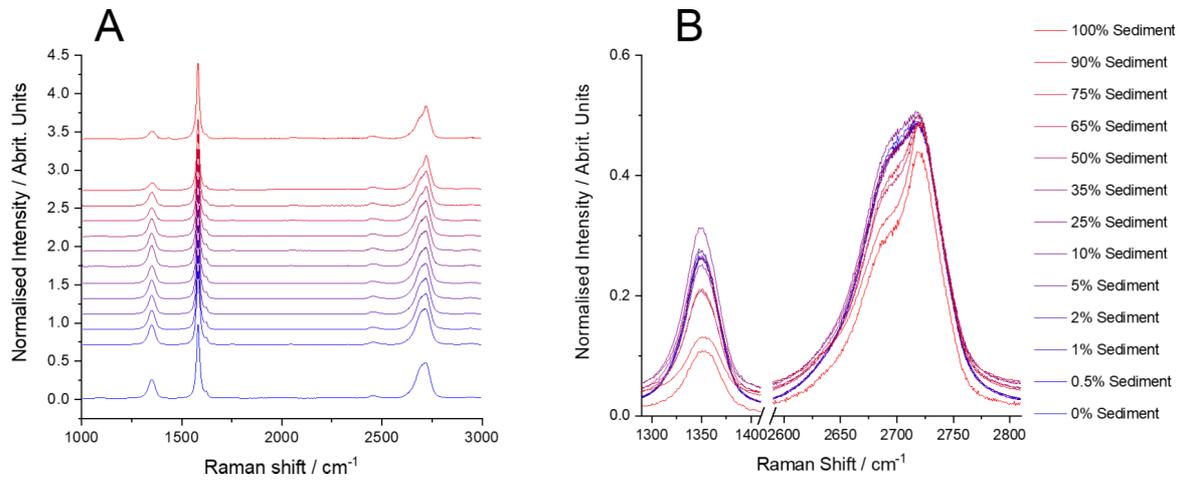
Sediment additions

While the results presented above demonstrate the limitations of Raman spectroscopy to identify the presence of graphite in a GNP sample, of more relevance is the question of identifying unexfoliated sediment. In typical top-down exfoliation processes, the yield of few-layer graphene or graphene nanoplatelets is very small, often less than 1 wt %. Hence, there is a need to separate this product from the processed but unexfoliated material (which can often be recycled through the process again). Often this is accomplished through a centrifuge-based method, hence this material is referred to as sediment here. In order to maximise production yield, there is a need to maximise the amount of GNP material extracted, while to maintain product quality, it is important to prevent sediment accidentally ending up in the extracted GNP fraction. To allow for a commercially viable, industrial scale-up, it is important to understand the performance of this separation step in order to minimise processing time and to maximise separation efficiency.

To investigate if Raman spectroscopy can be used for this purpose, a fresh sample of GNP_{ref} was prepared as described above, using the same processing conditions. Instead of fresh graphite however, the sediment from the first, low-speed centrifugation step (at 250g) was recovered, and re-mixed into the GNP_{ref} sample. These mixed samples were then filtered and measured with Raman spectroscopy using the same settings described above. The spectra measured by averaging across the mapped area are shown in Figure 6, where it can be seen that up to ca. 50 wt % sediment, there is little change between them. This is despite the fact that the sediment spectrum is clearly different and closely matches what would be expected from graphite.

This result confirms that simple inspection of a Raman spectrum, even when averaged across a large number of locations in a sample, cannot be relied on to confirm the absence of unexfoliated graphite material. Fitting these averaged spectra confirms that the simple intensity ratios (Figure 7a,b) do not show any significant differences up to between 35 wt % and 50 wt % sediment added. This is also true of the metric M_2 (Figure 7c) and the R^2 value (Figure 7d) from fitting the 2D peak to a single Voigt function.

The results in Figure 7 suggest that using a simple metric based on peak or spectral intensities is not useful to identify the presence of up to 20 wt % unexfoliated sediment in a sample of GNPs. This is the case both when analysing an averaged spectrum or when averaging the values obtained from individual spectra across the map. Of the possible metrics examined here, the method based on the R^2 value from fitting the 2D peak

Figure 6: (A) Averaged spectra from samples of GNP$_{ref}$ with additions of sediment. Bottom spectrum (blue) is sediment only. Top spectrum (red) is GNP$_{ref}$ only. All other spectra are mixtures of GNP$_{ref}$ and sediment. (B) Overlaid spectra showing the region of the D peak and the 2D peak.
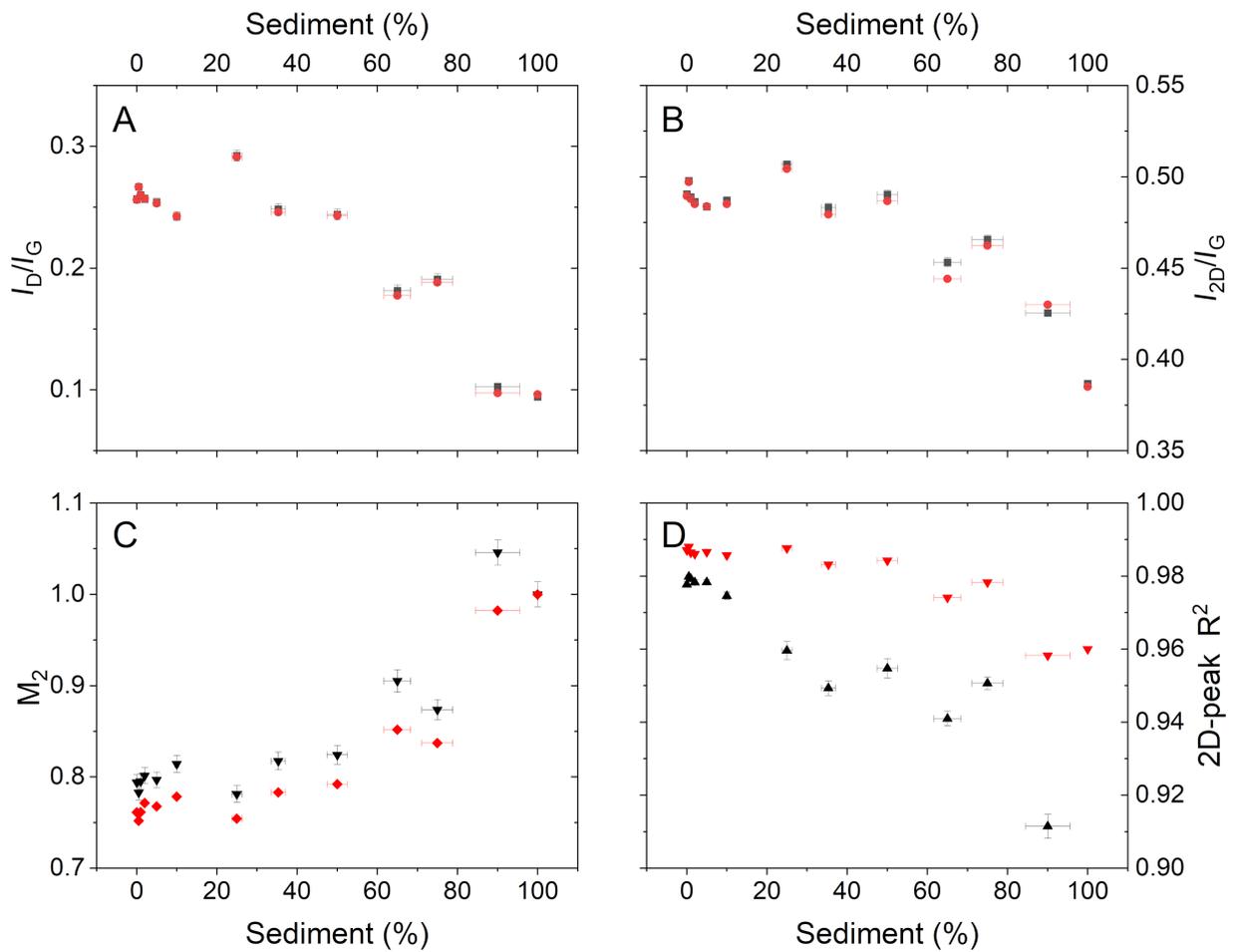
Figure 7: Values of the metrics at each sediment loading. (A) I_D/I_G intensity ratio; (B) I_{2D}/I_G intensity ratio; (C) M$_2$ metric from Backes et al. [13]; (D) R^2 value from fitting the 2D peak to a single Voigt function. Results are shown from both the average spectra (red) and the mean value from the fitting of each spectrum in a map (black) showing the standard deviation as the error bar.

shows the widest range of use when many individual Raman spectra are fitted and then averaged, as shown in Figure 7D. However, even in this case there is little change in the calculated value from samples with up to 10 wt % sediment added.

Using a value averaged across a map, with appropriate uncertainties, is useful and easy to interpret. However, information is lost in the process of averaging, even when applying the metrics to individual spectra. An alternative approach may be to apply a classification of each spectrum and then to calculate the fractions that are "sediment-like". This can be done in two ways: first, by adopting the approach of Roscher et al. [23] and defining a cut-off in the R^2 value from fitting the 2D peak and, second, by running a non-negative least squares fit and defining a cut-off for the "sediment-like" spectral loading, as implemented above for graphite additions. The value of the threshold has here been set to minimise the mean-squared variance between the calculated fraction and the known loading of sediment material. The estimated sediment content based on the fraction of "sediment-like" spectra for each sample is shown in Figure 8.
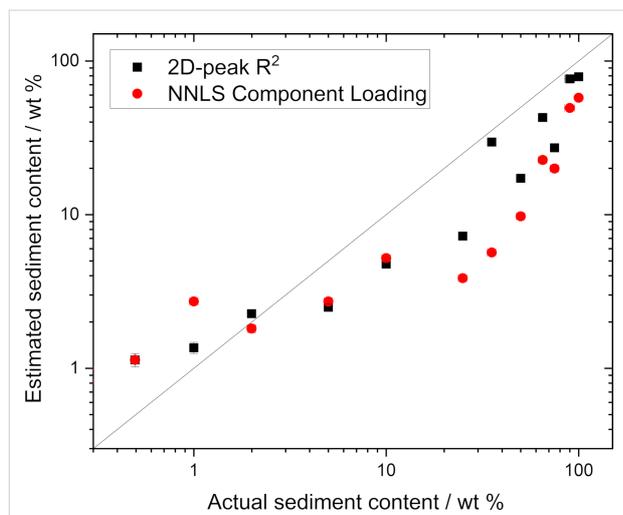
Figure 8: Estimated sediment content calculated from the fraction of measured spectra that are "sediment-like" based on either adjusted R^2 value from fitting the 2D peak or from NNLS fitting. The line shows the expected linear trend, rather than a fit to the data.
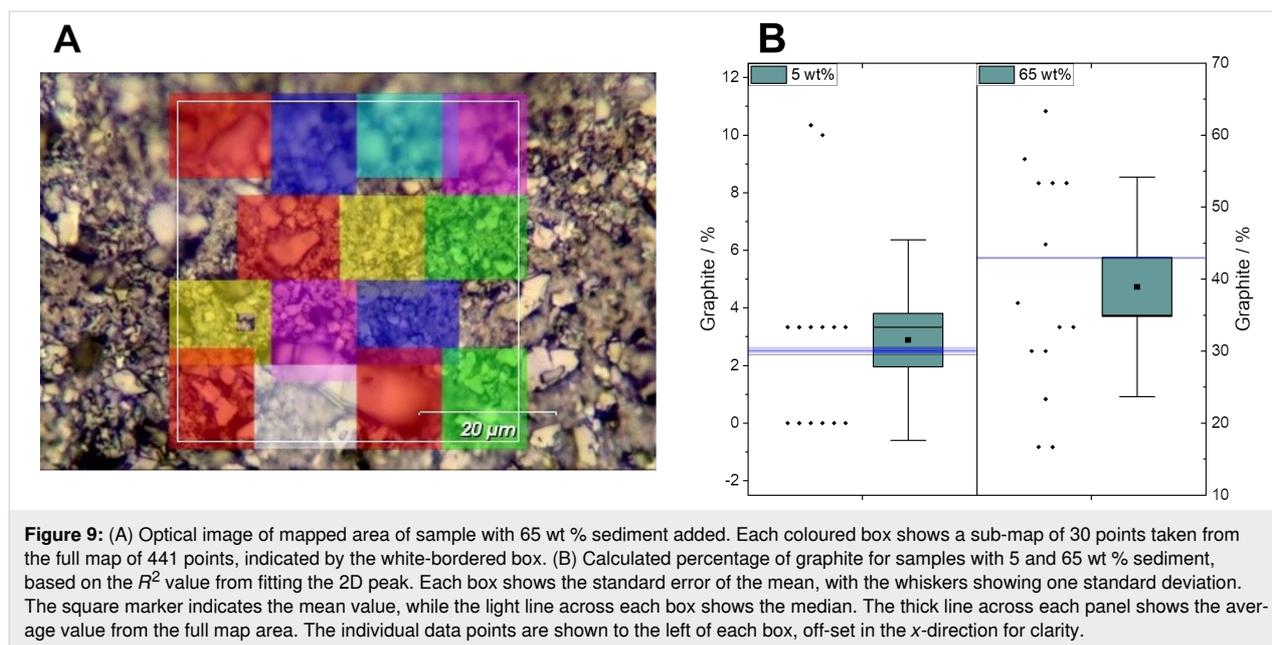
It can be seen that if the individual spectra in the map are classified as "sediment" or "GNP" without any averaging, the presence of this non-GNP material can be identified more reliably than when using averaged values. We have calculated the variance from the nominal loading according to:

$$\frac{\left| f_{\text{pred}} - f_{\text{nom}} \right|}{f_{\text{nom}}} \times 100, \qquad (4)$$

where f_{pred} is the fraction of sediment predicted by the metric, and f_{nom} is the weight fraction of added sediment. The largest variation is still seen at the lowest loading of sediment. Using a threshold value of 1.09×10^{-3}, the mean absolute deviation from the expected value is 73% with a maximum of 172% for 1 wt % using the NNLS fitting. Using the R^2 value from the 2D peak fit with a threshold of 0.949 gives a mean absolute deviation of 47%, with a maximum of 129% for the 0.5 wt % sample. Tables with the full values of the predicted sediment content and the variance and the ratio between nominal and predicted values are provided in Supporting Information File 1, Table S1 and Table S2. It is a useful finding that the mean deviation is lower for the R^2 approach as this approach is significantly easier to implement computationally and the spectra of the pure components are not required. This ease of implementation is critical when designing a quality control system. However, it is important to keep in mind that the value of R^2 obtained is affected by the signal-to-noise ratio of the spectrum (see Supporting Information File 1, Figure S4 and Figure S5). We therefore do not intend to suggest that the values of the thresholds given here are universal values.

It is important to consider that the sediment component is present in discrete particles, which are significantly larger than the GNP particles and generally larger than the laser spot size (above 1 μm with 100× objective lens). Due to the larger size and thickness of the sediment particles compared to the GNP particles, a given weight fraction of sediment will correspond to a significantly lower number fraction of particles [40]. This difference will be more pronounced at low mass loading of sediment, where a small number of particles will be needed to provide the required mass. This increases the likelihood that the area mapped does not contain a representative number of sediment particles and may therefore skew the results. To investigate this effect, we have taken the samples with 5 wt % and 65 wt % sediment, and calculated the metrics obtained from smaller sub-maps, as shown in Figure 9. Figure 9A shows the white-light image of the sample with 65 wt % sediment addition, with the sub-maps used overlaid.

When taking 14 sub-maps of 30 points and applying the criteria for "sediment-like" spectrum defined above for the R^2 value of 2D peak fitting, the fraction of sediment measured varied from 0% to 10.3%, with a mean value of 2.9% ± 0.2%, with a standard deviation of 3.5%. Similarly, for the sample with 65 wt % sediment, the values range from 16.7% to 63.3%, with a mean value of 38.9% ± 1.1% and standard deviation of 15.3%. It is therefore clear that if only a small number of points are measured, it is possible to record a significant variation in the measured concentration of sediment in a sample. Indeed, for the 5 wt % GNP$_{\text{ref}}$ sample, six of the sub-map analyses would indi-

Figure 9: (A) Optical image of mapped area of sample with 65 wt % sediment added. Each coloured box shows a sub-map of 30 points taken from the full map of 441 points, indicated by the white-bordered box. (B) Calculated percentage of graphite for samples with 5 and 65 wt % sediment, based on the R^2 value from fitting the 2D peak. Each box shows the standard error of the mean, with the whiskers showing one standard deviation. The square marker indicates the mean value, while the light line across each box shows the median. The thick line across each panel shows the average value from the full map area. The individual data points are shown to the left of each box, off-set in the *x*-direction for clarity.

cate that there is no sediment present. These results emphasise the importance of acquiring a large number of spectra from a sufficiently wide area of the sample to ensure representative sampling. This is in line with Coleman et al. [41] who have previously discussed the issue of sampling.

Conclusion

While Raman spectroscopy is a powerful and widely used technique to characterize graphene-related 2D materials, this work shows that care is needed when interpreting measurements from bulk samples containing many particles. Measurements on individual graphitic particles can distinguish between graphite, few-layer graphene, and graphene. However, measurements on mass-produced samples can be more difficult to interpret. In this case, which is more similar to the requirements of a quality control process for industrially produced powders containing GNPs, each measurement location will be sampling multiple particles, which will have different number of layers and lateral sizes.

We have shown in this work that when measuring samples with significant fractions of unexfoliated material, quantification can be difficult. When analysing the average spectrum from a large number of locations in a bulk sample, the presence of up to 10 wt % graphite can not be reliably identified. When adding processed graphite ("sediment") into samples, this limit is extended up to 50 wt % when analysing the averaged spectrum. However, we have shown that if individual measurement locations are analysed and classified separately, it is possible to identify the presence of this material in the sample, although quantification of the amount remains approximate. As has been

shown previously, for this to be reliable, a large number of spectra need to be measured to ensure representative sampling of the material.

In light of these results, it is suggested that while Raman spectroscopy remains a powerful tool, in order to reliably identify the presence of graphite material in a GNP sample, individual spectra need to be analysed and classified before averaging. Using a metric based around the residual of a simple peak fitting means that this can be implemented in an automated, unsupervised method. This is essential for the use in a quality control process for industrial production of materials.

Supporting Information

Supporting Information File 1
Additional experimental data.
[https://www.beilstein-journals.org/bjnano/content/supplementary/2190-4286-14-42-S1.pdf]

ORCID® iDs

Keith R. Paton - https://orcid.org/0000-0003-0300-8676
Konstantinos Despotelis - https://orcid.org/0000-0002-2490-7868
Naresh Kumar - https://orcid.org/0000-0001-8953-5420
Piers Turner - https://orcid.org/0000-0002-3644-0636
Andrew J. Pollard - https://orcid.org/0000-0002-6841-2592

References

1. Inoveight Limited Inov-8 Unveil World's First-Ever Graphene Sports Shoes, 2018.
   https://www.inov-8.com/eu/graphene-launch-press-release (accessed April 3, 2023).
2. Vittoria S.p.A. Bicycle tires - powered by graphene (2017).
   https://www.vittoria.com/ww/en/technology/graphene (accessed April 3, 2023).
3. Huawei Technologies Co. Ltd. Huawei Achieves Major Breakthrough in Graphene-Assisted High Temperature Li-ion Batteries (2016).
   https://www.huawei.com/en/news/2016/12/Graphene-Assisted-Li-ion-Batteries (accessed April 3, 2023).
4. The Ford Motor Company Cell phones, sporting goods, and soon, cars: Ford innovates with "miracle" material, powerful graphene for vehicle parts (2018).
   https://media.ford.com/content/fordmedia/feu/en/news/2018/10/09/ford-innovates-with-miracle-material-powerful-graphene-for-vehicle-parts.html (accessed April 3, 2023).
5. SIO Grafen, Graphene Supplier Guide. https://suppliers.siografen.se/.
6. ISO, Nanotechnologies — Vocabulary. In *Part 13: Graphene and related two-dimensional (2D) materials*, 2016; Vol. ISO/TS 80004-13:2017. https://www.iso.org/standard/64741.html (accessed April 3, 2023).
7. Nanotechnologies — Structural characterization of graphene. In *Part 1: Graphene from powders and dispersions*, 2021; Vol. ISO/TS 21356-1:2021(E). https://www.iso.org/standard/70757.html (accessed April 3, 2023).
8. Ferrari, A. C.; Basko, D. M. *Nat. Nanotechnol.* **2013,** *8,* 235–246. doi:10.1038/nnano.2013.46
9. Févotte, G. *Chem. Eng. Res. Des.* **2007,** *85,* 906–920. doi:10.1205/cherd06229
10. Echtermeyer, A.; Marks, C.; Mitsos, A.; Viell, J. *Appl. Spectrosc.* **2021,** *75,* 506–519. doi:10.1177/0003702820973275
11. Harting, J.; Kleinebudde, P. *Eur. J. Pharm. Biopharm.* **2018,** *125,* 169–181. doi:10.1016/j.ejpb.2018.01.015
12. Harms, Z. D.; Shi, Z.; Kulkarni, R. A.; Myers, D. P. *Anal. Chem. (Washington, DC, U. S.)* **2019,** *91,* 8045–8053. doi:10.1021/acs.analchem.8b05002
13. Backes, C.; Paton, K. R.; Hanlon, D.; Yuan, S.; Katsnelson, M. I.; Houston, J.; Smith, R. J.; McCloskey, D.; Donegan, J. F.; Coleman, J. N. *Nanoscale* **2016,** *8,* 4311–4323. doi:10.1039/c5nr08047a
14. Brennan, B.; Centeno, A.; Zurutuza, A.; Mack, P.; Paton, K. R.; Pollard, A. J. *ACS Appl. Nano Mater.* **2021,** *4,* 5187–5197. doi:10.1021/acsanm.1c00519
15. Pollard, A. J.; Brennan, B.; Stec, H.; Tyler, B. J.; Seah, M. P.; Gilmore, I. S.; Roy, D. *Appl. Phys. Lett.* **2014,** *105,* 253107. doi:10.1063/1.4905128
16. Armano, A.; Buscarino, G.; Cannas, M.; Gelardi, F. M.; Giannazzo, F.; Schilirò, E.; Agnello, S. *Carbon* **2018,** *127,* 270–279. doi:10.1016/j.carbon.2017.11.008
17. Lui, C. H.; Malard, L. M.; Kim, S.; Lantz, G.; Laverge, F. E.; Saito, R.; Heinz, T. F. *Nano Lett.* **2012,** *12,* 5539–5544. doi:10.1021/nl302450s
18. Zabel, J.; Nair, R. R.; Ott, A.; Georgiou, T.; Geim, A. K.; Novoselov, K. S.; Casiraghi, C. *Nano Lett.* **2012,** *12,* 617–621. doi:10.1021/nl203359n
19. Ferrari, A. C.; Meyer, J. C.; Scardaci, V.; Casiraghi, C.; Lazzeri, M.; Mauri, F.; Piscanec, S.; Jiang, D.; Novoselov, K. S.; Roth, S.; Geim, A. K. *Phys. Rev. Lett.* **2006,** *97,* 187401. doi:10.1103/physrevlett.97.187401
20. Nemanich, R. J.; Solin, S. A. *Phys. Rev. B* **1979,** *20,* 392–401. doi:10.1103/physrevb.20.392
21. Malard, L. M.; Pimenta, M. A.; Dresselhaus, G.; Dresselhaus, M. S. *Phys. Rep.* **2009,** *473,* 51–87. doi:10.1016/j.physrep.2009.02.003
22. Havener, R. W.; Zhuang, H.; Brown, L.; Hennig, R. G.; Park, J. *Nano Lett.* **2012,** *12,* 3162–3167. doi:10.1021/nl301137k
23. Roscher, S.; Hoffmann, R.; Ambacher, O. *Anal. Methods* **2019,** *11,* 1224–1228. doi:10.1039/c8ay02619j
24. Backes, C.; Abdelkader, A. M.; Alonso, C.; Andrieux-Ledier, A.; Arenal, R.; Azpeitia, J.; Balakrishnan, N.; Banszerus, L.; Barjon, J.; Bartali, R.; Bellani, S.; Berger, C.; Berger, R.; Ortega, M. M. B.; Bernard, C.; Beton, P. H.; Beyer, A.; Bianco, A.; Bøggild, P.; Bonaccorso, F.; Barin, G. B.; Botas, C.; Bueno, R. A.; Carriazo, D.; Castellanos-Gomez, A.; Christian, M.; Ciesielski, A.; Ciuk, T.; Cole, M. T.; Coleman, J.; Coletti, C.; Crema, L.; Cun, H.; Dasler, D.; De Fazio, D.; Díez, N.; Drieschner, S.; Duesberg, G. S.; Fasel, R.; Feng, X.; Fina, A.; Forti, S.; Galiotis, C.; Garberoglio, G.; García, J. M.; Garrido, J. A.; Gibertini, M.; Gölzhäuser, A.; Gómez, J.; Greber, T.; Hauke, F.; Hemmi, A.; Hernandez-Rodriguez, I.; Hirsch, A.; Hodge, S. A.; Huttel, Y.; Jepsen, P. U.; Jimenez, I.; Kaiser, U.; Kaplas, T.; Kim, H.; Kis, A.; Papagelis, K.; Kostarelos, K.; Krajewska, A.; Lee, K.; Li, C.; Lipsanen, H.; Liscio, A.; Lohe, M. R.; Loiseau, A.; Lombardi, L.; Francisca López, M.; Martin, O.; Martín, C.; Martínez, L.; Martin-Gago, J. A.; Ignacio Martínez, J.; Marzari, N.; Mayoral, Á.; McManus, J.; Melucci, M.; Méndez, J.; Merino, C.; Merino, P.; Meyer, A. P.; Miniussi, E.; Miseikis, V.; Mishra, N.; Morandi, V.; Munuera, C.; Muñoz, R.; Nolan, H.; Ortolani, L.; Ott, A. K.; Palacio, I.; Palermo, V.; Parthenios, J.; Pasternak, I.; Patane, A.; Prato, M.; Prevost, H.; Prudkovskiy, V.; Pugno, N.; Rojo, T.; Rossi, A.; Ruffieux, P.; Samorì, P.; Schué, L.; Setijadi, E.; Seyller, T.; Speranza, G.; Stampfer, C.; Stenger, I.; Strupinski, W.; Svirko, Y.; Taioli, S.; Teo, K. B. K.; Testi, M.; Tomarchio, F.; Tortello, M.; Treossi, E.; Turchanin, A.; Vazquez, E.; Villaro, E.; Whelan, P. R.; Xia, Z.; Yakimova, R.; Yang, S.; Yazdi, G. R.; Yim, C.; Yoon, D.; Zhang, X.; Zhuang, X.; Colombo, L.; Ferrari, A. C.; Garcia-Hernandez, M. *2D Mater.* **2020,** *7,* 022001. doi:10.1088/2053-1583/ab1e0a
25. Paton, K. R.; Varrla, E.; Backes, C.; Smith, R. J.; Khan, U.; O'Neill, A.; Boland, C.; Lotya, M.; Istrate, O. M.; King, P.; Higgins, T.; Barwich, S.; May, P.; Puczkarski, P.; Ahmed, I.; Moebius, M.; Pettersson, H.; Long, E.; Coelho, J.; O'Brien, S. E.; McGuire, E. K.; Sanchez, B. M.; Duesberg, G. S.; McEvoy, N.; Pennycook, T. J.; Downing, C.; Crossley, A.; Nicolosi, V.; Coleman, J. N. *Nat. Mater.* **2014,** *13,* 624–630. doi:10.1038/nmat3944

26. Backes, C.; Higgins, T. M.; Kelly, A.; Boland, C.; Harvey, A.; Hanlon, D.; Coleman, J. N. *Chem. Mater.* **2017,** *29,* 243–255. doi:10.1021/acs.chemmater.6b03335

27. Backes, C.; Szydłowska, B. M.; Harvey, A.; Yuan, S.; Vega-Mayoral, V.; Davies, B. R.; Zhao, P.-l.; Hanlon, D.; Santos, E. J. G.; Katsnelson, M. I.; Blau, W. J.; Gadermaier, C.; Coleman, J. N. *ACS Nano* **2016,** *10,* 1589–1601. doi:10.1021/acsnano.5b07228

28. Paton, K. R.; Coleman, J. N. *Carbon* **2016,** *107,* 733–738. doi:10.1016/j.carbon.2016.06.043

29. Marchesini, S.; Turner, P.; Paton, K. R.; Reed, B. P.; Pollard, A. J. *Nanoscale* **2021,** *13,* 14518–14524. doi:10.1039/d1nr03361a

30. Cançado, L. G.; Jorio, A.; Pimenta, M. A. *Phys. Rev. B* **2007,** *76,* 064304. doi:10.1103/physrevb.76.064304

31. Tuinstra, F.; Koenig, J. L. *J. Chem. Phys.* **1970,** *53,* 1126–1130. doi:10.1063/1.1674108

32. Ferrari, A. C.; Robertson, J. *Phys. Rev. B* **2000,** *61,* 14095–14107. doi:10.1103/physrevb.61.14095

33. Kauling, A. P.; Seefeldt, A. T.; Pisoni, D. P.; Pradeep, R. C.; Bentini, R.; Oliveira, R. V. B.; Novoselov, K. S.; Castro Neto, A. H. *Adv. Mater. (Weinheim, Ger.)* **2018,** *30,* 1803784. doi:10.1002/adma.201803784

34. Yoon, D.; Moon, H.; Cheong, H.; Choi, J.; Choi, J.; Park, B. *J. Korean Phys. Soc.* **2009,** *55,* 1299–1303. doi:10.3938/jkps.55.1299

35. Workman, J., Jr. *Spectroscopy* **2010,** *25,* 16–21.

36. Ciesielski, A.; Haar, S.; El Gemayel, M.; Yang, H.; Clough, J.; Melinte, G.; Gobbi, M.; Orgiu, E.; Nardi, M. V.; Ligorio, G.; Palermo, V.; Koch, N.; Ersen, O.; Casiraghi, C.; Samorì, P. *Angew. Chem., Int. Ed.* **2014,** *53,* 10355–10361. doi:10.1002/anie.201402696

37. Haar, S.; Ciesielski, A.; Clough, J.; Yang, H.; Mazzaro, R.; Richard, F.; Conti, S.; Merstorf, N.; Cecchini, M.; Morandi, V.; Casiraghi, C.; Samorì, P. *Small* **2015,** *11,* 1691–1702. doi:10.1002/smll.201402745

38. Shin, Y.; Prestat, E.; Zhou, K.-G.; Gorgojo, P.; Althumayri, K.; Harrison, W.; Budd, P. M.; Haigh, S. J.; Casiraghi, C. *Carbon* **2016,** *102,* 357–366. doi:10.1016/j.carbon.2016.02.037

39. Nagyte, V.; Kelly, D. J.; Felten, A.; Picardi, G.; Shin, Y.; Alieva, A.; Worsley, R. E.; Parvez, K.; Dehm, S.; Krupke, R.; Haigh, S. J.; Oikonomou, A.; Pollard, A. J.; Casiraghi, C. *Nano Lett.* **2020,** *20,* 3411–3419. doi:10.1021/acs.nanolett.0c00332

40. Silva, D. L.; Campos, J. L. E.; Fernandes, T. F. D.; Rocha, J. N.; Machado, L. R. P.; Soares, E. M.; Miquita, D. R.; Miranda, H.; Rabelo, C.; Vilela Neto, O. P.; Jorio, A.; Cançado, L. G. *Carbon* **2020,** *161,* 181–189. doi:10.1016/j.carbon.2020.01.050

41. Goldie, S. J.; Bush, S.; Cumming, J. A.; Coleman, K. S. *ACS Appl. Nano Mater.* **2020,** *3,* 11229–11239. doi:10.1021/acsanm.0c02361

Upscaling the urea method synthesis of CoAl layered double hydroxides

Camilo Jaramillo-Hernández[1], Víctor Oestreicher[1], Martín Mizrahi[2,3]
and Gonzalo Abellán[*1]

Address:
[1]Instituto de Ciencia Molecular (ICMol). Universidad de Valencia, Catedrático José Beltrán 2, Paterna, Valencia, 46980, Spain, [2]Instituto de Investigaciones Fisicoquímicas Teóricas y Aplicadas (INIFTA), Departamento de Química, Facultad de Ciencias Exactas. Universidad Nacional de La Plata, CCT La Plata- CONICET. Diagonal 113 y 64, 1900, La Plata, Argentina and [3]Facultad de Ingeniería, Universidad Nacional de La Plata. Calle 1 esq. 47, 1900, La Plata, Argentina

Email:
Gonzalo Abellán[*] - gonzalo.abellan@uv.es

* Corresponding author

Keywords:
Co-based hydroxides; layered double hydroxide; layered materials; scale-up process; synthesis; two-dimensional materials

Abstract

Research on two-dimensional materials is one of the most relevant fields in materials science. Layered double hydroxides (LDHs), a versatile class of anionic clays, exhibit great potential in photocatalysis, energy storage and conversion, and environmental applications. However, its implementation in real-life devices requires the development of efficient and reproducible large-scale synthesis processes. Unfortunately, reliable methods that allow for the production of large quantities of two-dimensional LDHs with well-defined morphologies and high crystallinity are very scarce. In this work, we carry out a scale-up of the urea-based CoAl-LDH synthesis method. We thoroughly study the effects of the mass scale-up (25-fold: up to 375 mM) and the volumetric scale-up (20-fold: up to 2 L). For this, we use a combination of several structural (XRD, TGA, and N_2 and CO_2 isotherms), microscopic (SEM, TEM, and AFM), magnetic (SQUID), and spectroscopic techniques (ATR-FTIR, UV–vis, XPS, ICP-MS, and XANES-EXAFS). In the case of the volumetric scale-up, a reduction of 45% in the lateral dimensions of the crystals (from 3.7 to 2.0 μm) is observed as the reaction volume increases. This fact is related to modified heating processes affecting the alkalinization rates and, concomitantly, the precipitation, even under recrystallization at high temperatures. In contrast, for the tenfold mass scale-up, similar morphological features were observed and assigned to changes in nucleation and growth. However, at higher concentrations, simonkolleite-like Co-based layered hydroxide impurities are formed, indicating a phase competition during the precipitation related to the thermodynamic stability of the growing phases. Overall, this work demonstrates that it is possible to upscale the synthesis of high-quality hexagonal CoAl-LDH in a reproducible manner. It highlights the most critical synthesis aspects that must be controlled and provides various fingerprints to trace the quality of these materials. These results will contribute to bringing the use of these 2D layered materials closer to reality in different applications of interest.

Introduction

Since the discovery of graphene [1], research on two-dimensional (2D) materials has become one of the most relevant topics in physics, chemistry, and (nano)materials science [2-4]. These materials play a key role both from a fundamental point of view and regarding potential applications in electronic devices, drug delivery, and energy storage and conversion, to name a few [5-8].

Layered materials range from monoelementals (i.e., graphene, silicene, germanene, or pnictogens (P, As, Sb and Bi)) to multi-elementals (e.g., boron nitrate, metal dichalcogenides, MXenes, layered metal/covalent organic frameworks, or layered hydroxides/oxides) [9-11]. These systems exhibit an enormous variability in their physicochemical properties, which are defined by their layer-to-layer interactions and chemical composition.

One of the most interesting families is that of layered double hydroxides (LDHs), which are characterized by having a positive charge, hence the name "anionic clays". This family exhibits hydrotalcite-like structures consisting of infinite positively charged layers containing M^{II} and M^{III} octahedral cations connected by μ_3-OH bridges that interact electrostatically with interlayer anions. Typically, LDHs can be represented by the chemical formula $[M^{II}_{1-x}M^{III}_x(OH)]^{x+}(A^{n-})_{x/n}(Sv)_m$, where M represents cations (e.g., Mg, Zn, Co, Ni, Cu, Al, Fe, or Cr) and x the metallic ratio (typically, $0.20 < x < 0.33$). A^{n-} symbolizes a constituent ranging from (in)organic anions to macromolecules, and Sv stands for solvent molecules. This general composition leads to a plethora of highly tunable systems [12-16] with relevance in environmental applications [17], photocatalysis [18], energy storage and conversion [19-21], quantum materials [22,23], and others [24]. This wide range of potential applications makes the development of reliable scaling processes crucial.

Usually, LDHs are obtained by different synthesis procedures such as co-precipitation [25], hydrothermal synthesis [13], sol–gel methods [26], mechanochemistry [27], or the epoxide route [28], to name a few [29]. Among them, hydrothermal methods based on ammonium-releasing reagents (ARRs), commonly urea or hexamethylenetetramine, are especially interesting since they allow one to obtain large and highly crystalline particles [30-32]. The ARR decomposes at temperatures above 70 °C, which leads to the alkalinization of a solution containing cation reagents, eventually triggering the precipitation of LDHs [13,33-35]. The experimental conditions (concentration, solvent mixture, and temperature) will define the alkalinization rate, which (mainly) controls the nucleation and growth processes, and therefore particle size, morphology, and crystallinity [33,36,37].

Attempts to upscale the production of LDHs included incrementing the concentration of the reactants [38,39], the use of large-scale reactors [40,41], byway co-precipitation, and mechanochemical approaches [27]. Although these methods can produce materials on a large scale, they are very limited in providing materials with controlled morphology, size, or crystallinity [42]. This issue can be partially solved using continuous flow techniques [43,44]. Yet, reliable scaling methods that allow for the production of large quantities of two-dimensional LDHs with well-defined morphologies and high crystallinity are very scarce.

Herein, we thoroughly study the scale-up of CoAl-LDH synthesis by a urea alkalization method. We explore both volumetric (increment in reactor size) and mass (increment in the reagent concentration) scale-up processes. In the mass scale-up process, the increment in the concentration (25-fold that of the reference condition) triggers the appereance of simonkolleite-like Co-based impurities due to phase competition during the precipitation process (thermodynamic aspects). In the volumetric approach, pure CoAl-based LDHs are obtained, size and shape (edge sharpness) of which highly depend on the heating procedure, even after 48 h of recrystallization (kinetic aspects). Our results suggest that either an up to tenfold mass scale-up or a 20-fold volumetric scale-up can provide pure CoAl-based LDH materials exhibiting comparable morphology and crystallinity.

Interestingly, while in the case of the volumetric scale-up, the kinetic issues could be solved by a better control over the heating process, the thermodynamic aspects (phase competition) [30,45] exclusively depend on the nature of the involved cations.
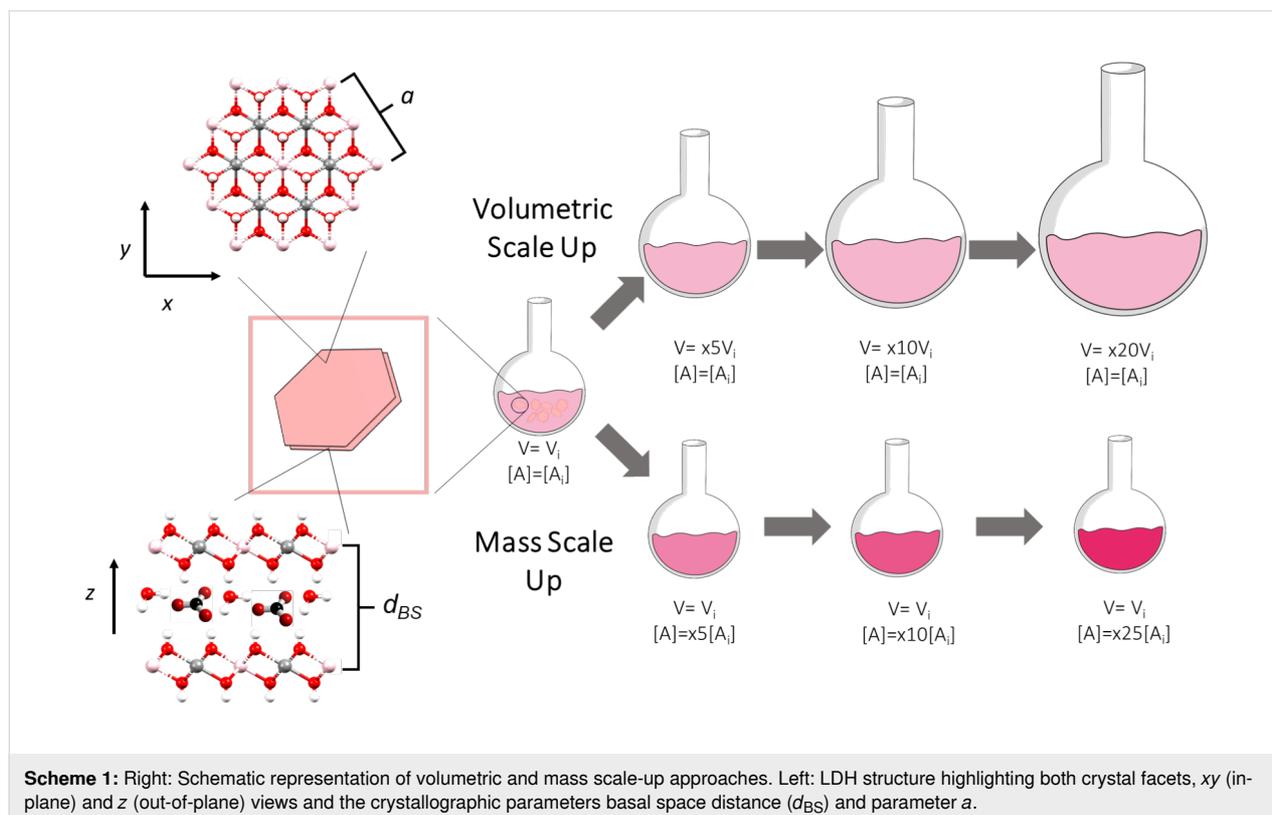
Results and Discussion

In order to analyse the effect of the scale-up on the obtained LDH materials, we have selected as reference the experimental conditions for the synthesis of CoAl-LDHs reported by Liu et al. [13], which currently arises as one of the most cited papers describing the synthesis of LDH phases. The aforementioned experimental conditions have been labeled as "x1". The experiments featuring an increment in the initial volume (i.e., volumetric scale-up) or initial reagent concentration (i.e., mass scale-up) will be designated as xYV and xYM, respectively. Here, Y is the factor of the scale-up. In the case of the mass scale-up, a 100 mL two-necked round bottom flask was employed. For the volumetric scale-up, different two-neck round bottom flasks ranging from 500 to 2000 mL were used. In all experiments, the same hotplate stirrer RET Basic (IKA, Germany) was used to keep the temperature at 97 °C. The whole synthesis process (heating, precipitation and cooldown)
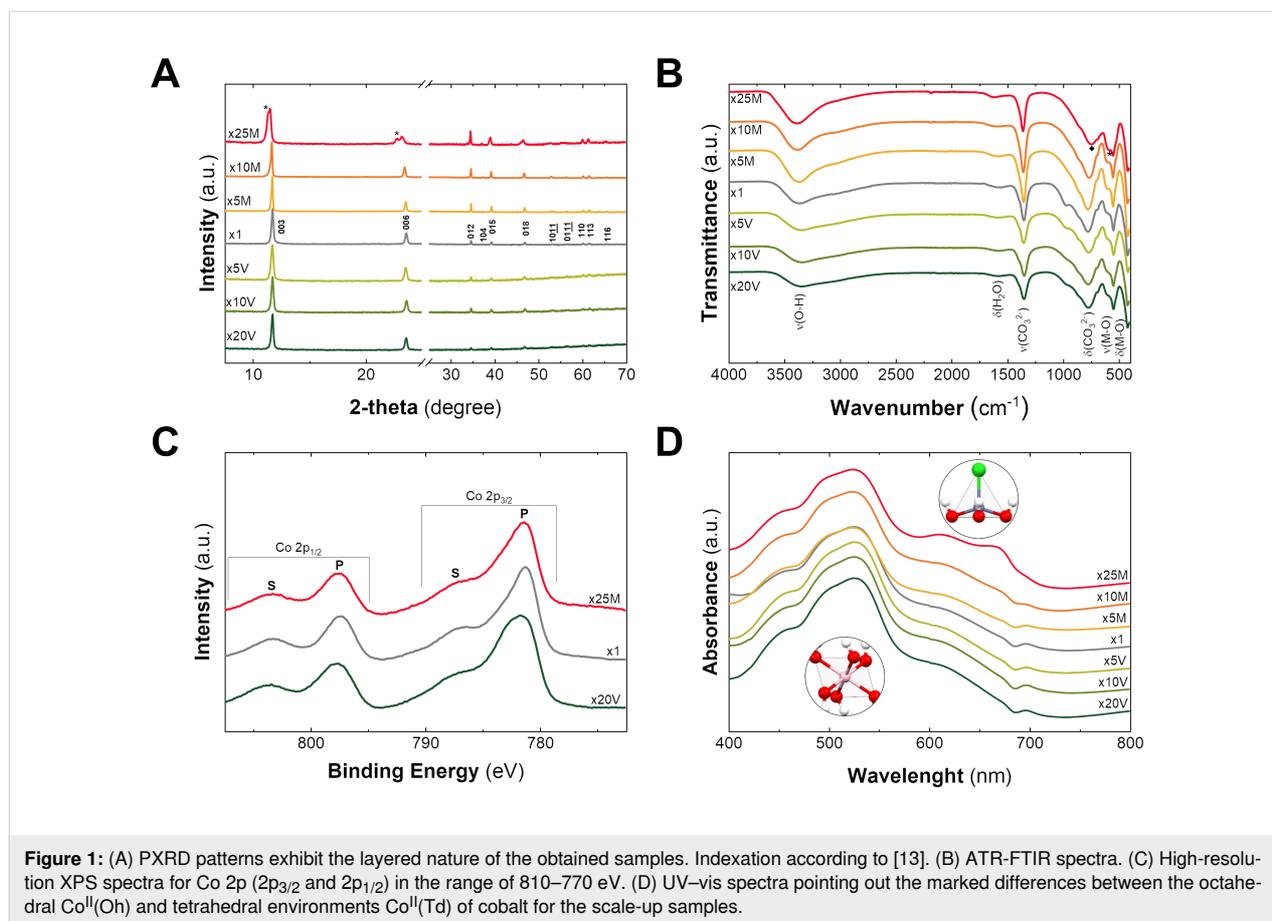
was carried out under stirring (750 rpm). Scheme 1 depicts the experimental approach of this work, highlighting key structural parameters of the CoAl-based LDH structure.

Figure 1A depicts the PXRD patterns for the obtained pale pink solid samples. The pattern of reference sample x1 exhibits the typical reflections expected for a CoAl-LDH structure. Specifically, the two main signals located at 11.72° and 23.62°, indexed as (003) and (006), are assigned to the interlayer reflections, revealing a basal space distance (d_{BS}) of 7.56 Å. This value is in perfect agreement with a CoAl LDH phase containing carbonate as interlayer anion [13]. Furthermore, from the signal at around 60°, corresponding to the (110) planes, the parameter *a* (related to the M–O distance) can be estimated to a value of 3.07 Å, which is in agreement with a CoAl-based LDH exhibiting a Co/Al ratio of 2:1 [13,15]. The scale-up samples depict PXRD patterns similar to that of reference x1, suggesting the formation of analogous CoAl LDH phases. However, in the case of sample x25M, the existence of a second set of interlayer reflections (denoted with asterisks in Figure 1A), corresponding to a layered structure with d_{BS} = 7.8 Å, suggests the presence of an impurity. Also, the (003) reflection of x10M exhibits an asymmetry in comparison to samples x1 and x10V (see Figure S1 and Figure S2, Supporting Information File 1). Table S1 summarizes the values of d_{BS} and parameter *a* for all samples.

Attenuated total reflectance Fourier-transform infrared spectroscopy (ATR-FTIR) provides valuable information about the nature of the layered hydroxide structure and the intercalated anions (Figure 1B). In the case of the reference x1, the spectrum displays a broad signal at ca. 3400 cm^{-1}, which corresponds to the OH stretching vibrations typically attributed to interlayer water molecules, as confirmed by the extra signal at 1600 cm^{-1} (water bending mode). The presence of carbonate as interlayer anion is confirmed by the vibration bands centered at 1350 and 775 cm^{-1}. Finally, peaks below 750 cm^{-1} are related to the Co/Al–O vibrational bands [13,46,47]. Overall, a CoAl-LDH containing carbonate as interlayer anion is observed. Interestingly, in the case of sample x25M, a shift in the carbonate bending signal (from 775 to 740 cm^{-1}, denoted with a diamond) and the appearance of a shoulder at 581 cm^{-1} (denoted with an asterisk) indicate the presence of the impurity already observed by PXRD (see also Supporting Information File 1, Figure S3) [48].

Aiming to determine the identity of the impurity observed in sample x25M, X-ray photoelectron spectroscopy (XPS) was conducted (Figure 1C). In the case of reference x1, the observed main peaks at 781.23 eV (Co $2_{3/2}$) and 797.36 eV (Co $2_{1/2}$), as well as their satellites at 783.13 and 798.83 eV, confirm the occurrence of Co^{II} [15,49]. The XPS spectra of the samples x20V and x25M are indistinguishable from that of

Scheme 1: Right: Schematic representation of volumetric and mass scale-up approaches. Left: LDH structure highlighting both crystal facets, *xy* (in-plane) and *z* (out-of-plane) views and the crystallographic parameters basal space distance (d_{BS}) and parameter *a*.

Figure 1: (A) PXRD patterns exhibit the layered nature of the obtained samples. Indexation according to [13]. (B) ATR-FTIR spectra. (C) High-resolution XPS spectra for Co 2p ($2p_{3/2}$ and $2p_{1/2}$) in the range of 810–770 eV. (D) UV–vis spectra pointing out the marked differences between the octahedral $Co^{II}(Oh)$ and tetrahedral environments $Co^{II}(Td)$ of cobalt for the scale-up samples.

reference x1, suggesting the lack of Co^{III} in the impurity of sample x25M. Supporting Information File 1, Table S2 compiles further information related to the XPS signals.

Finally, UV–vis spectroscopy has demonstrated to be a powerful technique for layered hydroxide characterization, especially in the case of earth-abundant 3d cations where this technique can provide information about coordination environments and oxidation states [50]. The spectrum of reference x1 depicts a main signal at 525 nm containing high-left and low-right shoulders around 492 and 450 nm. The shape and the position of these d–d electronic transition bands are assigned to the $^{4}T_{1g} \rightarrow ^{4}T_{1g}(P)$ and $^{4}T_{1g} \rightarrow ^{4}A_{2g}(F)$ transitions in octahedral divalent cobalt cations ($Co^{II}(Oh)$) [31,51,52]. However, the sample x25M contains an extra band with a double peak around 650 nm resembling that of Co-based simonkolleite-like structures, also known as α-Co LH [31]. Indeed, this signal can be ascribed to the $^{4}A_{2}(F) \rightarrow ^{4}T_{1}(P)$ transition, corresponding to $Co^{II}(Td)$, where the exact position depends on the nature of the coordinated anions [53]. Sample x10M also exhibits this extra band, but less intense and only noticeable when the values of absorbance are normalized (Supporting Information File 1, Figure S4). Thus, considering the peaks at 610 and 665 nm, the

impurity could be associated to a simonkolleite-like α-Co^{II} LH structure (see control experiments and further characterization in Figure S5 and Figure S6, Supporting Information File 1). Regarding sample x10M, the asymmetry of the (003) reflection observed in PXRD can be an indicator of the presence of an impurity. Furthermore, we have characterized these samples by conventional SQUID magnetic measurements. Despite the acute differences in the magnetic behavior of Co-based LDH and simonkolleite-like α-LH [46,54,55], the impurities do not lead to significant changes beyond slight variations in the DC magnetic susceptibility and the out-of-phase contribution of the dynamic susceptibility (Figure S7 and Figure S8, Supporting Information File 1).

The appearance of α-Co LH with increasing reagent concentration (sample x25M) indicates a typical precipitation competition scenario, where the initial conditions can modify the relative thermodynamic stability of the growing phases. Indeed, the occurrence of α-Co LH as an impurity in the early precipitation stages has been already reported in the case of the synthesis of β-$Co(OH)_2$ [30] and CoAl-based LDHs [45]. Since this phase competition is ruled by thermodynamic aspects, its occurrence will depend on the chemical identity of the involved cations

[30,45,56-58]. This has been observed in different large-scale approaches, where different phases besides hydroxides have been observed at high concentrations [59,60].

In order to provide a comprehensive understanding of the electronic and structural features resulting from the scale-up process and aiming to quantify the amount of this Co-based α-LH impurity, X-ray absorption spectroscopy (XAS) measurements were performed at the CLÆSS BL22 beamline at the ALBA synchrotron. Figure 2A depicts the X-ray absorption near-edge structure (XANES) spectra for the Co K edge. In all samples, the presence of Co^{II} is confirmed regardless of the synthesis conditions [31,50,61]. Nevertheless, sample x25M shows differences in the intensity of the white line and in the resonances behind the absorption edge, compared to the other samples studied. At first glance, this would indicate that, although all Co atoms are in the same oxidation state (2+), they would be found in different environments, as suggested by PXRD and confirmed by UV–vis spectroscopy. This means the presence of the α-Co^{II} LH impurity. To quantify its fraction, the spectrum of sample x25M was reproduced by using a linear combination of CoAl-LDH and α-Co^{II} LH reference spectra. Figure 2B depicts the result of the fits, where excellent agreement is achieved using 57% of LDH and 43% of α-Co^{II} LH. This analysis is an excellent example to show that XANES is a useful technique for LH structure quantification. A detailed description of the structural features of the scale-up samples determined by extended X-ray absorption fine structure (EXAFS) measurements, the used model, and the corresponding fits can be found in Supporting Information File 1 (Figure S9 and Table S3).

Thermal decomposition in both inert (nitrogen) and oxidative (air) atmospheres was measured through thermogravimetric analysis (TGA). Typically, the decomposition of layered hydroxide structures consists of at least two main mass loss steps. The first, below 200 °C, is related to the release of physisorbed and interlayer water. The second one consists of the loss/decomposition of the interlayer anion and the concomitant dehydroxylation process, which leads to the collapse of the layered hydroxide structure [13,54]. The TGA curve of reference x1 in air (Figure 3) shows a first mass loss step of ca. 12% at 207 °C and a second one of around 14% at 276 °C, which are in agreement with the literature [13,15]. All pure scale-up sam-
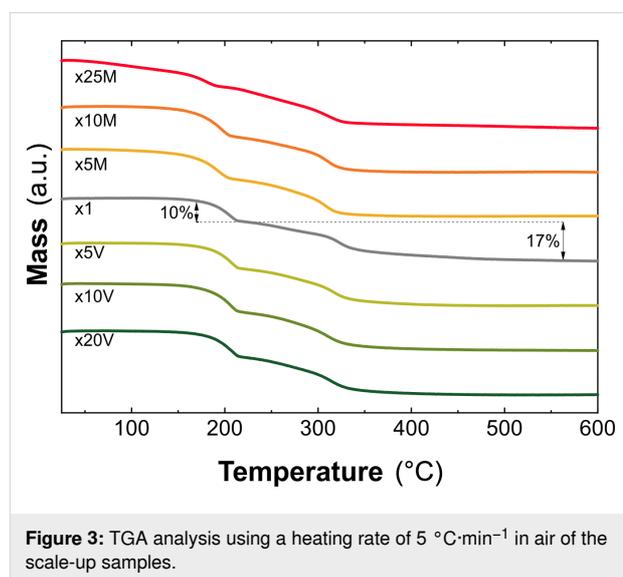
Figure 3: TGA analysis using a heating rate of 5 °C·min^{-1} in air of the scale-up samples.
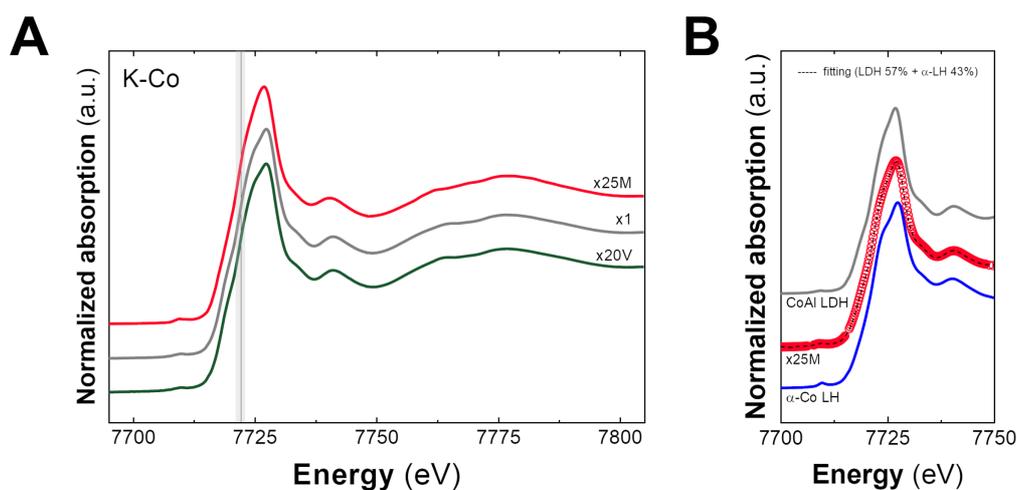
Figure 2: (A) Normalized XANES spectra at the Co K edge for the obtained samples. The grey line depicts the position of the absorption edge characteristic to Co^{II}. (B) Linear fit combination by employing CoAl-LDH and α-Co LH as references, suggesting fractions of 57% of LDH and 43% of the impurity.

ples exhibit the same TGA profile with only subtle differences in terms of mass loss percentage and decomposition temperature (see Supporting Information File 1, Table S4), which in principle could be related to morphological aspects, vide infra. As expected, the PXRD analysis of the calcined solids confirmed the formation of Co_2AlO_4 spinel (see Figure S10, Supporting Information File 1) [62]. Once again, sample x25M shows differences in terms of thermal behavior, resembling simonkolleite-like α-Co^{II} LH samples (see Figure S11, Supporting Information File 1) [30,52,55]. TGA curves in inert atmosphere can be found in Supporting Information File 1, Figure S12.

Inductively coupled plasma mass spectrometry (ICP-MS) was employed to assess quantitatively the precipitation of the cations. It confirmed a Co/Al ratio of 2.0 ± 0.1. Hence, the formation of pure CoAl LDH samples containing carbonate as interlayer anion and exhibiting the chemical formula $[Co_{0.66}^{II}Al_{0.34}^{III}(OH)_2](CO_3)_{0.17}(H_2O)_{0.7}$ (see also Supporting Information File 1, Table S5) can be safely confirmed for both volumetric and mass scale-up approaches, up to 25-fold and tenfold, respectively.

Considering the experimental conditions for the production of pure CoAl-based LDH, we decided to compare the synthesis performance in terms of the space–time yield (STY). The STY value, defined as the amount of material (in kg) that can be produced per volume (in m^3) per day, provides a good parameter to compare different synthesis protocols, as it has been demonstrated for metal-organic frameworks [63-65]. As expected, no-changes in STY values for the volumetric scale-up are observed, while in the case of the mass scale-up, there is a linear relation between STY values and initial concentration (Table 1). Supporting Information File 1, Table S6 compares the obtained STY values with those ones from other synthesis approaches such as co-precipitation and hydrothermal [39-41,65-69], mechanochemistry [27], and continuous flow methods [43,44].
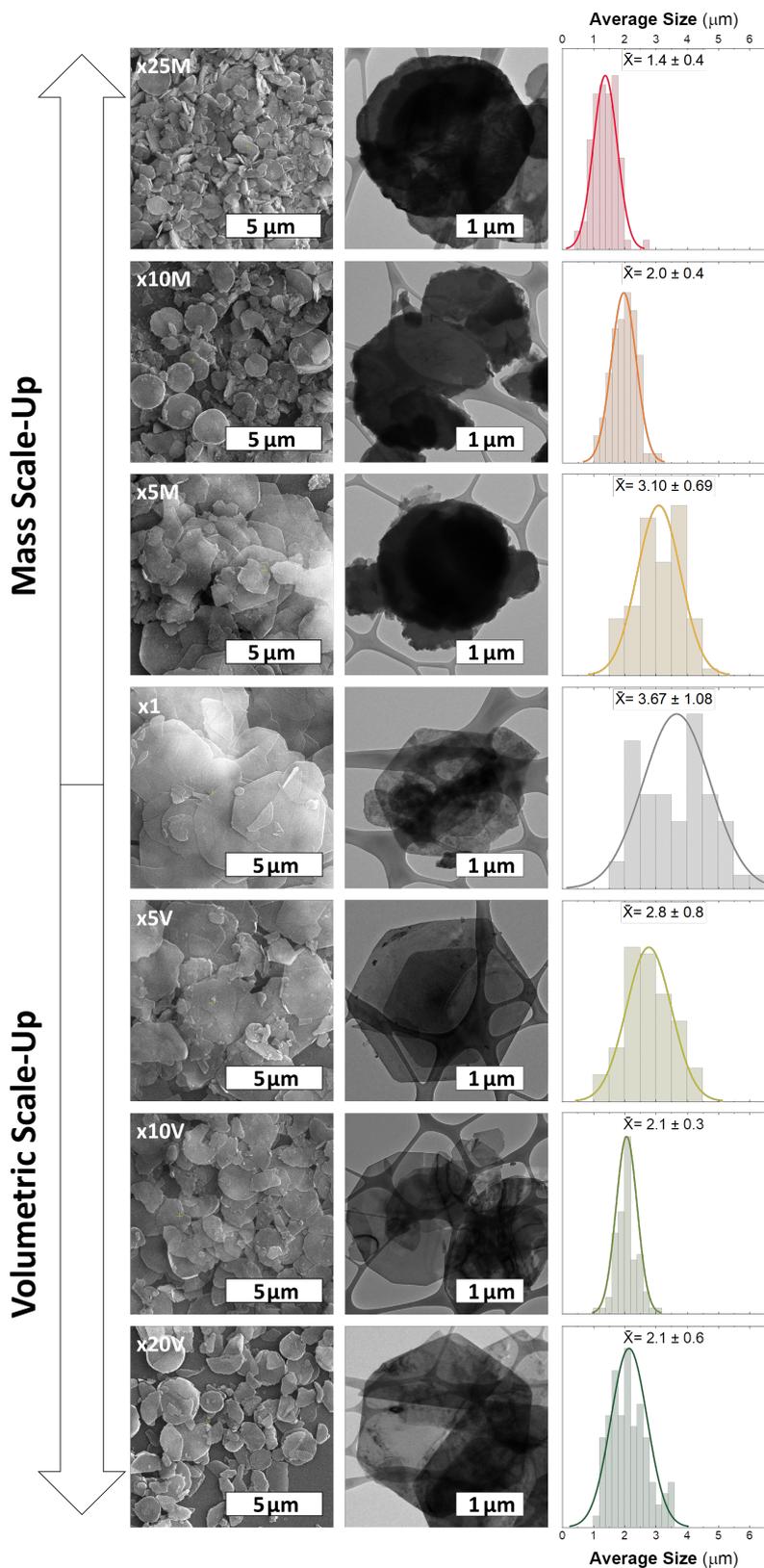
Table 1: Space–time yield (STY) values for the synthesis procedures of pure CoAl-based LDH samples. In all cases, a synthesis time of 48 h is considered. Additionally, $g \cdot L^{-1}$ and $L \cdot kg^{-1}$ values are also provided.

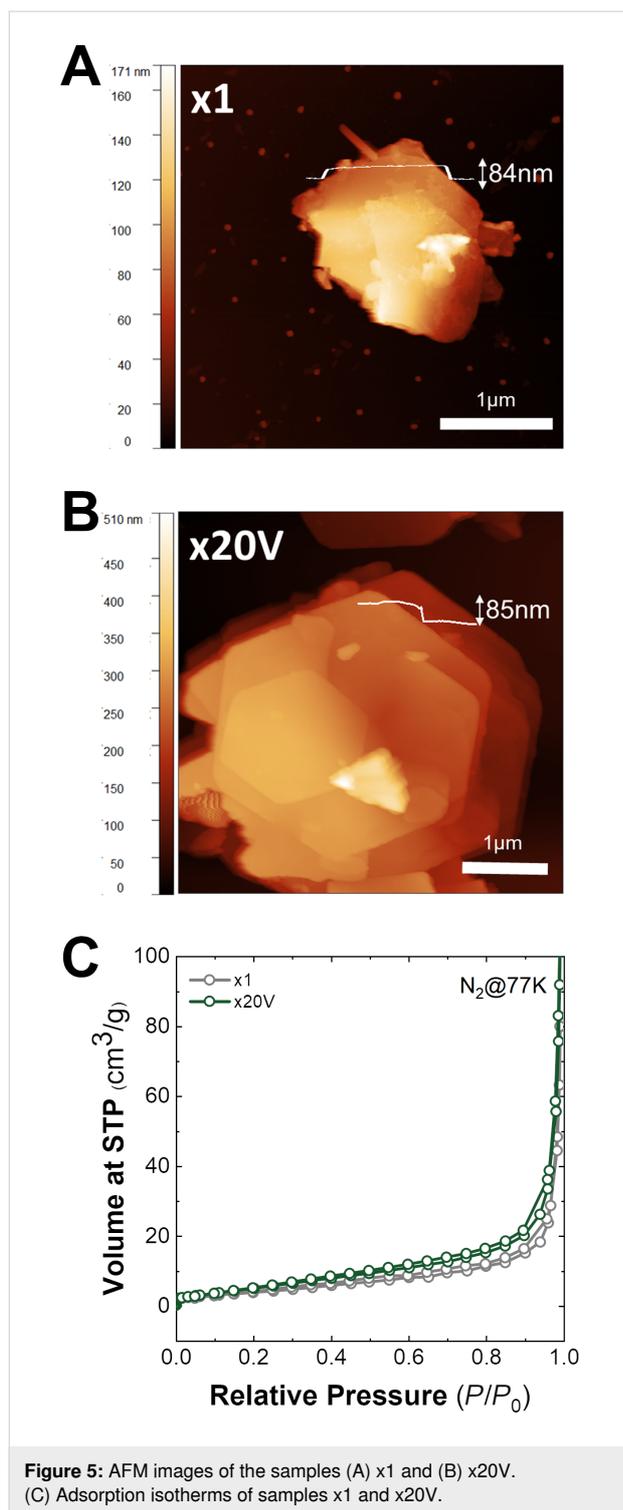| Sample	STY ($kg \cdot m^3 \cdot day^{-1}$)	$g \cdot L^{-1}$	$L \cdot kg^{-1}$
x1	0.23	0.46	2174
x5V	0.23	0.46	2174
x10V	0.23	0.46	2174
x20V	0.23	0.46	2174
x5M	1.15	2.3	434
x10M	2.3	4.6	217

After the limits for the scale-up of CoAl-based LDH synthesis through an ARR method had been demonstrated, morphological aspects were addressed by means of scanning electron microscopy (SEM), transmission electron microscopy (TEM), and atomic force microscopy (AFM) (Figure 4 and Figure 5). For reference x1, well-defined hexagonal single crystals of around 3.7 ± 1.0 μm are observed, in good agreement with [13]. Interestingly, pure CoAl-based LDH scale-up samples exhibit a reduction of around 45% in size and a lack of sharp edges, regardless of the synthesis approach. In the case of mass scale-up protocols, these differences can arise from differences in the nucleation and growth processes because of increased concentration and ionic strength of the reagents, modifying the whole precipitation process [33]. However, the differences are surprising in the case of the volumetric scale-up approach where the initial concentrations were kept constant. Aiming to provide further information, the temperatures of the solutions were measured during the early stage of the volumetric experiments. According to Figure S13 (Supporting Information File 1), the required time to reach the final temperature increases sixfold from reference x1 to sample x20V, evidencing differences in heat transfer. Hence, considering that the precipitation kinetics is controlled by the alkalization process (i.e., the hydrolysis of urea, which depends on the temperature [35]), modifications in the heating process can affect the final size and shape of the particles [69]. This occurs surely through modification of the pristine Al-based hydroxide seeds [28,45,61,70], but even in processes where recrystallization can easily take place. Figure S14 and Table S7 (Supporting Information File 1) summarize the average size and standard deviation values as functions of the experimental conditions extracted from SEM analysis.

Besides slight differences in size and morphology (sharpness of the edges), the AFM comparison of single hexagonal platelets of reference x1 and sample x20V shows a similar thickness of around 85 nm (Figure 5A,B and Supporting Information File 1, Figure S15). Finally, textural properties were also evaluated by N_2 and CO_2 adsorption–desorption isotherms to observe possible changes in the surface area of the samples. Figure 5C shows the N_2 isotherms at 77 K. The samples present type-IV adsorption isotherms (according to IUPAC classification) with an H3 hysteresis loop [71-76] and a low specific surface area (<50 m^2/g) as previously reported [46]. Additional data, such as pore contributions (micro-, meso- and macropores) and other textural parameters, are compiled in Figure S16 and Table S8 (Supporting Information File 1).

To conclude, regarding the obtained pure CoAl-LDHs, both scale-up processes lead to subtle modifications of the morphological aspects, which can be understood in terms of changes in

Figure 4: Microscopic characterization of CoAl-based LDH samples through (left) SEM and (center) TEM, and (right) the respective average size histograms.

Figure 5: AFM images of the samples (A) x1 and (B) x20V. (C) Adsorption isotherms of samples x1 and x20V.

proaches. Pure CoAl-LDH can be obtained up to a tenfold concentration increase with subtle morphological modifications, related to changes in nucleation and growth (ionic strength increment). At a 25-fold concentration increase (x25M), the formation of a simonkolleite-like Co-based layered hydroxide impurity is observed, indicating phase competition during precipitation related to the thermodynamic stability of the growing phases. In the case of the volumetric scale-up, a reduction of ca. 45% of the particle size is observed as the volume increases. This feature is related to changes in the heating process (heat transfer) modifying the alkalinization kinetics and the concomitant precipitation process, even after 48 h of recrystallization. These results suggest that the final LDH morphology (size and sharpness and thickness of edges) is closely related to the growth of $Al(OH)_3$-based seeds.

Hence, while the issues of the volumetric scale-up can be solved by accurate control of the heating process during the reaction, the drawbacks of the mass scale-up depend on the nature of the involved cations, requiring their specific optimization.

Overall, this work demonstrates, by means of several structural, microscopic, and spectroscopic techniques (including XANES-EXAFS synchrotron experiments), that the reproducible large-scale synthesis of high-quality morphologically controlled CoAl-LDHs is feasible, pinpointing the most critical synthesis aspects that should be controlled. Furthermore, this work offers reliable characterization fingerprints for controlling the quality and phase purity of these appealing anionic clays. These results may pave the way for the use of these 2D layered materials in different applications of great interest.

Experimental
Chemicals
Cobalt chloride hexahydrate ($CoCl_2 \cdot 6H_2O$), aluminium chloride hexahydrate ($AlCl_3 \cdot 6H_2O$), urea, and ethanol (EtOH) were purchased from Honeywell. All chemicals were used as received. Milli-Q water was obtained from a Millipore Milli-Q equipment.

Synthesis
Synthesis method based on urea hydrolysis
The synthesis of the CoAl layered double hydroxide phase was carried out by hydrolysis of urea in a two-neck flask (with a reflux condenser) using 50 mL of an aqueous solution of the metal salts at 97 °C for 48 h under Ar atmosphere. The system was continuously stirred (750 rpm) during the whole synthesis process (heating, precipitation, and cooldown). Initial concentrations were fixed to $[CoCl_2]$ = 10 mM, $[AlCl_3]$ = 5 mM, and $[urea]$ = 35 mM.

nucleation, growth and precipitation (mass scale-up), and different alkalization rates (volumetric approach).

Conclusion
In this work, the effects of the scale-up of a CoAl-LDH synthesis have been examined for both mass and volumetric ap-

Volumetric scale-up

The volumetric scale-up of the LDH synthesis was carried out by using the same conditions as above, using two-neck round bottom flasks of 500, 1000, and 2000 mL with reaction volumes of 50, 250, 500, and 1000 mL, increasing the initial volume fivefold, tenfold, and 20-fold, respectively.

Mass scale-up

The mass scale-up of the LDH synthesis was carried out by using the same reaction volume as that of the urea hydrolysis, but increasing the concentration of reagents fivefold, tenfold, and 25-fold. The initial concentrations for each sample in the scale-up were fixed to (1) X5M: $[CoCl_2]$ = 50 mM, $[AlCl_3]$ = 25 mM, and [urea] = 175 mM; (2) X10M: $[CoCl_2]$ = 100 mM, $[AlCl_3]$ = 50 mM, and [urea] = 350 mM; and (3) X25M: $[CoCl_2]$ = 250 mM, $[AlCl_3]$ = 125 mM, and [urea] = 875 mM. All obtained solids were filtered, washed three times with H_2O, H_2O/EtOH, and finally with EtOH. The samples were dried at room temperature and kept in desiccators until further characterization.

Synthesis of α-Co layered hydroxide

The α-Co layered hydroxide synthesis was carried out at room temperature by using the epoxide route for a period of 48 h under constant stirring with solutions of $[CoCl_2]$ = 10 mM and [NaCl] = 100 mM, in the presence of glycidol, [Gly] = 500 mM.

Chemical and structural characterization

Powder X-ray powder diffraction (PXRD) patterns were obtained on a PANalytical Empyrean X-ray platform with a capillary platform and copper radiation (Cu Kα = 1.54178 Å). Measurements were carried in triplicate in the 2-theta range of 2–70° with a step size of 0.02°/step and an integration time of 1 s.

Attenuated total reflectance Fourier-transform infrared spectroscopy (ATR-FTIR) spectra were collected on a Bruker alpha II FTIR spectrometer in the 4000–400 cm^{-1} range.

X-ray photoelectron spectroscopy (XPS) measurements were recorded on a Thermo Scientific™ K-alpha X-ray photoelectron spectrometer. Al Kα radiation was employed as X-ray source. For all elements, more than 100 spectra were recorded employing a step of 0.1 eV with a focused spot greater than 400 μm. XPS data were analyzed with the Thermo Avantage v5.9912 software. For the Co fits, FWHM values of 2.2, 2.9, 4.1, and 3.9 eV were employed for P_1, P_2, S_1, and S_2, respectively.

UV–vis absorption spectra of the solid samples were recorded in reflectance mode employing a Jasco V-670 spectrometer.

Thermogravimetric analysis (TGA) was carried out on a Netzsch TG 209 F1 Libra instrument in the 30–900 °C temperature range.

Magnetic data were collected over the bulk material with a Quantum Design superconducting quantum interference device (SQUID) MPMS-XL-5. The magnetic susceptibility of the samples was corrected considering the diamagnetic contributions of their atomic constituents as deduced from Pascal's constant tables and the sample holder. The DC data were recorded under external applied fields of 100 or 1000 Oe in the 2–300 K temperature range. The AC data were collected under an applied field of 3.95 Oe at 997, 333, 110, 10, and 1 Hz. All magnetic measurements were carried out in eicosane, since this diamagnetic material allows for a better immobilization of these small anisotropic crystals, precluding any artefacts in the magnetic measurements.

The porous texture of all prepared materials was characterized by N_2 adsorption at 77 K and CO_2 at 273 K in an AUTOSORB-6 apparatus. Prior to the measurements, the samples were degassed for 4 h at 523 K and 5×10^{-5} bar. The desorption branch of the N_2 isotherm was used to determine the pore size distribution using the BJH method. The surface area was determined using the BET method. The micropores volumes were determined by applying t-plot and DR methods.

X-ray absorption spectroscopy

X-ray absorption spectroscopy (XAS) measurements were performed at the BL-22 (CLÆSS) beamline of the ALBA synchrotron (Barcelona, Spain), proposal: 2022097096. XANES and EXAFS Co K edge spectra were measured at room temperature in transmission mode. Absorbents of as-synthesized fresh samples were prepared by paint spraying on carbon paper. The optimum amount of material for the measurements was calculated by the program "Hephaestus", which is part of the Demeter package [77]. A Si(111) double-crystal monochromator was used to obtain a monochromatic incident beam, and the intensities of incident and transmitted X-rays were measured using two ionization chambers. XAS spectra were collected from 7590 to 8550 eV with a reduced step (0.2 eV) in the XANES region (7690 to 7750 eV). The incident photon energy was calibrated using the first inflection point of the Co K edge (7709 eV) from a Co reference foil. For each sample, six spectra were taken with exposure times of 4 min each to later be averaged. XANES data treatment was performed by subtracting the pre-edge background followed by normalization by extrapolation of a quadratic polynomial fitted at the post-edge region of the spectrum using the ATHENA AUTOBK background removal algorithm [77]. The quantitative analysis of the EXAFS results were performed by modeling and fitting the iso-

lated EXAFS oscillations. The EXAFS oscillations χ(k) were extracted from the experimental data with standard procedures using the Athena program part of the Demeter package. The k^2-weighted χ(k) data, to enhance the oscillations at higher k, were Fourier-transformed. The Fourier transformation was calculated using the sine filtering function. EXAFS modelling was carried out using the ARTEMIS software [77]. Theoretical scattering path amplitudes and phase shifts for all paths used in the fits were calculated using the FEFF9 code [78]. The k range was set from 2.3 to 12.1 Å^{-1}. The passive reduction factor S_0^2 values were restrained to 0.8. This value was obtained from fitting a standard foil of metallic Co and constraining the coordination numbers to the corresponding structure.

Microscopy
Sample preparation
The dried solids were suspended in ethanol and drop cast onto Au TEM grids covered with a lacy carbon film, and the solvent was left to evaporate. SEM samples were prepared from the same solution after 5 min of ultrasonication. The sonicated suspension was spin-coated on a Si wafer (3000 rpm, 40 s), washed with ethanol and dried afterward. For AFM, the samples were diluted in ethanol and drop-cast on a Si/SiO$_2$ wafer. Si/SiO$_2$ wafers were washed by spin-coating ten droplets of acetone and ten droplets of isopropanol prior to sample deposition.

Scanning electron microscopy (SEM)
Scanning electron microscopy data was acquired using a Hitachi S-4800, with a beam energy of 5 keV. The samples on silicon wafers were directly investigated without any surface coating. Energy dispersive X-ray (EDS) spectroscopy studies were performed on a Hitachi S-4800 microscope at an accelerating voltage of 20 kV.

Atomic force microscopy (AFM)
AFM was carried out with a Bruker Dimension Icon microscope in scan-assist-mode. A Bruker Scanasyst-Air silicon tip with a diameter of around 10 nm was used to obtain images with a resolution of 512×512 or 1024×1024 pixels. The Gwyddion software was used for flattening and image correction.

Transmission electron microscopy (TEM)
Transmission electron microscopy was carried out using a JEOL JEM-1010 at 100 kV accelerating voltage and a Tecnai F20 operated at 200 kV. Images were acquired in bright-field mode with an objective aperture selecting the unscattered electrons. To record the images, an AMT RX80 8MP CCD camera (JEOL JEM-1010) and a Gatan CCD 1k × 1k device were used.

Supporting Information

Supporting Information features additional structural, spectroscopic, and magnetic characterization data.

Supporting Information File 1
Additional experimental data.
[https://www.beilstein-journals.org/bjnano/content/supplementary/2190-4286-14-76-S1.pdf]

ORCID® iDs
Camilo Jaramillo-Hernández - https://orcid.org/0000-0001-8163-5056
Gonzalo Abellán - https://orcid.org/0000-0003-1564-6210

References
1. Geim, A. K.; Novoselov, K. S. *Nat. Mater.* **2007,** *6,* 183–191. doi:10.1038/nmat1849
2. Miró, P.; Audiffred, M.; Heine, T. *Chem. Soc. Rev.* **2014,** *43,* 6537–6554. doi:10.1039/c4cs00102h
3. Mannix, A. J.; Kiraly, B.; Hersam, M. C.; Guisinger, N. P. *Nat. Rev. Chem.* **2017,** *1,* 0014. doi:10.1038/s41570-016-0014
4. Carrasco, J. A.; Congost-Escoin, P.; Assebban, M.; Abellán, G. *Chem. Soc. Rev.* **2023,** *52,* 1288–1330. doi:10.1039/d2cs00570k
5. Pastore, H. O.; Marchese, L. *J. Mater. Chem.* **2009,** *19,* 2453–2456. doi:10.1039/b904902a
6. Duong, D. L.; Yun, S. J.; Lee, Y. H. *ACS Nano* **2017,** *11,* 11803–11830. doi:10.1021/acsnano.7b07436
7. Liu, Y.; Weiss, N. O.; Duan, X.; Cheng, H.-C.; Huang, Y.; Duan, X. *Nat. Rev. Mater.* **2016,** *1,* 16042. doi:10.1038/natrevmats.2016.42

8. Coleman, J. N.; Lotya, M.; O'Neill, A.; Bergin, S. D.; King, P. J.; Khan, U.; Young, K.; Gaucher, A.; De, S.; Smith, R. J.; Shvets, I. V.; Arora, S. K.; Stanton, G.; Kim, H.-Y.; Lee, K.; Kim, G. T.; Duesberg, G. S.; Hallam, T.; Boland, J. J.; Wang, J. J.; Donegan, J. F.; Grunlan, J. C.; Moriarty, G.; Shmeliov, A.; Nicholls, R. J.; Perkins, J. M.; Grieveson, E. M.; Theuwissen, K.; McComb, D. W.; Nellist, P. D.; Nicolosi, V. *Science* **2011,** *331,* 568–571. doi:10.1126/science.1194975

9. Centi, G.; Perathoner, S. *Microporous Mesoporous Mater.* **2008,** *107,* 3–15. doi:10.1016/j.micromeso.2007.03.011

10. Nicolosi, V.; Chhowalla, M.; Kanatzidis, M. G.; Strano, M. S.; Coleman, J. N. *Science* **2013,** *340,* 1226419. doi:10.1126/science.1226419

11. Kaul, A. B. *J. Mater. Res.* **2014,** *29,* 348–361. doi:10.1557/jmr.2014.6

12. Carrasco, J. A.; Seijas-Da Silva, A.; Oestreicher, V.; Romero, J.; Márkus, B. G.; Simon, F.; Vieira, B. J. C.; Waerenborgh, J. C.; Abellán, G.; Coronado, E. *Chem. – Eur. J.* **2020,** *26,* 6504–6517. doi:10.1002/chem.201905397

13. Liu, Z.; Ma, R.; Osada, M.; Iyi, N.; Ebina, Y.; Takada, K.; Sasaki, T. *J. Am. Chem. Soc.* **2006,** *128,* 4872–4880. doi:10.1021/ja0584471

14. Abellán, G.; Martí-Gastaldo, C.; Ribera, A.; Coronado, E. *Acc. Chem. Res.* **2015,** *48,* 1601–1611. doi:10.1021/acs.accounts.5b00033

15. SeijasDa Silva, A.; Sanchis-Gual, R.; Carrasco, J. A.; Oestreicher, V.; Abellán, G.; Coronado, E. *Batteries Supercaps* **2020,** *3,* 499–509. doi:10.1002/batt.201900223

16. Yu, J.; Wang, Q.; O'Hare, D.; Sun, L. *Chem. Soc. Rev.* **2017,** *46,* 5950–5974. doi:10.1039/c7cs00318h

17. Chaillot, D.; Bennici, S.; Brendlé, J. *Environ. Sci. Pollut. Res.* **2021,** *28,* 24375–24405. doi:10.1007/s11356-020-08498-6

18. Mohapatra, L.; Parida, K. *J. Mater. Chem. A* **2016,** *4,* 10744–10766. doi:10.1039/c6ta01668e

19. Sarfraz, M.; Shakir, I. *J. Energy Storage* **2017,** *13,* 103–122. doi:10.1016/j.est.2017.06.011

20. Fan, G.; Li, F.; Evans, D. G.; Duan, X. *Chem. Soc. Rev.* **2014,** *43,* 7040–7066. doi:10.1039/c4cs00160e

21. Abellán, G.; Carrasco, J. A.; Coronado, E. Layered Double Hydroxide Nanocomposites Based on Carbon Nanoforms. In *Layered Double Hydroxide Polymer Nanocomposites;* Thomas, S.; Daniel, S., Eds.; Elsevier, 2020; pp 411–460. doi:10.1016/b978-0-08-101903-0.00010-6

22. Song, X.; Yuan, F.; Schoop, L. M. *Appl. Phys. Rev.* **2021,** *8,* 011312. doi:10.1063/5.0038644

23. Seijas-Da Silva, A.; Carrasco, J. A.; Vieira, B. J. C.; Waerenborgh, J. C.; Coronado, E.; Abellán, G. *Dalton Trans.* **2023,** *52,* 1219–1228. doi:10.1039/d2dt03804h

24. Mishra, G.; Dash, B.; Pandey, S. *Appl. Clay Sci.* **2018,** *153,* 172–186. doi:10.1016/j.clay.2017.12.021

25. Miyata, S. *Clays Clay Miner.* **1980,** *28,* 50–56. doi:10.1346/ccmn.1980.0280107

26. Richetta, M.; Medaglia, P. G.; Mattoccia, A.; Varone, A.; Pizzoferrato, R. *J. Mater. Sci. Eng.* **2017,** *6,* 1000360. doi:10.4172/2169-0022.1000360

27. Qu, J.; Zhang, Q.; Li, X.; He, X.; Song, S. *Appl. Clay Sci.* **2016,** *119,* 185–192. doi:10.1016/j.clay.2015.10.018

28. Oestreicher, V.; Jobbágy, M. *Langmuir* **2013,** *29,* 12104–12109. doi:10.1021/la402260m

29. He, J.; Wei, M.; Li, B.; Kang, Y.; Evans, D. G.; Duan, X. Preparation of Layered Double Hydroxides. In *Layered Double Hydroxides;* Duan, X.; Evans, D. G., Eds.; Structure and Bonding, Vol. 119; Springer-Verlag: Berlin/Heidelberg, 2005; pp 89–119. doi:10.1007/430_006

30. Liu, Z.; Ma, R.; Osada, M.; Takada, K.; Sasaki, T. *J. Am. Chem. Soc.* **2005,** *127,* 13869–13874. doi:10.1021/ja0523338

31. Ma, R.; Liu, Z.; Takada, K.; Fukuda, K.; Ebina, Y.; Bando, Y.; Sasaki, T. *Inorg. Chem.* **2006,** *45,* 3964–3969. doi:10.1021/ic052108r

32. Abellán, G.; Coronado, E.; Martí-Gastaldo, C.; Ribera, A.; Jordá, J. L.; García, H. *Adv. Mater. (Weinheim, Ger.)* **2014,** *26,* 4156–4162. doi:10.1002/adma.201400713

33. Okamoto, K.; Iyi, N.; Sasaki, T. *Appl. Clay Sci.* **2007,** *37,* 23–31. doi:10.1016/j.clay.2006.10.008

34. Iyi, N.; Matsumoto, T.; Kaneko, Y.; Kitamura, K. *Chem. Lett.* **2004,** *33,* 1122–1123. doi:10.1246/cl.2004.1122

35. Arai, Y.; Ogawa, M. *Appl. Clay Sci.* **2009,** *42,* 601–604. doi:10.1016/j.clay.2008.04.011

36. Xu, Z. P.; Lu, G. Q. (Max). *Chem. Mater.* **2005,** *17,* 1055–1062. doi:10.1021/cm048085g

37. Ogawa, M.; Kaiho, H. *Langmuir* **2002,** *18,* 4240–4242. doi:10.1021/la0117045

38. Reichle, W. T. *Solid State Ionics* **1986,** *22,* 135–141. doi:10.1016/0167-2738(86)90067-6

39. Sato, T.; Fujita, H.; Endo, T.; Shimada, M.; Tsunashima, A. *React. Solids* **1988,** *5,* 219–228. doi:10.1016/0168-7336(88)80089-5

40. Kong, X.; Ge, R.; Liu, T.; Xu, S.; Hao, P.; Zhao, X.; Li, Z.; Lei, X.; Duan, H. *Chem. Eng. J.* **2021,** *407,* 127178. doi:10.1016/j.cej.2020.127178

41. Mao, F.; Hao, P.; Zhu, Y.; Kong, X.; Duan, X. *Chin. J. Chem. Eng.* **2022,** *41,* 42–48. doi:10.1016/j.cjche.2021.09.023

42. Chen, Z.; Fan, Q.; Huang, M.; Cölfen, H. *CrystEngComm* **2022,** *24,* 4639–4655. doi:10.1039/d2ce00511e

43. Wang, Q.; Tang, S. V. Y.; Lester, E.; O'Hare, D. *Nanoscale* **2013,** *5,* 114–117. doi:10.1039/c2nr32568c

44. Tichit, D.; Layrac, G.; Gérardin, C. *Chem. Eng. J.* **2019,** *369,* 302–332. doi:10.1016/j.cej.2019.03.057

45. Oestreicher, V.; Jobbágy, M. *Chem. – Eur. J.* **2019,** *25,* 12611–12619. doi:10.1002/chem.201902627

46. Carrasco, J. A.; Abellán, G.; Coronado, E. *J. Mater. Chem. C* **2018,** *6,* 1187–1198. doi:10.1039/c7tc05569b

47. Guoxiang, P.; Xinhui, X.; Jingshan, L.; Feng, C.; Zhihong, Y.; Hongjin, F. *Appl. Clay Sci.* **2014,** *102,* 28–32. doi:10.1016/j.clay.2014.10.003

48. Sanchis-Gual, R.; Hunt, D.; Jaramillo, C.; Seijas-Da Silva, Á.; Mizrahi, M.; Marini, C.; Oestreicher, V.; Abellán, G. *ChemRxiv* **2022,** 1–22. doi:10.26434/chemrxiv-2022-rcq28

49. Biesinger, M. C.; Payne, B. P.; Grosvenor, A. P.; Lau, L. W. M.; Gerson, A. R.; Smart, R. S. C. *Appl. Surf. Sci.* **2011,** *257,* 2717–2730. doi:10.1016/j.apsusc.2010.10.051

50. Hunt, D.; Oestreicher, V.; Mizrahi, M.; Requejo, F. G.; Jobbágy, M. *Chem. – Eur. J.* **2020,** *26,* 17081–17090. doi:10.1002/chem.202001944

51. Neilson, J. R.; Schwenzer, B.; Seshadri, R.; Morse, D. E. *Inorg. Chem.* **2009,** *48,* 11017–11023. doi:10.1021/ic901167u

52. Oestreicher, V.; Hunt, D.; Torres-Cavanillas, R.; Abellán, G.; Scherlis, D. A.; Jobbágy, M. *Inorg. Chem.* **2019,** *58,* 9414–9424. doi:10.1021/acs.inorgchem.9b01252

53. Oestreicher, V.; Hunt, D.; Dolle, C.; Borovik, P.; Jobbágy, M.; Abellán, G.; Coronado, E. *Chem. – Eur. J.* **2021,** *27,* 921–927. doi:10.1002/chem.202003593

54. Oestreicher, V.; Abellán, G.; Coronado, E. *Phys. Status Solidi RRL* **2020,** *14,* 2000380. doi:10.1002/pssr.202000380

55. Oestreicher, V.; Dolle, C.; Hunt, D.; Fickert, M.; Abellán, G. *Nano Mater. Sci.* **2022,** *4,* 36–43. doi:10.1016/j.nanoms.2020.12.004

56. Du, Y.; Ok, K. M.; O'Hare, D. *J. Mater. Chem.* **2008,** *18,* 4450. doi:10.1039/b809085h

57. de A. A. Soler-Illia, G. J.; Candal, R. J.; Regazzoni, A. E.; Blesa, M. A. *Chem. Mater.* **1997,** *9,* 184–191. doi:10.1021/cm9602813

58. de A. A. Soler-Illia, G. J.; Jobbágy, M.; Regazzoni, A. E.; Blesa, M. A. *Chem. Mater.* **1999,** *11,* 3140–3146. doi:10.1021/cm9902220

59. Intasa-Ard, S. (Grace); Ogawa, M. *J. Solid State Chem.* **2023,** *317,* 123664. doi:10.1016/j.jssc.2022.123664

60. Raimundo, B.; Kino, D.; Kitgawa, N.; Tokudome, Y.; Nunes, C. D. *Appl. Clay Sci.* **2023,** *239,* 106948. doi:10.1016/j.clay.2023.106948

61. Oestreicher, V.; Fábregas, I.; Jobbágy, M. *J. Phys. Chem. C* **2014,** *118,* 30274–30281. doi:10.1021/jp510341q

62. Masoud, E. M.; El-Bellihi, A.-A.; Bayoumy, W. A.; Abdelazeem, E. S. *Ionics* **2017,** *23,* 2417–2427. doi:10.1007/s11581-017-2091-0

63. Oestreicher, V.; Jobbágy, M. *Chem. Commun.* **2017,** *53,* 3466–3468. doi:10.1039/c7cc00737j

64. Huo, J.; Brightwell, M.; El Hankari, S.; Garai, A.; Bradshaw, D. *J. Mater. Chem. A* **2013,** *1,* 15220. doi:10.1039/c3ta14409g

65. Garzón-Tovar, L.; Carné-Sánchez, A.; Carbonell, C.; Imaz, I.; Maspoch, D. *J. Mater. Chem. A* **2015,** *3,* 20819–20826. doi:10.1039/c5ta04923g

66. Intasa-Ard, S. (Grace); Bureekaew, S.; Ogawa, M. *J. Ceram. Soc. Jpn.* **2019,** *127,* 11–17. doi:10.2109/jcersj2.18140

67. Intasa-ard, S.; Ogawa, M. *Appl. Clay Sci.* **2022,** *228,* 106615. doi:10.1016/j.clay.2022.106615

68. Kino, D.; Tokudome, Y.; Vaz, P. D.; Nunes, C. D.; Takahashi, M. *J. Asian Ceram. Soc.* **2017,** *5,* 466–471. doi:10.1016/j.jascer.2017.10.003

69. Iqbal, M. A.; Fedel, M. *Coatings* **2019,** *9,* 30. doi:10.3390/coatings9010030

70. Boclair, J. W.; Braterman, P. S. *Chem. Mater.* **1999,** *11,* 298–302. doi:10.1021/cm980523u

71. Tian, Z.; Li, Q.; Hou, J.; Pei, L.; Li, Y.; Ai, S. *J. Catal.* **2015,** *331,* 193–202. doi:10.1016/j.jcat.2015.08.020

72. Abellán, G.; Coronado, E.; Martí-Gastaldo, C.; Ribera, A.; Otero, T. F. *Part. Part. Syst. Charact.* **2013,** *30,* 853–863. doi:10.1002/ppsc.201300186

73. Yang, K.; Yan, L.-g.; Yang, Y.-m.; Yu, S.-j.; Shan, R.-r.; Yu, H.-q.; Zhu, B.-c.; Du, B. *Sep. Purif. Technol.* **2014,** *124,* 36–42. doi:10.1016/j.seppur.2013.12.042

74. Triantafyllidis, K. S.; Peleka, E. N.; Komvokis, V. G.; Mavros, P. P. *J. Colloid Interface Sci.* **2010,** *342,* 427–436. doi:10.1016/j.jcis.2009.10.063

75. Yun, S. K.; Pinnavaia, T. J. *Chem. Mater.* **1995,** *7,* 348–354. doi:10.1021/cm00050a017

76. Sing, K. S. W. *Pure Appl. Chem.* **1985,** *57,* 603–619. doi:10.1351/pac198557040603

77. Ravel, B.; Newville, M. *J. Synchrotron Radiat.* **2005,** *12,* 537–541. doi:10.1107/s0909049505012719

78. Rehr, J. J.; Kas, J. J.; Vila, F. D.; Prange, M. P.; Jorissen, K. *Phys. Chem. Chem. Phys.* **2010,** *12,* 5503. doi:10.1039/b926434e